Title
On healable polymers and fiber-reinforced composites

Permalink
https://escholarship.org/uc/item/530191hr

Author
Nielsen, Christian Eric

Publication Date
2012

Peer reviewed|Thesis/dissertation

UNIVERSITY OF CALIFORNIA, SAN DIEGO

On Healable Polymers and Fiber-Reinforced Composites

A Dissertation submitted in partial satisfaction of the requirements for the degree
Doctor of Philosophy

in

Engineering Sciences (Applied Mechanics)

by

Christian Eric Nielsen

Committee in charge:

> Sia Nemat-Nasser, Chair
> Prabhakar Bandaru
> Vlado Lubarda
> Yitzhak Tor
> Haim Weizman

2012

The Dissertation of Christian Eric Nielsen is approved, and it is acceptable in quality and

form for publication on microfilm and electronically:

_____

_____

_____

_____

_____
Chair

University of California, San Diego

2012

DEDICATION

To my family and friends.

TABLE OF CONTENTS

LIST OF FIGURES

LIST OF TABLES

ACKNOWLEDGEMENTS

VITA

2006   Bachelor of Science in Mechanical Engineering, Case Western Reserve
            University, Cleveland, Ohio

2008   Master of Science in Engineering Sciences (Applied Mechanics),
            University of California, San Diego

2012   Doctor of Philosophy in Engineering Sciences (Applied Mechanics),
            University of California, San Diego

PUBLICATIONS

ARCHIVAL JOURNALS

Nielsen C, Amirkhizi AV, Nemat-Nasser S. The effect of geometry on fracture strength
        measurements using DCDC samples. Eng Fract Mech 2012;91:1-13.

Weizman H, Nielsen C, Weizman OS, Nemat-Nasser S. Synthesis of a self-healing
        polymer based on reversible Diels-Alder reaction: an advanced undergraduate
        laboratory at the interface of organic chemistry and materials science. J Chem
        Educ 2011;88;1137-40.

PROCEEDINGS

Nielsen C, Amirkhizi AV, Nemat-Nasser S. The influence of sample thickness on the
        DCDC fracture test. Proceedings of the 2011 SEM Annual Conference and
        Exposition on Experimental and Applied Mechanics, Uncasville, CT, June 13-16,
        2011.

Duenas T, VanderVennet JA, Jha A, Chai K, Nielsen C, Ayorinde AJ, Mal A. Using
        remendable polymers for aerospace composite structures. Proceedings of the 2011
        SEM Annual Conference and Exposition on Experimental and Applied
        Mechanics, Uncasville, CT, June 13-16, 2011.

Nielsen C, Weizman H, Nemat-Nasser S. Thermal and mechanical characterization of a
        healable polymer. Proceedings of 2010 SEM Annual Conference and Exposition
        on Experimental and Applied Mechanics, Indianapolis, IN, June 7-10, 2010.

Nielsen C, Weizman O, Nemat-Nasser S. Characterization of healable polymers.
        Proceedings of Behavior and Mechanics of Multifunctional Materials and
        Composites 2010, Vol. 7644, SPIE's 17th Annual International Conference on
        Smart Structures and Materials, San Diego, CA, March 7-11, 2010.

Nielsen C, Weizman H, Nemat-Nasser S. Healable polymers: characterization. Proceedings of Second International Conference on Self-Healing Materials 2009, Chicago, IL, June 28-July 1, 2009.

Nielsen C, Amirkhizi AV, Nemat-Nasser S. Geometric effects in DCDC fracture experiments. Proceedings of the 2009 SEM Annual Conference and Exposition on Experimental and Applied Mechanics, Albuquerque, NM, June 1-4, 2009.

ABSTRACT OF THE DISSERTATION

On Healable Polymers and Fiber-Reinforced Composites

by

Christian Eric Nielsen

Doctor of Philosophy in Engineering Sciences (Applied Mechanics)

University of California, San Diego, 2012

Professor Sia Nemat-Nasser, Chair

Polymeric materials capable of healing damage would be valuable in structural applications where access for repair is limited. Approaches to creating such materials are reviewed, with the present work focusing on polymers with thermally reversible covalent cross-links. These special cross-links are Diels-Alder (DA) adducts, which can be separated and re-formed, enabling healing of mechanical damage at the molecular level. Several DA-based polymers, including 2MEP4FS, are mechanically and thermally characterized. The polymerization reaction of 2MEP4FS is modeled and the number of

established DA adducts is associated with the glass transition temperature of the polymer. The models are applied to concentric cylinder rotational measurements of 2MEP4FS prepolymer at room and elevated temperatures to describe the viscosity as a function of time, temperature, and conversion. Mechanical damage including cracks and scratches are imparted in cured polymer samples and subsequently healed. Damage due to high temperature thermal degradation is observed to not be reversible.

The ability to repair damage without flowing polymer chains makes DA-based healable polymers particularly well-suited for crack healing. The double cleavage drilled compression (DCDC) fracture test is investigated as a useful method of creating and incrementally growing cracks in a sample. The effect of sample geometry on the fracture behavior is experimentally and computationally studied. Computational and empirical models are developed to estimate critical stress intensity factors from DCDC results.

Glass and carbon fiber-reinforced composites are fabricated with 2MEP4FS as the matrix material. A prepreg process is developed that uses temperature to control the polymerization rate of the monomers and produce homogeneous prepolymer for integration with a layer of unidirectional fiber. Multiple prepreg layers are laminated to form multi-layered cross-ply healable composites, which are characterized in bending using dynamic mechanical analysis (DMA). Simple, theory-based analyses indicate that numerous cracks are present before testing due to thermal expansion mismatches, and during testing, these cracks must be healing. Extending healable composites to include healable fiber-matrix interfaces is discussed as future work and interfacial healing characterization approaches are considered.

Chapter 1

Introduction

Healable materials have a built-in mechanism for repairing damage and restoring structural integrity. This capability can mitigate the need for manual repair or replacement, a time-consuming and expensive undertaking for traditional materials. In some applications, manual repair and replacement are especially difficult or even impossible, such as implants in the human body or structures sent into deep space.

The ability to heal damage would be particularly valuable for composite materials. Composed of two or more constituents, composites are heterogeneous at the micro- to macro-scale. In the case of a fiber-reinforced composite, strengthening fibers are embedded in a continuous matrix phase that facilitates load sharing. Mismatches between the constituents' mechanical and thermal properties often lead to the development of microcracks. Under fatigue conditions, this damage will accumulate, spread, and eventually lead to failure of the structure. A composite capable of repairing microcracks could have significant benefits: reduced weight associated with overdesign, extended service life, improved safety, and reduced life-cycle costs.

Inspiration for composites with a native healing capability can be found in biological systems. Bone has evolved to provide vertebrates with a strong yet lightweight and healable structural scaffolding: the skeletal system. Composed of extracellular collagen fibers and hydroxyapatite matrix, bone tissue is a natural composite. After a fracture, new tissue is formed by osteoblast cells as part of a more complex healing process of the complete bone structure (Figure 1.1).
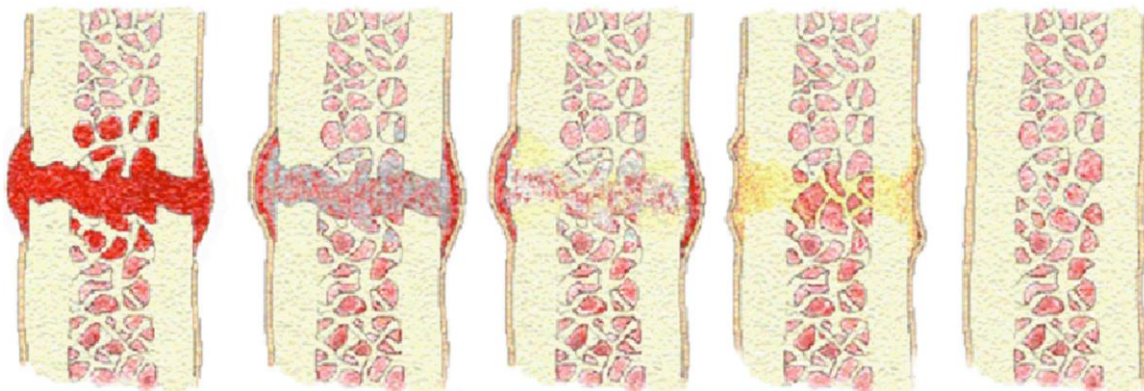
Figure 1.1   The healing process in a broken bone. (Brown et al. 2002)

1.1   Organization of Chapters

In the present work, polymers and composites are experimentally investigated and analyzed. Chapter 2 provides background on the various approaches to crack healing in polymers and composites. Chapter 3 covers the synthesis and mechanical and thermal testing of polymers with thermally reversible cross-links, focusing primarily on 2MEP4FS. Models for the conversion and conversion rate of 2MEP4FS are developed in Chapter 4, and they are applied to viscosity measurements of the prepolymer. Chapters 5 and 6 detour from healable polymers to investigate a mechanical test that is valuable for characterizing the fracture properties of brittle polymers.   In Chapter 5, a readily available polymer is used to study the fracture geometry, and a computational model is developed to estimate fracture toughness from the experimental results. In Chapter 6, the computational model is modified to further study the effect of sample geometry, as well as material properties and boundary conditions, on the fracture results, and an empirical model for estimating fracture toughness is developed. Chapter 7 examines the healing of mechanical and thermal damage imparted in neat 2MEP4FS samples.   Chapter 8

discusses and evaluates several approaches to fabricating fiber-reinforced composites with a healable polymer matrix. In Chapter 9, multi-layered composite samples are characterized, and simple analytical methods are used to show crack healing is occurring. Chapter 10 discusses healable interfaces, an area for future work.

Chapter 2

Healing Cracks in Polymers

There are several approaches to healing cracks in polymers intended for use in structural applications. These methods can be separated into two categories, autonomous and non-autonomous, depending on how the healing process is initiated and controlled. The term "healing" implies an internal repairing process and is distinguished from an external repairing process where additional material or a patch is applied from an external source. External repairing methods are not considered here.

2.1   Polymer Background

Polymers are macromolecules formed from repeating monomer units joined together by covalent bonds. The composition and arrangement of these monomers will determine the thermal and mechanical properties of the polymer. By adjusting the monomers or their assembled structure, polymers can be tailored for the desired application.

One method of classifying polymers is by their response to heat. Thermoplastic polymers will soften and melt, allowing remolding of the structure. These polymers are generally composed of long, linear or branched chains arranged in a semi-crystalline or amorphous structure. With no covalent cross-linking bonds between chains, the entanglements and relatively weak secondary forces (van der Waals, hydrogen, etc.) are overcome with the application of heat, allowing relative motion between chains.

Examples of common thermoplastic polymers include polyethylene, polypropylene, and poly(methyl methacrylate).

Thermosetting polymers, by contrast, do not melt when heat is applied. Covalent cross-linking bonds between chains create a large polymer network that will degrade irreversibly when excessively heated. Examples of common thermosetting polymers include epoxy and vulcanized rubber.

2.2   Autonomous Healing

Autonomous healing of polymers relies on processes that occur spontaneously, without external initiation or control. One approach is embedding catalysts and microcapsules of healing agent into a thermoset polymer (White et al. 2001). Propagating crack tips will puncture the capsules, releasing the agent into the crack, where it encounters catalyst particles and polymerizes (Figure 2.1). Initial work yielded an average healing efficiency of 60 % as measured by the peak fracture load. After some optimization, healing efficiencies in excess of 90 % were observed (Brown et al. 2002). In addition to healing, the microcapsules have been shown to increase the fracture toughness of epoxy an average of 127 % (Brown et al. 2004) and significantly improve
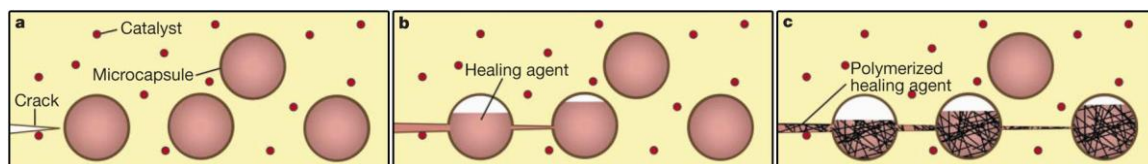
Figure 2.1   Microcapsule self-healing process: (a) crack forms; (b) crack tip breaks microcapsules, releasing healing agent; (c) agent polymerizes, repairing crack. (White et al, 2001)

fatigue resistance (Brown et al. 2006). Fibrous composites with an epoxy and microcapsule matrix material were found to have an average healing efficiency of 38 % (Kessler et al. 2003). Raising the healing temperature from ambient to 80 °C increased the healing efficiency average to 66 %.

Healing agents can also be incorporated into hollow fibers embedded in fiber-reinforced polymers. Breaking these special fibers releases the stored agent into damage sites. For two-part healing systems with a resin and hardener, it was found that some combination of solvent, heat, and vacuum must be used to reduce viscosity and draw out the components to effectively fill the damage sites (Bleay et al. 2001). A two-part healing agent with solvent was shown to restore 70 % of a host composite's flexural strength after damage (Pang and Bond 2005). A fibrous composite using a different two-part system sans solvent (Figure 2.2) was healed at an elevated temperature of 100 °C and showed 100 % recovery of flexural strength (Trask and Bond 2006). Compared with a reference, non-healable composite, the addition of hollow fibers reduced the composite's flexural strength by 16 %.
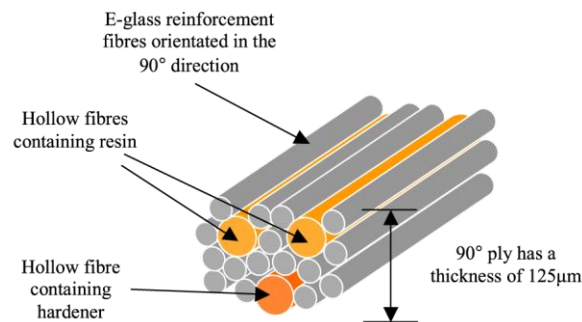
Figure 2.2 The two components of a healing agent are contained in separate hollow fibers integrated in a fibrous composite. (Trask and Bond 2006)

The autonomous healing methods discussed here have several common drawbacks. Primarily, they are single-use systems. Once the microcapsules or hollow fibers have been breached and their healing agent polymerized, future damage in the same location will not be healed until it grows into virgin material. These systems also rely on capillary action to spread the healing agent, meaning a solvent or heat are required to reduce viscosity and facilitate effective distribution. Unless removed, a solvent will inhibit polymerization and reduce healing efficiency. Heat will help the agent spread and drive the polymerization to completion (maximizing healing efficiency), but represents a non-autonomic factor in the system. In the case of a two-part healing agent, capillary action needs to transport and combine a stoichiometric ratio of the components for ideal healing. Manufacturing fibrous composites with integrated healing agents poses challenges. Microcapsules and catalyst particles that should be evenly distributed within a composite could be excluded from certain regions by the fibers during integration. The particles will tend to be concentrated in resin-rich regions where microcracks are less likely to form (noted by Plaisted 2007 regarding Kessler et al. 2003).

Despite the limitations, the microcapsule and hollow fiber approaches have been used to create truly self-healing materials and composites, a notable accomplishment.

2.3 Non-Autonomous Healing

Healing processes that must be activated or significantly accelerated by an external source are examples of non-autonomous healing. In thermoplastic materials, chain diffusion across an interface and bonding (Figure 2.3) will occur when the abutting surfaces are above the glass transition temperature (Wool and O'Conner 1981). Cracks
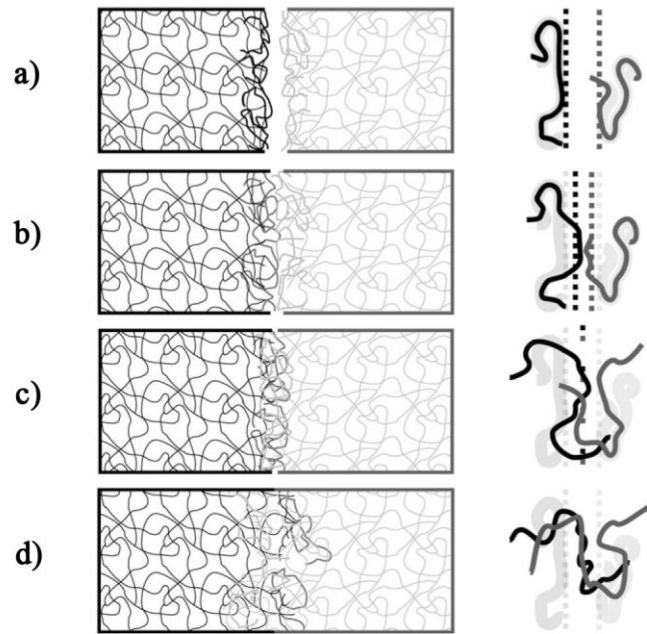
Figure 2.3   Diffusion healing of a crack in a thermoplastic.   (a) A crack breaks polymer chains; (b) the crack faces are brought in contact, and (c) the polymer chains diffuse across the interface leading to (d) entanglements and secondary bonding. (Wu et al. 2008)

in poly(methyl methacrylate) have been successfully healed using a thermal treatment (Jud et al. 1981).   Complete recovery of fracture toughness was possible with sufficient temperature and interface contact time.   Similar thermal treatments were used to heal cracks in fibrous composites with a thermoplastic matrix (Davies et al. 1989).   Solvents have also been used to reduce the effective glass transition temperature of thermoplastic crack interfaces, facilitating healing at lower temperatures (Lin et al. 1990; Wang et al. 1994).

A vascular network can be used to deliver healing agent to damage sites (Toohey et al. 2007).   The approach is an extension of the autonomous microcapsule and hollow fiber schemes.   Self-contained quantities of healing agent are replaced with a network of interconnected channels.   These systems are capable of healing the same location

multiple times. Two-part vascular healing systems (Figure 2.4) have demonstrated intermittent 60 % or higher healing efficiencies over 16 cycles (Toohey et al. 2009) and 50 % healing efficiencies after 30 healing cycles (Hansen et al. 2009). In these studies, cyclic flexural loading of the material was used to draw out and mix the healing agent. Another approach is to use an external reservoir of healing agent and a pressurized vascular network (Hamilton et al. 2010; Hamilton et al. 2012). A foam composite sandwich structure with this system was fully repaired when an active pump was used to increase the vascular pressure (Williams et al. 2008). Although the externality of the reservoir precludes labeling this repair as "healing" as defined in this review, the reservoir could eventually be integrated into the material and thereby warrants mention.

Embedded photopolymerizing agents can be used in place of two-part agents to create a healable material (Carlson et al. 2006). No mixing is required, but damaged areas must be exposed to a UV light source for healing to occur. This makes photopolymerizing agents useful for surface repairs in sunny locations.
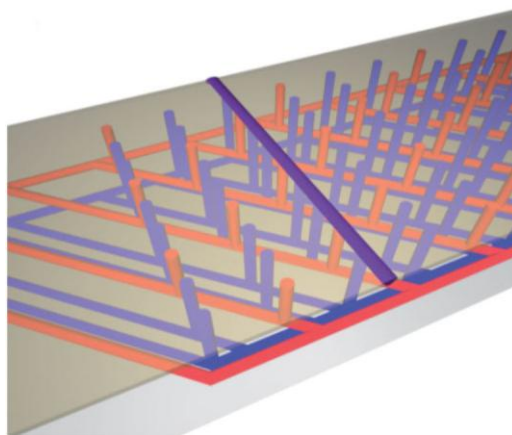
Figure 2.4 Illustration of vascular networks for a two-part epoxy healing agent. (Hansen et al. 2009)

All of the autonomous and non-autonomous approaches discussed thus far rely on physical transport for healing, be it the flow of a healing agent or diffusion of polymer chains. Re-establishing bonds at the molecular level is a unique alternative to polymer healing. Polymers with cross-linking bonds that can be formed, broken, and re-formed are termed "re-mendable". Hydrogen bonding between polymer chains has been shown to achieve this goal (Cordier et al. 2008; Chen et al. 2012), but relying on intramolecular forces leads to creep during prolonged loading. Re-mendable covalent bonds are possible via the Diels-Alder (DA) reaction, where a conjugated diene and reactive alkene (dienophile) are combined in a $(4+2)\pi$-electron cycloaddition to form a substituted cyclohexene. The DA adduct is thermally reversible, meaning that above a certain temperature, a retro-Diels-Alder (rDA) reaction will disconnect the diene and dienophile. A re-mendable, covalently cross-linked polymer was first demonstrated using a multi-furan monomer (the diene) and multi-maleimide monomer (the dienophile) (Figure 2.5) (Chen et al. 2002). Although the reaction will occur very slowly at ambient conditions, practical healing of this system requires the application of heat to drive the DA reaction by increasing interactions between functional groups. Initial crack healing studies indicated 80 % and 78 % healing efficiencies after the first and second crack healings
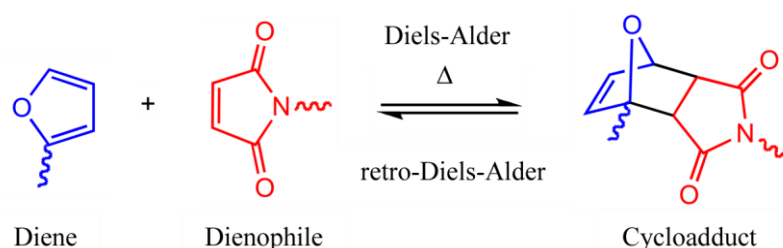
Figure 2.5 Schematic of the Diels-Alder and retro-Diels-Alder reactions in re-mendable polymers.

respectively (Chen et al. 2003). Subsequent experiments on a similar polymer using a different fracturing method yielded complete healing (Plaisted and Nemat-Nasser 2007). Aside from crack healing for structural purposes, re-mendable polymers have been proposed as rewritable data storage mediums (Gotsmann et al. 2006) and recyclable replacements for traditional thermosets (Watanabe and Yoshie 2006).

Non-autonomous healing systems have some disadvantages and inherent limitations. The materials are dependent on external factors for healing, factors that are not always readily provided by the environment. In the case of vascular networks (with or without an external reservoir), significant complexity has been designed into the structures, potentially making fabrication a challenge and reliability a concern. Photopolymerizing agents have limited applications, and subsurface damage in an opaque composite will not heal. Healing in DA-based polymers can be achieved while mechanical stiffness remains high, but this requires intimate contact between crack faces. Otherwise, the rDA reaction will be required to flow the polymer chains across the gap, during which time no significant mechanical loads can be supported.

In the course of reviewing literature, it is apparent that most of the work on DA-based polymers has focused on their chemistry and verifying thermal reversibility. Mechanical healing studies are less common, and applications in fibrous composites rarer still. These are areas of investigation in following chapters.

Chapter 3

Polymers with Thermally Reversible Cross-links

The first re-mendable polymers to be developed were 3M4F (Chen et al. 2002), 2ME4F, and 2MEP4F (Chen et al. 2003). Numerous other polymers and variations have since been developed and investigated. Here, a few of these polymers are examined in detail and thermally and mechanically characterized.

3.1   2MEP4FS

The majority of the work presented in this dissertation is focused on the re-mendable polymer 2MEP4FS. It's a highly cross-linked network of 4FS and 2MEP monomers connected via Diels-Alder reversible adducts (Figure 3.1). The polymer is a slightly modified version of 2MEP4F. One of the first re-mendable polymers, 2MEP4F is a combination of a tetrafuran monomer (4F) and a bismaleimide monomer (2MEP) (Chen et al. 2003). The synthesis route for 4F was later modified to simplify the process (Plaisted 2005), and resulted in an additional ester bonded to each functional group in the monomer (Figure 3.2). Since the original work was unpublished, the monomer was not
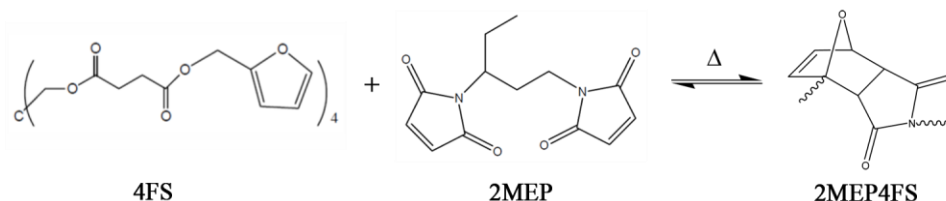
Figure 3.1   Diels-Alder reaction of 4FS and 2MEP to form 2MEP4FS. (Plaisted 2007)

4F   4FS
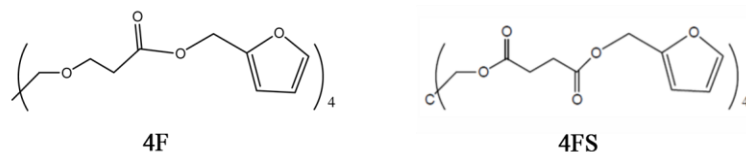
Figure 3.2   Schematics of tetrafuran monomer 4F (Chen 2003) and the modified tetrafuran monomer 4FS (Plaisted 2007).

specifically named, and Plaisted used it under the original 4F designation in his research. Other writings have termed the modified monomer "4FS" (Wudl 2004), the nomenclature used here.

3.1.1   Monomer Synthesis

In the present research, the synthesis procedure of the tertafuran diene has been changed again to improve yield and reduce the need for purification (Weizman et al. 2011). The final product, 4FS, has not changed. Where the previous method started with the pentaerythritol core of the monomer and built outward, the new procedure works in the opposite direction (Figure 3.3).   Furfuryl alchohol, anhydride, and 4-dimethylaminopyridine catalyst were combined at 50 °C to form a furfuryl acid. The acid was purified via column chromatography and reacted with pentaerythritol in dimethylformamide using N,N'-dicyclohexylcarbodiimide and 4-dimethylaminopyridine. White precipitates were filtered out and the compound was separated using column chromatography. The 4FS product is a yellow to yellow-orange clear viscous liquid at ambient conditions with a molecular weight of 856.7 g/mol.

The dienophile, monomer 2MEP, was also synthesized (Figure 3.4) (Chen et al. 2002). A diamine was combined with maleic anhyrdride in tetrahyrdofuran at 60 °C.
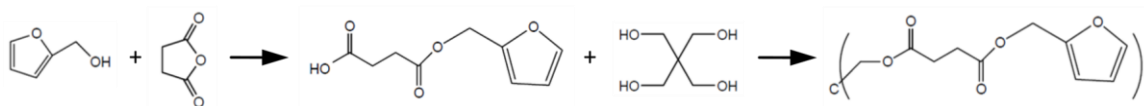
Figure 3.3 The 4FS synthesis route.
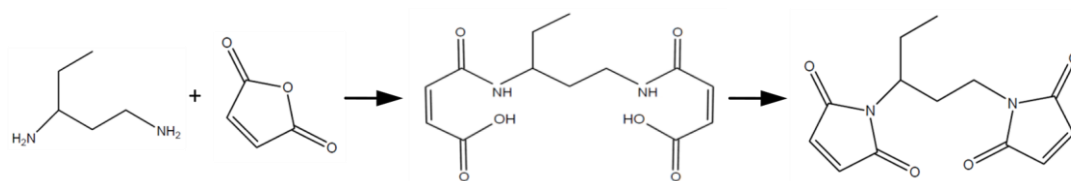
Figure 3.4 The 2MEP synthesis route.

The white precipitates were filtered out and combined with acetic anhydride and sodium acetate catalyst in dimethylformamide at 80-90 °C. After extraction and column chromatography, the compound was dried under high vacuum. The 2MEP product is a bright white powder at ambient conditions with a molecular weight of 262.1 g/mol.

3.1.2 Polymerization

Polymer 2MEP4FS samples were prepared by combining 2MEP and 4FS monomers in stoichiometric proportions. The monomers were separately heated to 90 °C to melt the 2MEP and reduce the viscosity of the 4FS before mixing under high vacuum. The hot prepolymer was poured into a preheated PDMS silicone mold and cured in a 90-95 °C oven for 5 hours. The sample was slowly cooled to room temperature over a period of 10 hours and removed from the mold. The final 2MEP4FS sample is transparent with a yellow-orange color similar to the 4FS monomer. The mass density of the sample, ρ, was measured to be 1.347 g/cm^3.

3.1.3 Differential Scanning Calorimetry

The monomers and resulting polymer were thermally characterized using differential scanning calorimetry (DSC). Standard DSC tests were conducted using a TA Instruments 2920 with 3 °C/min temperature ramp rate, hermetically sealed aluminum pans and nitrogen purge gas. Modulated DSC (MDSC) experiments included an additional ±1 °C/min temperature oscillation to separate the heat flow into heating rate dependent and heating rate independent parts (TA Instruments 1998).

The monomer 2MEP was observed to melt at 85.8 °C (Figure 3.5), as measured by the endothermic peak in the heat flow. This is comparable to previously reported values for 2MEP (Chen et al. 2003; Plaisted 2007). Monomer 4FS showed no distinct transitions over the range of study (Figure 3.5), also similar to the literature (Plaisted
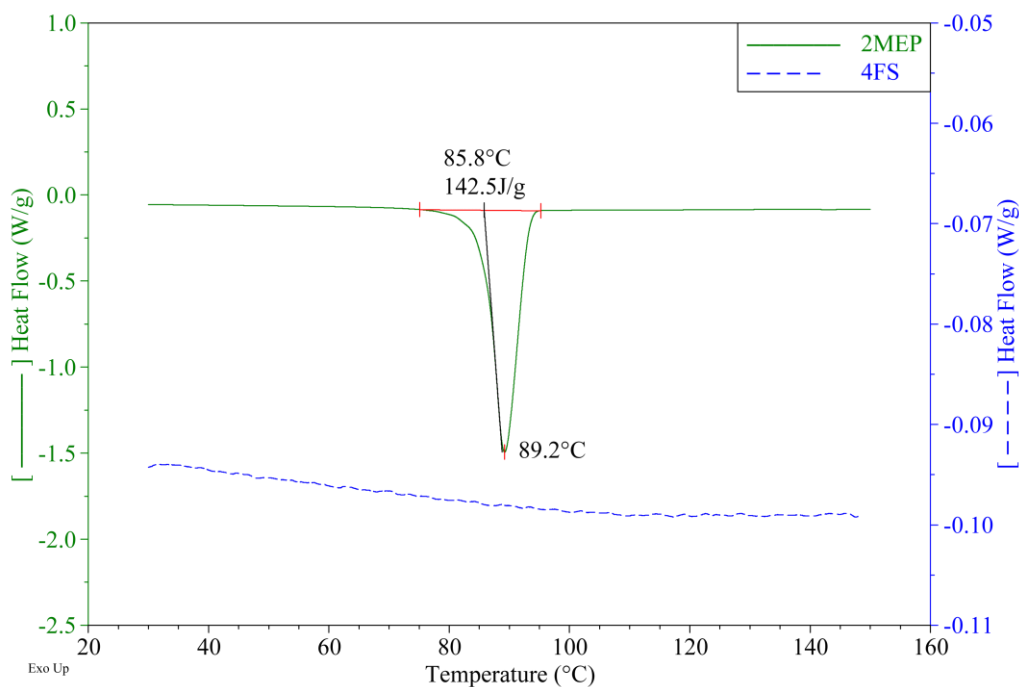
Figure 3.5 DSC results for 2MEP and 4FS monomers.

2007). A stoichiometric ratio of monomers was hand mixed and polymerized using DSC (Figure 3.6). A large exothermic peak centered at 82 °C corresponds to the Diels-Alder polymerization reaction. Assuming an ideal reaction, the 72.6 J/g peak equates to 6.0 kcal per mole of possible DA adducts in 2MEP4FS. For reference, the literature gives the DA adduct energy as 23 kcal/mol (Chen et al. 2002). Some of the missing exothermic energy may have been used to melt 2MEP, which was initially a solid powder. Observations of a vial of hand-mixed monomers heated in an oil bath indicate the 2MEP melts between 60 and 70 °C. Poor mixing of the monomers may also have diminished DA adduct production. Since the sample was dynamically scanned, not all of the possible DA adducts may have formed before the onset of the retro-Diels-Alder
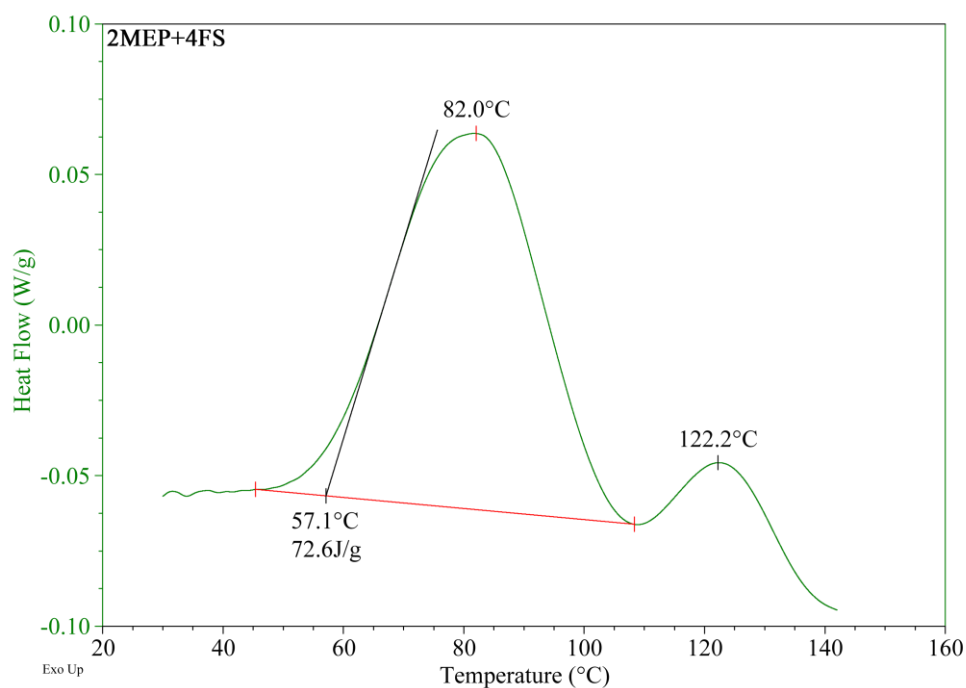
Figure 3.6 Manually-mixed 2MEP and 4FS monomers polymerizing during a DSC test.

(rDA) reaction. The cause of the second, smaller exothermic peak centered at 122 °C is unclear. The polymerization of 2MEP4FS is studied in more detail in Chapter 4.

Modulated DSC tests were conducted on a sample of oven-cured 2MEP4FS polymer (Figure 3.7). The glass transition temperature, T_g, of the sample is estimated to be 101.2 °C, as measured by the inflection point of the reversible, heating rate dependent part of the heat flow (TA Instruments 1998). A small exothermic peak in the non-reversing heat flow at 105.7 °C indicates the sample briefly gives off energy immediately after the glass transition temperature. This suggests that not all DA adducts had formed during the curing process. The endothermic peak beyond 110 °C has been previously attributed to the rDA reaction separating DA adducts (Chen et al. 2002).
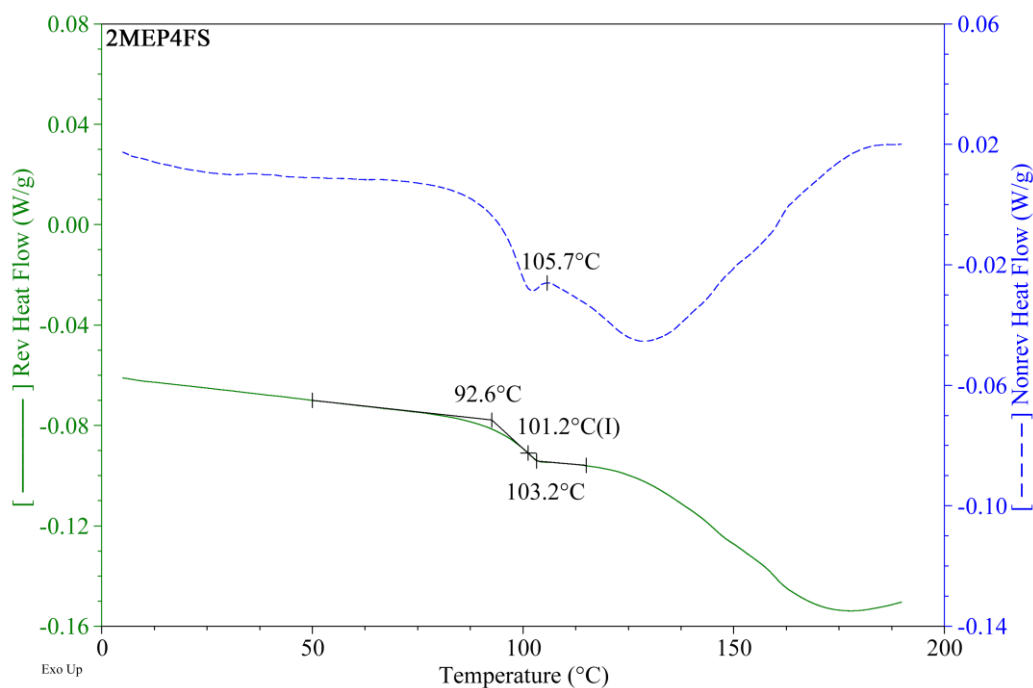
Figure 3.7   The heating rate dependent (reversible) and heating rate independent (non-reversible) heat flows for cured 2MEP4FS.

DSC was used to confirm the thermal reversibility of the DA adducts in the 2MEP4FS polymer (Figure 3.8). A second sample of the oven-cured polymer was tested multiple times to establish a stable baseline heat flow curve. Between each test, the hot sample was cooled to room temperature over a period of many minutes to an hour. This slow cooling gave separated DA adducts in the polymer time to re-establish. After the final baseline test, the hot sample was quenched in liquid nitrogen, preventing separated DA adducts from re-forming. Retesting the sample yielded a new exothermic peak in the heat flow around 79.5 °C. Here, the disconnected groups have sufficient mobility and energy to re-form the DA adduct. The peak is similar to the original polymerization peak, although smaller, suggesting not all of the DA adducts had been disconnected.
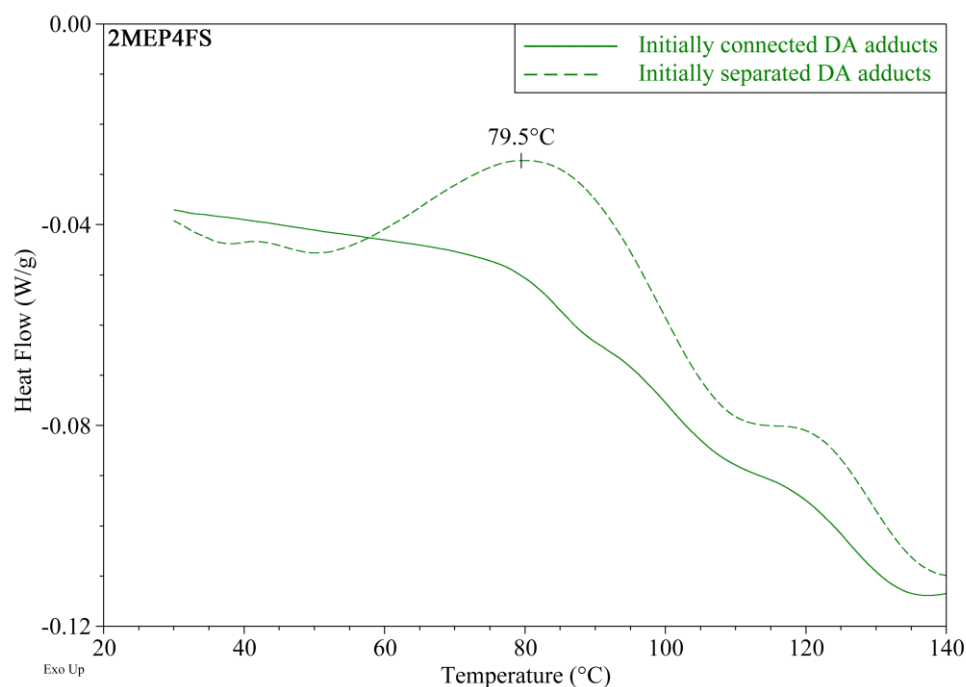
Figure 3.8 A cured 2MEP4FS sample is DSC tested until a repeatable heat flow profile is obtained (solid line), and then quenched in liquid nitrogen. The sample is retested to observe the re-formation of DA bonds (dashed line).

This manner of observing the presence of thermally reversible cross-links has been previously demonstrated in the literature (Chen 2003; Plaisted 2007).

3.1.4   Dynamic Mechanical Analysis

The viscoelastic properties of the cured 2MEP4FS sample were characterized as a function of frequency and temperature using dynamic mechanical analysis (DMA). The technique separates the elastic and viscous components of the mechanical response of a sample at a given frequency and temperature (TA Instruments 2002):

$$E^* = E' + iE''. \tag{3.1}$$

The complex modulus, E^*, is composed of the storage modulus, E', derived from the elastic, in-phase response, and the loss modulus, E'', derived from the viscous, out-of-phase response. The ratio of the loss to storage moduli is $\tan \delta$.

The cured 2MEP4FS sample was machined to create a parallelepiped with flat and parallel rectangular sides. It was mounted in a single cantilever fixture in a TA Instruments 2980 DMA (Figure 3.9). The clamp screws securing the ends of the sample
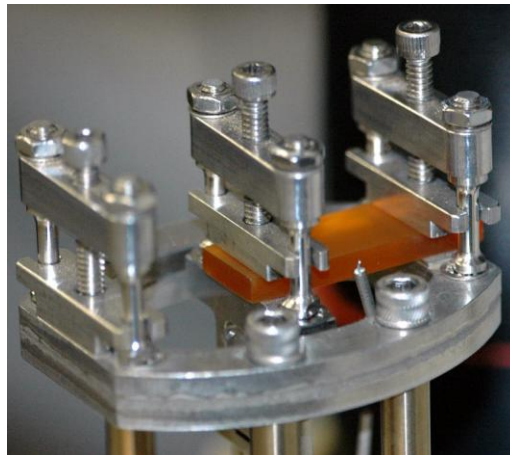
Figure 3.9   A cured 2MEP4FS sample mounted in the DMA cantilever fixture.

against rotation were tightened with 8 in·lbf of torque, and the instrument applied a 30 μm amplitude out-of-plane sinusoidal displacement to one end. A series of eight multi-frequency scans were conducted at room temperature at 0.1, 1, 2, 5, 10, and 20 Hz, with the sample removed and remounted between each scan (Figure 3.10). A temperature controlled test was also performed at a fixed frequency of 1 Hz (Figure 3.11). The sample temperature was ramped from 20 °C to 130 °C at 3 °C/min. At room temperature (22 °C), 2MEP4FS is almost perfectly elastic, with a storage modulus of 3.05 GPa and tan δ of 0.01. As the temperature increases, the storage modulus decreases gradually to 2.33 GPa at 85 °C, before decreasing rapidly to near zero beyond 115 °C. The tan δ of 2MEP4FS exhibits a peak of 1.2 at 110.9 °C, which can be taken as an estimate of T_g. A more conservative estimate of T_g for structural applications would be the inflection point of the decreasing storage modulus at 102.6 °C, or the onset of softening at 93.8 °C.

Taken together, the DSC and DMA results highlight the potential significance of the 2MEP4FS as a healable structural material. The establishment and re-establishment
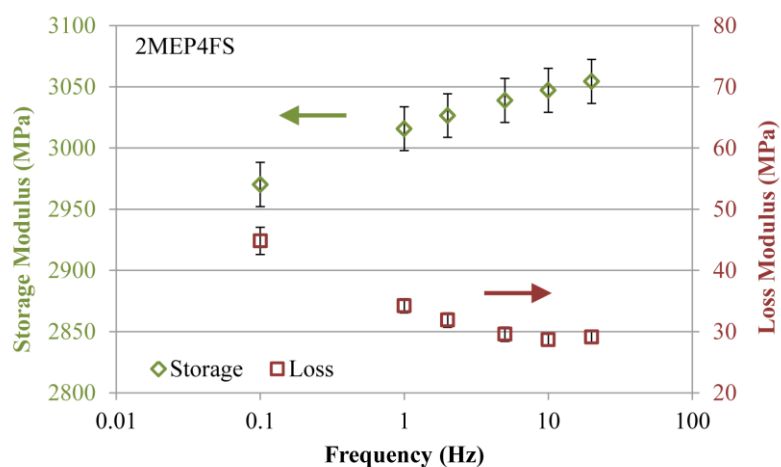
Figure 3.10 Room temperature DMA results for 2MEP4FS as a function of frequency.
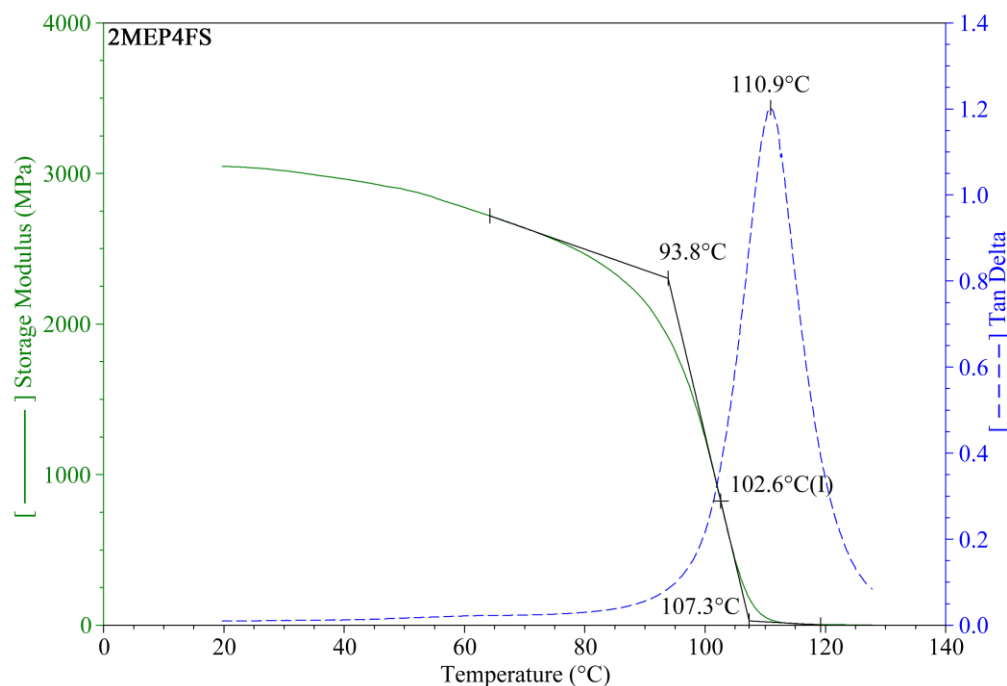
Figure 3.11 Single frequency (1 Hz) DMA results for 2MEP4FS as a function of temperature.

of DA bonds occurs at ~80 °C, a temperature where the material still has significant mechanical stiffness. This suggests the polymer can be healed using a thermal treatment while maintaining some load carrying capability. Under low loads, the polymer should be able to heal without creep occurring.

3.1.5 Ultrasonic Measurements

Prior to DMA testing at elevated temperatures, the cured 2MEP4FS sample was characterized with ultrasonic acoustic waves. The measurement system depicted in Figure 3.12 consists of a Matec TB-1000 tone burst signal generator, 100:1 attenuator, Tektronix DPO 3014 oscilloscope, and a pair of Olympus Panametrics V103-RB longitudinal or V153-RM shear contact transducers sending and receiving the ultrasonic
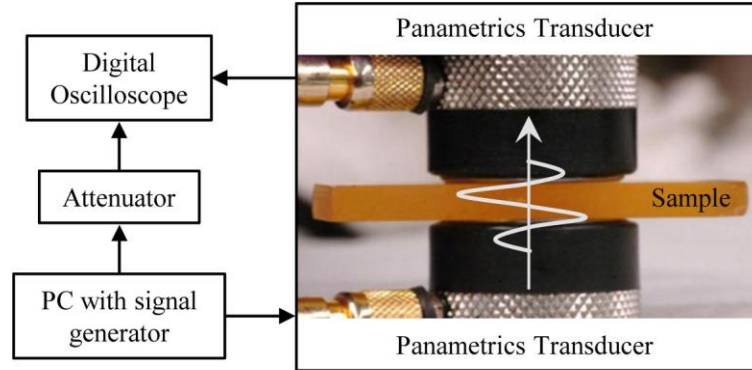
Figure 3.12   Diagram of the ultrasonic characterization system.

waves.   The transducers were lubricated with a couplant at the interfaces and measurements were made at room temperature using a 1 MHz signal. The wave speed is determined by dividing the sample thickness by the time required for the signal to pass through the sample. Attenuation was not considered in the present study.

Typically, the system is used to characterize two samples of the same material but different thicknesses (Qiao et al. 2011).   By subtracting the results, interfacial problems and time lags in the system are assumed to cancel out.   Since there was only one 2MEP4FS sample, measurements were made with and without the sample.   This approach was verified using a similarly sized piece of poly ethyl ethyl ketone (PEEK). Longitudinal and shear wave speeds were measured to be within 1 % of values given in the literature (Fitch et al. 2010).

The longitudinal wave speed and shear wave speed in 2MEP4FS were found to be 2460 m/s and 1130 m/s respectively.   Assuming the polymer is completely elastic at room temperature, which DMA measurements indicate is a reasonable approximation, the

mechanical properties of 2MEP4FS can be calculated (Table 3.1). The shear modulus, G, is related to the shear wave speed, c_S:

$$G = \rho c_S^2, \tag{3.2}$$

and the bulk modulus, K, is related to the longitudinal wave speed, c_L:

$$K = \rho c_L^2 - \frac{4}{3} G. \tag{3.3}$$

The Young's modulus, E, is:

$$E = \frac{9KG}{3K+G}, \tag{3.4}$$

and Poisson's ratio, ν, is:

$$\nu = \frac{3K-E}{6K}. \tag{3.5}$$

The Young's modulus estimated from ultrasonic measurements is ~50 % higher than the storage modulus measured by DMA. Although the measurements were made on the same sample at the same temperature, the two tests were performed at vastly different frequencies: 1 MHz versus 1 Hz. The discrepancy in the calculated results suggests that at high frequencies, an ideally elastic assumption may not be appropriate. Low temperature, multi-frequency DMA measurements of 2MEP4FS indicate an increasing $\tan \delta$ with decreasing temperature (Figure 3.13). According to time-temperature superposition (TTS) principles, lower temperatures correspond to shorter time-scales and higher frequencies. Since the polymer is below its glass transition temperature, the standard TTS equations and data shifting techniques meant for rubbery polymers (Qiao et al. 2011) cannot be applied to generate master curves.

Table 3.1   Ultrasonic wave speeds in 2MEP4FS and calculated properties.

c_L	c_S	G	K	E	ν
2461 m/s	1128 m/s	1.71 GPa	5.87 GPa	4.68 GPa	0.367
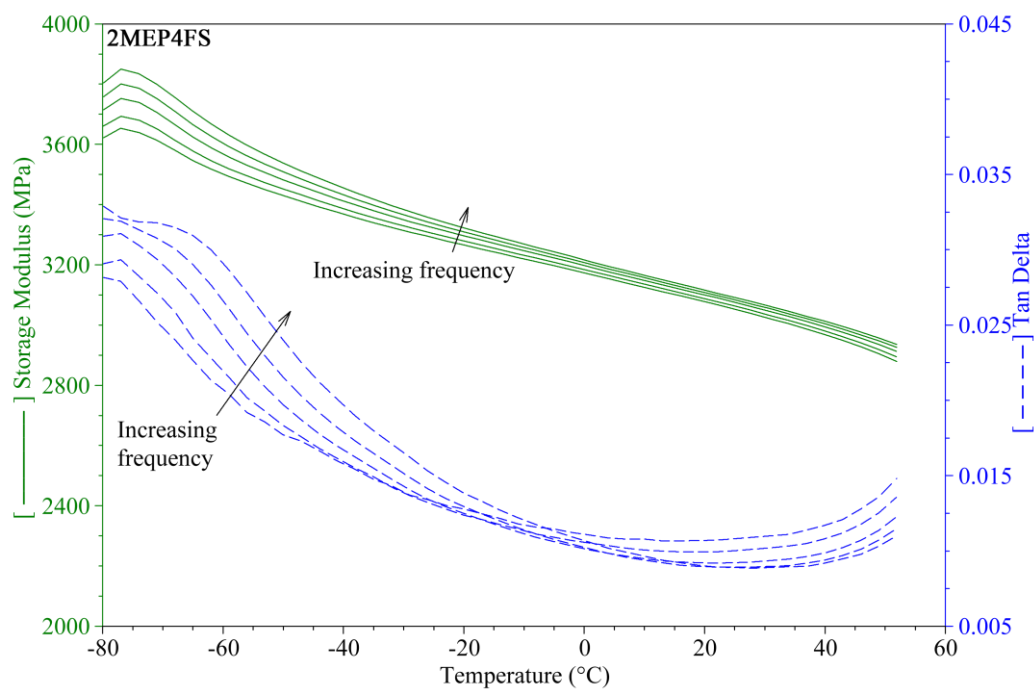
Figure 3.13   Low temperature DMA results for 2MEP4FS at 1, 2, 5, 10, and 20 Hz and stepped temperatures.

3.2   2MEP3FT

Modifications to the 2MEP4FS polymer have been explored. Using monomers that are more readily synthesized would save time and allow for larger geometries and more samples. Altering the constituent monomers could also allow polymer properties to be tailored. Glass transition temperature is one property of particular interest: raising T_g would increase the useful temperature range of the polymer.

A new furan monomer, 3FT, was synthesized to replace 4FS. 3FT has three furan groups bonded to a central 1,3,5 triazine ring (Figure 3.14). It is a yellow to yellow-orange clear viscous liquid at ambient conditions, with a molecular weight of 366.1 g/mol. The design is more easily synthesized than 4FS, and since the molecular linkages connecting the furan groups are significantly shorter, a 2MEP3FT polymer is predicted to have a higher stiffness than 2MEP4FS. DSC tests of hand-mixed 2MEP and 3FT monomers yielded a DA polymerization peak centered at 74.3 °C (Figure 3.15). The polymerization energy equates to 4.2 kcal per mole potential DA adduct. A small endothermic peak preceding the polymerization suggests the 2MEP is melting during the reaction, consuming energy. Modulated DSC testing of cured 2MEP3FT indicates a
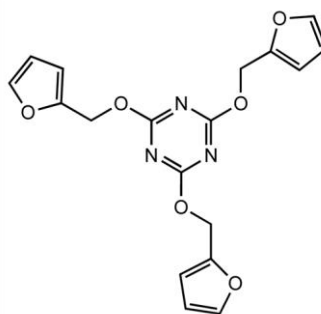
Figure 3.14   The 3FT monomer.

glass transition temperature in excess of 120 °C, significantly higher than 2MEP4FS. Additional DSC tests of the sample after rapid cooling did not exhibit an exothermic peak to indicate the presence of thermally reversible cross-links. Since the 3FT monomer was specially designed to create DA adducts with a maleimide like 2MEP, the relatively short furan linkages may lack the flexibility and mobility necessary to re-establish separated adducts.
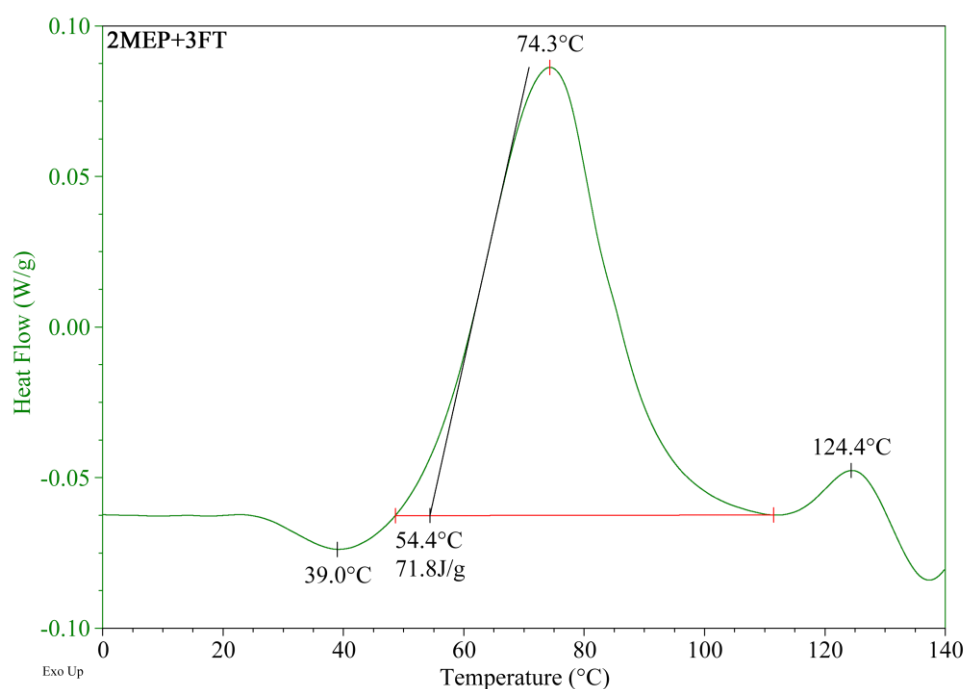
Figure 3.15 Manually mixed 2MEP and 3FT monomers polymerizing during a DSC test.

3.3   DPBM4FS

A commercially available replacement for the bismaleimide, 2MEP, was also considered: 1,1'-(methylenedi-4,1-phenylene)bismaleimide (DPBM, Sigma-Aldrich) (Figure 3.16). A DSC test of DPBM hand mixed with a stoichiometric proportion of 4FS shows a DA polymerization peak at 81.5 °C (Figure 3.17). Integrating the exothermic peak gives a polymerization energy of 1.4 kcal per mole of potential DA adducts, which is much lower than 2MEP4FS (6.0 kcal/mol) and 2MEP3FT (4.2 kcal/mol). The
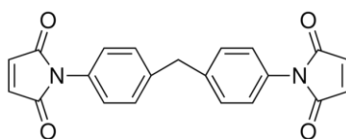
Figure 3.16 The DPBM monomer.
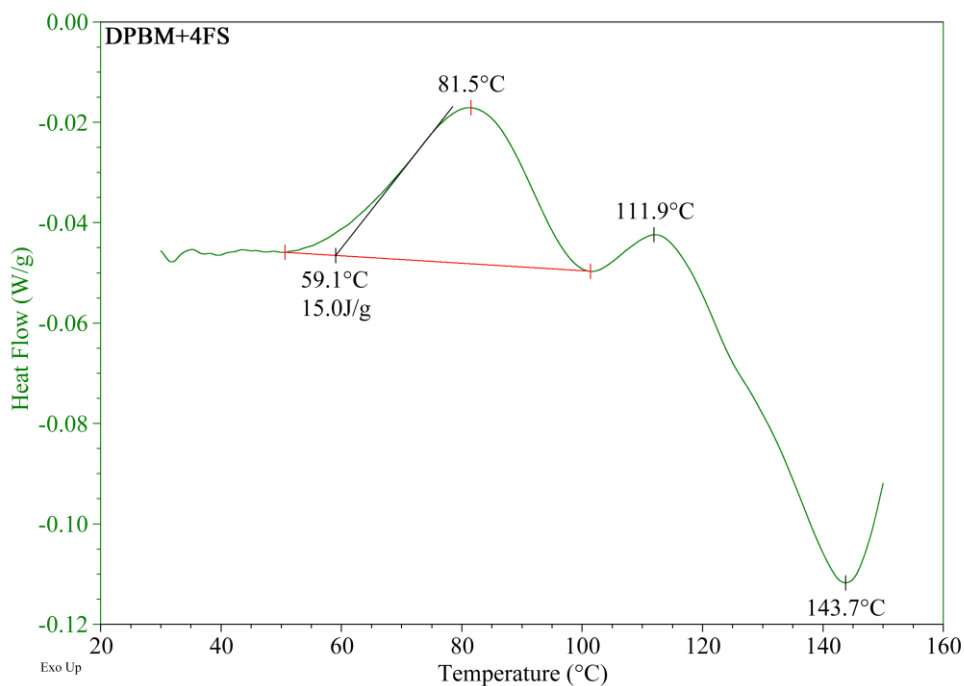
Figure 3.17 Manually-mixed DPBM and 4FS monomers polymerizing during a DSC test.

discrepancy may be related to poor mixing due to the relative coarseness of the DPBM powder compared with 2MEP. The large endothermic peak at 144 °C also suggests the DPBM is melting at a temperature much higher than the polymerization, which could have reduced DA adduct production. To improve polymerization, DPBM should be in a liquid phase when it's combined with 4FS. Neat DPBM was observed to melt at 157.6 °C, significantly higher than the polymerization temperature. Preliminary tests indicated poor sample properties when the monomers were combined at this temperature.

The thermal reversibility of DPBM4FS was established using DSC experiments with varied sample cooling rates. After rapidly cooling the sample, an exothermic peak associated with the re-establishing of DA adducts (Figure 3.18) was observed at 67.5 °C, lower than the ~82 °C observed during the initial polymerization.
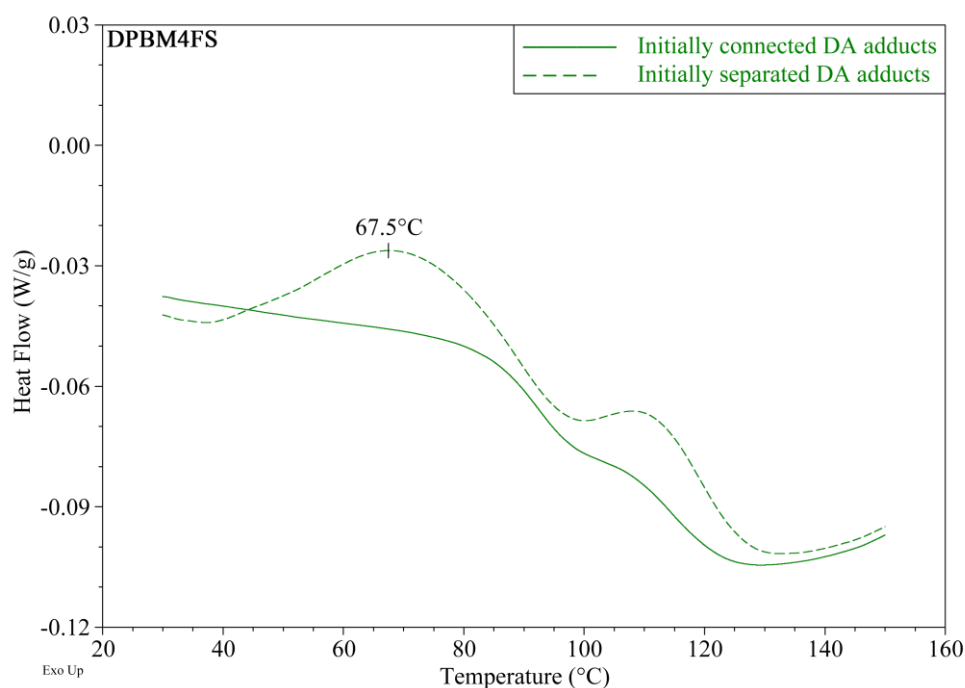
Figure 3.18 DPBM4FS is DSC tested (solid line), and quenched in liquid nitrogen. The sample is retested to observe the re-establishing of DA bonds (dashed line).

3.4 Polymer 400

Since there are inherent challenges to combining two monomers that are different phases at ambient conditions (see Chapter 8), a re-mendable polymer formed from a single component is desirable (Wudl 2004). Two such polymers have been developed: 400 and 401 (Murphy et al. 2008). Both polymers have a constituent monomer that contains a dicyclopentadiene core, which can undergo an rDA reaction to expose diene and dienophile functional groups. These groups can form DA bonds with neighboring monomers, creating the polymer (Figure 3.19). Additionally, the dicyclopentadiene can undergo a second DA reaction, forming a trimer and creating a cross-linked network.

Monomers 400 and 401 are structurally similar, but 401 has an additional ether in the tethering chain. These molecules were added to simplify processing, but led to a decrease in polymer T_g from 138 °C for polymer 400 to 89 °C for polymer 401 (Murphy et al. 2008). The elastic modulus and strength in compression were also reported: 1.51 GPa and 95.8 MPa for monomer 400, and 1.51 GPa and 95.8 MPa for monomer 401.
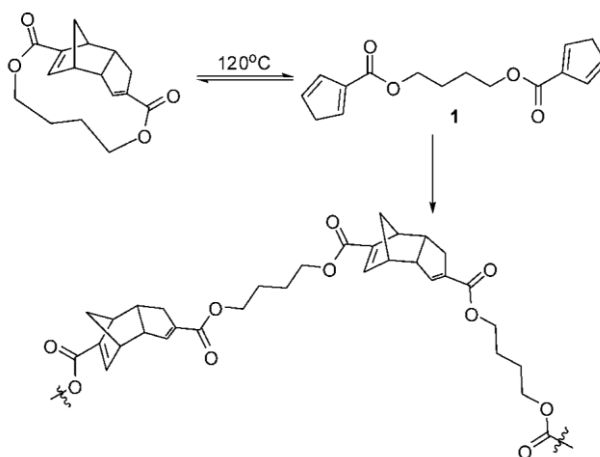
Figure 3.19 Monomer 400 (top left) undergoes rDA and DA reactions to form polymer 400. (Murphy et al. 2008)

A new batch of monomer 400 was obtained from Wudl's lab via NextGen Aeronautics (PI: Dr. Terrisa Duenas). The monomer is a white powder at ambient conditions. DSC testing indicates a melting temperature, T_m, of 120.7 °C, and a crystallization temperature, T_c, of 126.1 °C (Figure 3.20). Murphy et al. (2008) reported a T_m of 124.5 °C where the rDA reaction occurs and a T_c of 129.4 °C where polymerization occurs.

Beyond DSC testing, small quantities of monomer 400 were polymerized in vials. Careful control over the temperature ramp rate and a strong vacuum yielded uniform samples free of bubbles.

Figure 3.20 DSC results for monomer 400.

Chapter 4

Reaction Kinetics of 2MEP4FS with Application to Viscosity Measurements

Based on the thermal and mechanical results presented in Chapter 3, 2MEP4FS was selected for further evaluation and modeling of the polymerization reaction.

4.1   Introduction

Healable materials have built-in mechanisms for self-repair. When activated, these mechanisms mitigate damage, extending the useful life of the structure or coating. There are several approaches to designing such materials, including embedding healing-agent-filled capsules (White et al. 2001), hollow fibers (Pang and Bond 2005), or vascular networks (Toohey et al. 2007) into a host material, using reversible intermolecular interactions like hydrogen bonding (Cordier et al. 2008; Chen et al. 2012), or using reversible covalent bonding like the Diels-Alder adduct (Chen et al. 2002; Chen et al. 2003). A more detailed survey of the field is given by Murphy and Wudl (2010). In the Diels-Alder (DA) reaction, a diene and dienophile react in a cycloaddition to form a cyclohexene ring. This reaction is thermally reversible; the retro-Diels-Alder (rDA) reaction separates the cyclohexene ring into the original diene and dienophile groups. In a polymer system, using Diels-Alder adducts as cross-linking bonds means the cross-links can be formed, separated, and re-formed.

Cross-link formation in a traditional highly cross-linked polymer like epoxy generally proceeds in only one direction (increasing). In a DA-based polymer, however, the rDA reaction means the number of cross-links can decrease depending on the thermal and mechanical conditions. Since the thermal and mechanical properties of the polymer are dependent on the number of established cross-linking bonds (Nielsen 1969), knowledge of the number of cross-links present at any given time is important for predicting material behavior.

2MEP4FS is one example of a healable polymer with Diels-Alder cross-links. It is formed from the reaction of a tetrafuran diene, 4FS, and bismaleimide dienophile, 2MEP. Plaisted et al. (Plaisted 2007; Plaisted and Nemat-Nasser 2007) have extensively tested this polymer. They refer to the tetrafuran as '4F', where we use the name '4FS' to distinguish this monomer from the original 4F used by Chen et al. (2003), which has one less ester group due to the synthesis route. Notably, Plaisted and Nemat-Nasser (2007) successfully demonstrated complete fracture healing, even obtaining fracture stresses after multiple healings that exceeded the initial, virgin fracture stresses. Since the DA adduct is generally weaker than the surrounding covalent bonds, it is preferentially broken by a propagating crack tip (Chen et al. 2002). When the fracture surfaces are brought back together at a temperature below where the rDA reaction occurs, DA adducts are re-established, healing the damage.

One aspect of 2MEP4FS unaddressed by Plaisted is an estimate of the number of DA cross-links present in the fully cured polymer. Here, we seek to make this estimate using DSC thermal measurements and theoretical and empirical approximations. A processing method for producing homogenous small samples suitable for our experiments

is outlined. A model is developed that correlates the measured glass transition temperature (T_g) with the relative number of established Diels-Alder cross-links. A second model is developed for the rate of DA cross-link formation in 2MEP4FS as a function of temperature and the number of established cross-links. Special cases are considered to determine limits on the applicability of the rate model. Finally, the models are applied to mechanical measurements of 2MEP4FS during polymerization to describe the viscosity as a function of cross-linking. In future work, this approach could be used to describe other mechanical and thermal properties as a function of the number of established cross-links.

4.2   Synthesis

The bismaleimide 2MEP and tetrafuran 4FS monomers were synthesized according to established procedures (Chen et al. 2003; Weizman et al. 2011). At room temperature, 2MEP is a solid powder, while 4FS is a viscous liquid. Obtaining a well-mixed final polymer, 2MEP4FS, poses a challenge. Chen et al. (2003) used simple mixing to combine two dissimilar monomers before heating to cure the polymer. This approach is evaluated later and found to be insufficient for 2MEP4FS.

Large samples (on the order of grams) can be efficiently produced by separately heating the monomers to melt the 2MEP and reduce the viscosity of 4FS before mixing (Plaisted 2007; Plaisted and Nemat-Nasser 2007; Ghezzo et al. 2010). This procedure does not facilitate the preparation of the small samples (on the order of 10 mg) required for differential scanning calorimetry (DSC) thermal measurements. To minimize the initial polymerization before DSC testing, the hot mixture must be quenched, which is

challenging when working with relatively large monomer quantities. The unused prepolymer also amounts to wasted material, a significant drawback when monomer production is a time-consuming endeavor. Scaling down the monomer quantities addresses these issues, but quickly and precisely combining and effectively mixing small quantities of hot, low viscosity monomers proved difficult.

For the small samples used here in DSC and viscosity experiments, a polymerization procedure was developed to minimize wasted material, but still enable a precise mixture ratio of monomers. At room temperature, a stoichiometric proportion of 2MEP was added to 4FS in a disposable glass culture tube. The monomers were manually mixed and then placed under high vacuum. While still under vacuum, the culture tube was submerged in a preheated 90 °C silicone oil bath for 20-35 sec depending on the sample size. The light yellow opaque monomer mixture quickly became transparent as the 2MEP melted and bubbled vigorously as trapped gases were pulled out. Once the contents settled, the culture tube was quenched in liquid nitrogen to slow the polymerization process. After rewarming the culture tube to room temperature in a water bath, the vacuum was broken and the 2MEP4FS prepolymer was ready for testing. At this stage, the prepolymer was a transparent yellow in color and qualitatively similar in viscosity to the starting 4FS monomer. Quantitative viscosity measurements are discussed later.

4.3   Differential Scanning Calorimetry

Differential scanning calorimetry (DSC) measurements were performed using a TA Instruments DSC 2920. The instrument was configured with a liquid nitrogen

cooling accessory and 50 mL/min nitrogen purge gas. All samples were tested in sealed hermetic aluminum pans. Baseline and cell constant calibrations were performed for all heating rates. Temperature and heat capacity calibrations were performed for the modulated DSC experiments using indium and sapphire respectively.

A series of isothermal curing experiments were used for kinetic modeling. Two DSC samples were prepared from a fresh batch of 2MEP4FS prepolymer for each experiment. A total of 4 scans were required to measure the initial T_g, reaction energy during curing, and final T_g. Here, T_g was taken as the inflection point in the reversible part of the heat flow (TA Instruments 1998).

Scan 1) One sample was immediately tested in the DSC, while the second was stored in liquid nitrogen. Sample 1 was cooled from room temperature to -80 °C over a period of 10 min, the maximum cooling rate capable by the instrument. It was then heated at 3 °C/min with ±1 °C/min sinusoidal modulation through the glass transition temperature (initial T_g).

Scan 2) Sample 2 was removed from the liquid nitrogen and rapidly heated to room temperature using large aluminum heat sinks. It was quickly loaded into the DSC, cooled to -80 °C, and heated at 30 °C/min to the desired curing temperature. The sample was held isothermally at this temperature for an extended period of time. When the heat flow was deemed to have equilibrated, the sample was cooled to room temperature.

Scan 3) Scan 2 was repeated on sample 2 to establish a baseline heat flow.

Scan 4) Sample 2 was scanned a third time using a 3 °C/min heating rate and ±1

°C/min sinusoidal modulation from room temperature through the glass

transition temperature (final T_g).

Four different curing temperatures were used for kinetic modeling: 60, 70, 80, and 90 °C.

Additional special cases are discussed later. Table 4.1 summarizes the measured results.

4.4   Conversion Rate Modeling

The conversion, α, of the polymer describes the level of cross-linking, where $\alpha=0$

indicates no cross-linking bonds are present and $\alpha=1$ is fully cured material with a

maximum number of cross-links. Conversion is given as:

$$\alpha = \frac{H_T - H_r}{H_T} \tag{4.1}$$

where H_T is the total energy of the reaction and H_r is the residual energy required to

Table 4.1   DSC experimental results for 2MEP4FS. The first four samples were used to model the reaction and estimate the total energy, H_T. The sample prepared by manually mixing the monomers at room temperature (special case 1) is considered the fully uncured case. The sample prepared by rapidly mixing the monomers at an elevated temperature (the large-sample method) is considered the fully cured case. The sample cured at 100 °C is special case 2.

Processing Method	Small	Small	Small	Small	Manual-mix only	Large	Small
Cure Temp (°C)	60	70	80	90	90	90-95	100
Initial T_g (°C)	-18.03	-17.45	-17.26	-17.36	-23.97	-	-17.83
ΔC_{p0} (mJ/g/°C)	-	-	-	-	332.88	-	-
H_m (kcal/mol DA adducts)	10.31	10.99	11.15	11.65	9.50	-	12.38
Final T_g (°C)	83.71	92.29	95.15	99.85	92.46	101.20	97.68
$\Delta C_{p\infty}$ (mJ/g/°C)	-	-	-	-	-	277.60	-

complete the polymerization. The change in conversion over time is then:

$$\frac{d\alpha}{dt} = \frac{-dH_r/dt}{H_T}$$

(4.2)

where the heat flow rate $-dH_r/dt$ is directly given by the DSC.

In the present study, the residual energy for each experiment is determined from the difference between scans 2 and 3. The majority of this energy is given off during the isothermal step of scan 2. The energy released during the temperature ramp step of scan 2 is also accounted for by considering the divergence from linearity of the heat flow as a function of temperature above T_g and relative to scan 3. The only unknown is the total energy of the reaction. Typically, this is determined by heating an uncured sample of material until all exothermic energy has been given off and the heat flow equilibrates (Sheng et al. 2008). In the present thermally reversible polymer, this is not a feasible technique as the rDA reaction will consume energy and separate the DA adduct, reducing conversion. Instead, we fit the data to the DiBenedetto equation to estimate the total energy. The equation uses the properties of fully cured and fully uncured material cases to estimate the glass transition temperature as a function of conversion (Pascault and Williams 1990; Sheng et al. 2008):

$$\frac{T_g-T_{g0}}{T_{g\infty}-T_{g0}} = \frac{\lambda\alpha}{1-(1-\lambda)\alpha}.$$

(4.3)

The glass transition temperatures T_{g0} and $T_{g\infty}$ are for the fully uncured and cured cases respectively. The parameter λ is the ratio of the change in heat capacity around the glass transition temperature of the fully cured and uncured cases: $\Delta C_{p\infty}/\Delta C_{p0}$. Here, the fully cured case is taken as the polymer prepared using the large-sample fabrication method (see Chapter 3.1.2). The large sample had been cured for 5 hours at 90-95 °C and

allowed to cool to room temperature over a period of approximately 10 hours before a small piece was broken off for DSC testing. The fully uncured case is assumed to be the monomers after manual mixing, the first step of the small-sample fabrication procedure. If the initial T_g for each curing case is assumed to be on the curve given by the DiBenedetto equation (Figure 4.1), the final T_g is given by:

$$\alpha_f = \alpha_i - \frac{\Delta H_r}{H_T}. \tag{4.4}$$

where ΔH_r is the measured change in residual heat energy. A least squares fit of all four curing cases gives an average total heat of polymerization of 12.5 kcal/mol DA adduct.

The estimated DA adduct energy is less than the 23 kcal/mol DA adduct determined by Chen et al. (2002) for 3M4F, another thermally reversible polymer.
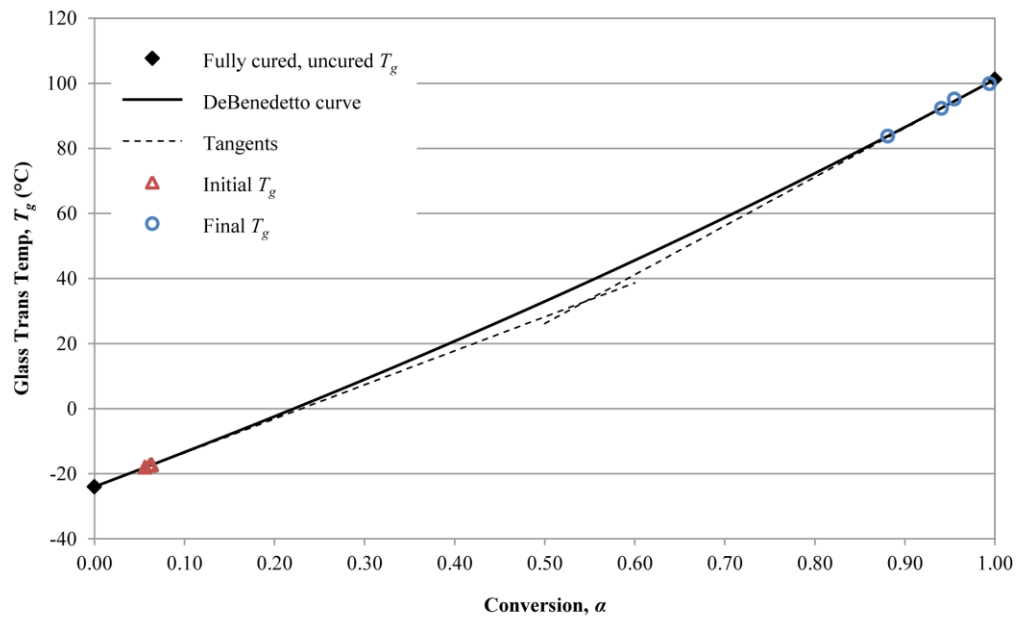
Figure 4.1 The DiBenedetto curve was developed considering the fully cured and uncured 2MEP4FS cases. The DSC data from the four curing temperatures (60, 70, 80, 90 °C) are fitted to the curve by assuming H_T. The intersection of the tangent lines from $\alpha=0$ and $\alpha=1$ gives the approximate gel point of 2MEP4FS as $\alpha_{gel}=0.545$.

Considering the bonding energies for carbon-carbon single and double bonds, the DA adduct energy is estimated to be 40 kcal/mol (Chapter 4.7). These comparisons suggest a significant number of moieties remain unreacted in the final 2MEP4FS polymer.

The rate of DA cross-link formation (rate of conversion) in 2MEP4FS varies with conversion and temperature. Two models are considered as potential candidates to approximate the kinetics of the reaction: n^{th} order and autocatalytic. An nth order reaction assumes the conversion rate decreases with the concentration of unreacted moieties according to a power law:

$$\frac{d\alpha}{dt} = k(1-\alpha)^n. \tag{4.5}$$

Conversely, an autocatalytic reaction assumes the products catalyze the reaction, leading to an initial increase, maximum, and then decrease in reaction rate as the unreacted moieties are consumed:

$$\frac{d\alpha}{dt} = k(1-\alpha)^n \alpha^m. \tag{4.6}$$

The parameters n and m are the reaction order, and the rate constant k is assumed to follow the Arrhenius relationship:

$$k(T) = A exp\left(-\frac{E_a}{RT}\right), \tag{4.7}$$

where A is a pre-exponential factor, E_a is the activation energy, R is the universal gas constant, and T is the absolute temperature. The two models exhibit significantly different behavior at low conversion: at $\alpha=0$ the nth order model predicts a maximum reaction rate, while the autocatalytic model predicts a reaction rate of zero. Since the present processing methods do not facilitate investigation of the reaction at low conversions, it is unclear from the DSC data which model is more appropriate for

2MEP4FS. Therefore, each model was fit to the DSC experimental results using a least squares method. The autocatalytic model was deemed a better fit across all four curing temperatures (R^2=0.998 versus R^2=0.994 for the fitted n^{th} order model). A physical mechanism in this reaction that would cause it to behave in an autocatalytic manner is unknown. Park et al. (2009) uses an autocatalytic model for the cross-linking of another Diels-Alder-based healable polymer, although a rationale is not given. Here, the fitted autocatalytic model (Figure 4.2) gives a total reaction order for 2MEP4FS (m=0.35 + n=1.87) of 2.22. A logarithmic fit of $\ln k$ versus $1/T$ (Figure 2 insert) gives an activation energy E_a of 55.2 kJ/mol and pre-exponential factor A of 9x10^5.
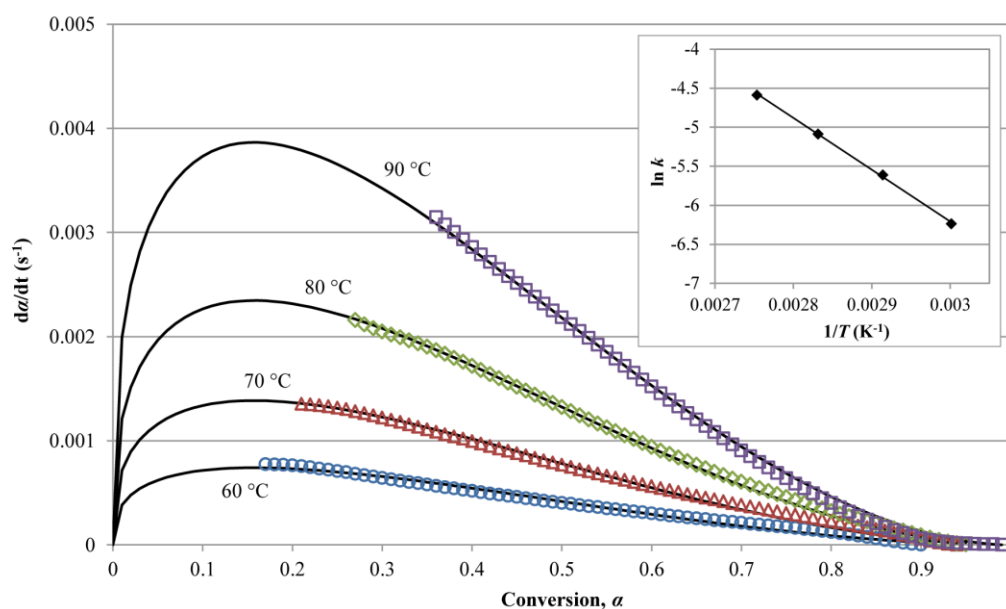
Figure 4.2   The conversion rate of 2MEP4FS as a function of conversion and temperature is fitted with the autocatalytic model (solid lines). Increasing the temperature increases the conversion rate of the polymer. Despite starting at similar initial conversions, the samples cured at higher temperatures required more heating time, leading to more conversion during the ramp step and the staggered starts in the data. The first isothermal data points were truncated as the instrument response had not yet stabilized. (insert) A linear fit of the autocatalytic model rate constants gives the parameters for the Arrhenius relationship (equation 4.7).

4.4.1   Special Case 1: Manual-mix Only

Sample preparation would be greatly simplified if the monomers could be combined at room temperature and fully cured without the intermediate steps of the small-sample processing procedure. Chen et al. (2003) used simple mixing to combine 2MEP and 4F monomers in their study. The effect of this preparation method on the reaction and final conversion of 2MEP4FS was studied using DSC.

A stoichiometric ratio of 2MEP and 4FS monomers was combined in a glass culture tube and hand mixed vigorously for approximately 5 minutes, at which time the light yellow, opaque mixture was visually homogenous. High vacuum was briefly applied to remove air trapped during mixing. Two small samples of the mixture were then transferred to aluminum DSC pans, which were subsequently sealed and tested following the previously established procedure with a 90 °C curing temperature.

Comparing the results of the manually-mixed sample with the expected behavior given by the DiBenedetto curve, the change in conversion (calculated from the measured energy released during polymerization) is underpredicted given the measured change in T_g. A likely explanation for the missing energy is that it has gone into melting small 2MEP particles that were not fully dissolved in the 4FS. Due to the energy consumed during the reaction, estimating the conversion rate for comparison with the fitted autocatalytic model is problematic. Particularly, the conversion rate is initially determined to be negative as energy is consumed by the sample during the initial portion of the reaction. The final T_g of the manually-mixed 2MEP4FS is 7.4 °C below the final T_g of the 2MEP4FS prepared according to the small-sample procedure. Incomplete mixing of the monomers could lead to the formation of fewer cross-linking bonds in the

final polymer. During the small-sample processing procedure, the rapid heating of the monomers melts the 2MEP and lowers the viscosity of the mixture, while the high vacuum leads to violent bubbling as trapped gasses are pulled out. This bubbling likely enhances mixing of the monomers, leading to a prepolymer that is more homogeneous than that achieved by manual mixing alone.

4.4.2 Special Case 2: High Temperature Cure

Next, we investigate the effect of curing the 2MEP4FS prepolymer at 100 °C, which is near $T_{g\infty}$. Plaisted and Nemat-Nasser (2007) cured their 2MEP4FS at this temperature, and subsequently obtained excellent crack healing results, even demonstrating improved resistance to fracture after healing. In the present study, 2MEP4FS prepolymer was prepared according to the standard small-sample processing procedure and tested following the aforementioned DSC method using a 100 °C curing temperature. The conversion rate is observed to be lower than predicted by the fitted autocatalytic model (Figure 4.3). The total measured energy also suggests a final conversion of $\alpha=1.05$, meaning there should be more cross-links formed than in the material produced using the large-sample processing method, which had been cured at 90-95 °C. DSC measurements of the 100 °C cured sample give a final conversion of $\alpha=0.98$, indicating there are fewer cross-links after the curing process has completed and the sample has cooled. The retro-Diels-Alder (rDA) reaction offers a possible explanation for these observations. During curing at 100 °C, the DA and rDA reactions may both be occurring, slowing the overall rate of cross-link formation. The literature gives the rDA reaction as starting at 110 °C (Chen et al. 2003), but this observation was
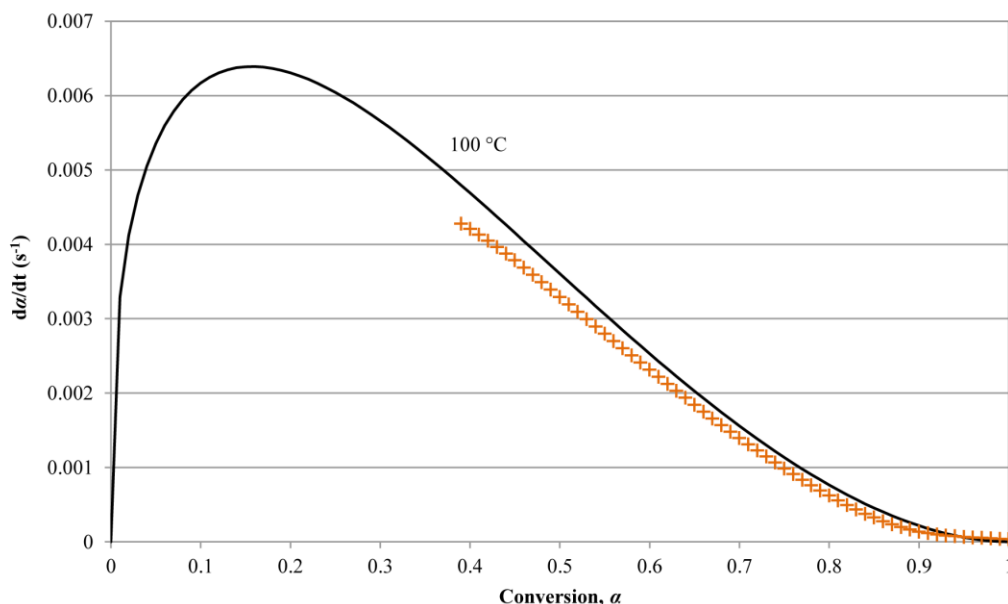
Figure 4.3   The experimentally measured conversion rate of 2MEP4FS at 100 °C is compared with the rate predicted by the fitted autocatalytic model (solid line).

made based on dynamic DSC scans. It's possible the onset of the rDA reaction is earlier. Assuming the rDA reaction is occurring, increased moiety mobility due to softening of the material at the glass transition temperature and additional thermal energy could lead to more cross-links being formed despite the rDA reaction. Once the material cools, however, the rDA reaction reduces the overall conversion of the sample. This explanation suggests that there is a maximum level of cross-linking for the polymer, and it is below the total number of DA adducts possible.

4.4.3   Special Case 3: Room Temperature Cure

After preparation according to the small-sample processing method, the 2MEP4FS prepolymer is at room temperature (22 °C). During previous experiments, the prepolymer spent only a minimal amount of time at this temperature before being cured

at an elevated temperature. But, if the prepolymer is subsequently worked with or used elsewhere such as in a composite prepreg, it could spend an extended period of time at room temperature. We seek to evaluate the rate of cross-link formation at ambient conditions. Since the fitted autocatalytic model predicts a slow rate of conversion at room temperature, measuring the heat flow over an extended period of time using DSC as previously done is not practical. Instead, a series of prepolymer DSC samples were tested after different periods of time at room temperature. By comparing the change in T_g between samples, an average conversion rate can be estimated and compared with the predicted autocatalytic behavior.

Seven DSC samples were created from one 2MEP4FS prepolymer preparation and tested after nominal periods of 8 min, 30 min, 1 hr, 3 hr, 6 hr, 1 day, and 3 days at room temperature. Since the modulated DSC test requires approximately 1 hour for a complete scan according to the previously established procedure, the 30 min and 1 hr samples were held at room temperature and then stored in liquid nitrogen until the instrument was ready. The DiBenedetto equation (4.3) is used to translate the observed T_g to conversion, α. The change in conversion between samples gives a series of average conversion rates. These rates are significantly lower than those predicted by the fitted autocatalytic model (Figure 4.4). The reason for this discrepancy is not clear. Room temperature is significantly below the temperature range used to fit the autocatalytic model, and the predicted conversion rates are very slow. At 22 °C, there may be insufficient thermal energy to overcome energy barriers to the reaction. Another possibility is the 2MEP monomer is precipitating out of the 4FS. During the small-sample process, the 2MEP is melted and dispersed in the 4FS. But, since the material is
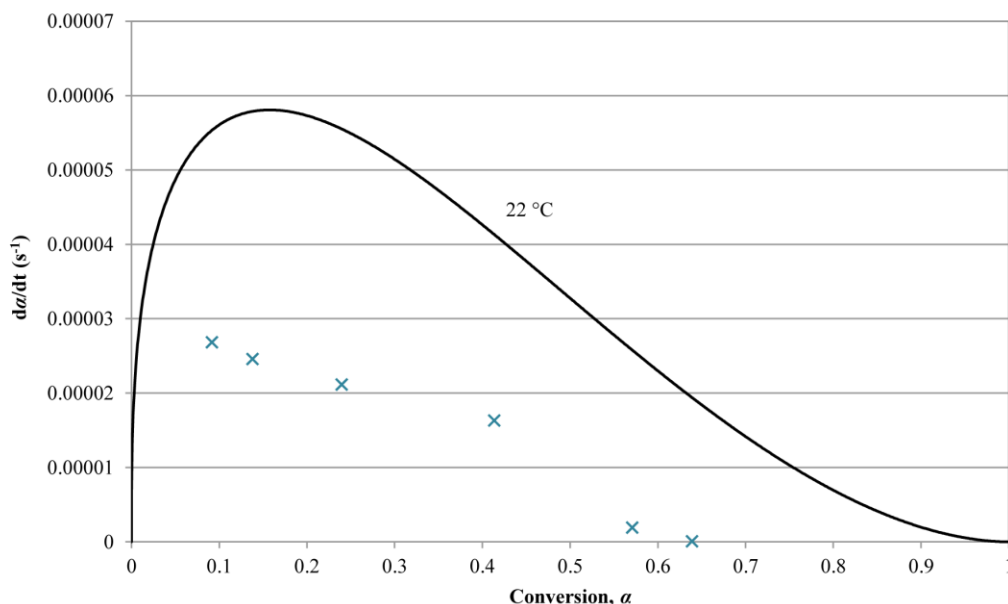
Figure 4.4   Average conversion rates of 2MEP4FS at room temperature (22 °C) are compared with the rate predicted by the fitted autocatalytic model (solid line).

cooled before significant cross-linking occurs, there are still large quantities of unreacted 2MEP monomers.   At room temperature, there could be a crystallization process competing with and inhibiting polymerization.

A visual investigation was conducted using a series of 2MEP4FS polymer films. The first film was prepared following the initial portion of the small-sample processing method, but without quenching.   Instead, the hot prepolymer was removed from the culture tube and placed between two nylon films in a preheated 90 °C oven. Two more films were prepared following the entire small-sample processing method, with the room temperature prepolymer distributed between nylon films. The prepolymer was held at room temperature for 5 min and 1 day respectively, before being cured at 90 °C. Observed using cross-polarized light microscopy, the three 2MEP4FS films have bright

regions that could be caused by small crystals (Figure 4.5). The number of these bright regions increases with the time the prepolymer spends at room temperature before final curing. It was noted that the density of the bright regions did not change as a result of curing.

If the crystals are 2MEP precipitates, the final conversion of the 2MEP4FS polymer may be reduced. A new series of three prepolymer DSC samples were prepared following the small-sample processing method. The samples were held at room temperature for 1 hr, 4 hr, and 1 day respectively before being curing at 90 °C in the DSC. After curing, each sample was scanned to estimate final T_g (scan 4), and the associated conversion was normalized by the conversion obtained for the earlier 90 °C cured sample that had spent minimal time at room temperature. The results show no significant changes, with normalized final conversions of 1.0041, 0.9999, and 1.0004 respectively. The consistent results indicate that time at room temperature does not negatively affect cross-linking in the final, cured 2MEP4FS polymer. Since the low final conversion of the manual-mix only case (special case 1) was attributed to poor mixing of the monomers, the present results suggest the observed crystalline regions may not be 2MEP precipitates.
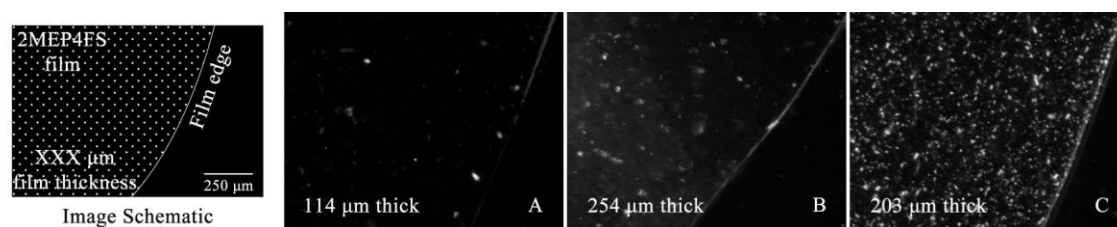
Figure 4.5 Polarized light microscopy images of 2MEP4FS polymer films cured at 90 °C after the prepolymer spent (A) zero time, (B) 5 min, and (C) 24 hr at room temperature.

4.5   Application to Viscosity Measurements

The formation of cross-linking bonds in 2MEP4FS leads to changes in thermal and mechanical properties. In the previous section, the change in glass transition temperature was explored and related to the conversion of the polymer. Using this relationship, we seek to correlate 2MEP4FS prepolymer viscosity with conversion.

Viscosity is a measure of the resistance to flow of a fluid subjected to mechanical shearing. During polymerization, the prepolymer will initially have a minimum viscosity. As cross-linking between the monomers proceeds, the average molecular weight and viscosity increase, eventually going to infinity when the material becomes solid. At this gel point, a continuous polymer network has formed. The evolution of viscosity with conversion and the gel point are important parameters for processing the prepolymer, particularly in composite applications.

There are a number of standard viscosity measurement techniques available. Calibrated funnels or capillary tubes can be used to estimate viscosity based on the movement of the fluid as a function of time (Washburn 1921). A falling sphere (or rising bubble) viscometer relies on a sphere moving through a fluid at terminal velocity (ASTM D1343 2006). Stokes law relates this velocity with a drag force, which depends on viscosity. Ghezzo et al. (2010) successfully used the falling sphere method to characterize the viscosity of 2MEP4F prepolymer as a function of time and temperature. Rotational viscometers apply an external torque to an object in the fluid to produce angular rotation (ASTM D2983 2009). The relationship between torque and angular speed is related to the viscosity of the fluid. Rotational viscometers include the cup and bob, cone and plate, and electromagnetically spinning sphere types (Sakai et al. 2010).

Plaisted (2007) used a cone and plate viscometer to estimate the initial viscosity of 2MEP4FS prepolymer as 0.112 Pa·s (112 cP) at 90 °C.

4.5.1   Experimental Setup

In the present work, a cup and bob-type rotational viscometer is modified to make measurements directly inside the production culture tube. This approach offers several benefits. Following the small-sample processing method yields prepolymer at a minimum initial conversion, but the limited quantity of material (< 0.3 mL) precludes most of the aforementioned viscosity methods. The electromagnetically spinning sphere approach is possible but limited to 10 Pa·s (Sakai et al. 2010), which is too low for the present materials at room temperature. Effectively transferring this small quantity of prepolymer to a cone and plate-type viscometer would be challenging.

A Brookfield HADVII+ viscometer was adapted to turn a custom spindle inside a culture tube containing the prepolymer. The spindle had a hemispherical end and was fabricated from 5/16 inch precision steel rod. A threaded hole was machined into the opposite end, allowing it to be screwed onto the motor shaft of the viscometer. The 10x75 mm borosilicate glass culture tube was mounted in a bracket, which was slid up and into position using a pair of linear bearings riding along precision steel shafts. A ring mounted on one shaft between the bracket and the instrument acted as a stop, enabling the culture tube to be reliably positioned such that the gap around the spindle was estimated to be constant. Nylon set screws secured the culture tube and bracket in position. A picture of the setup and important dimensions are given in Figure 4.6. Measurements were made by recording the height of the fluid in the culture tube and the
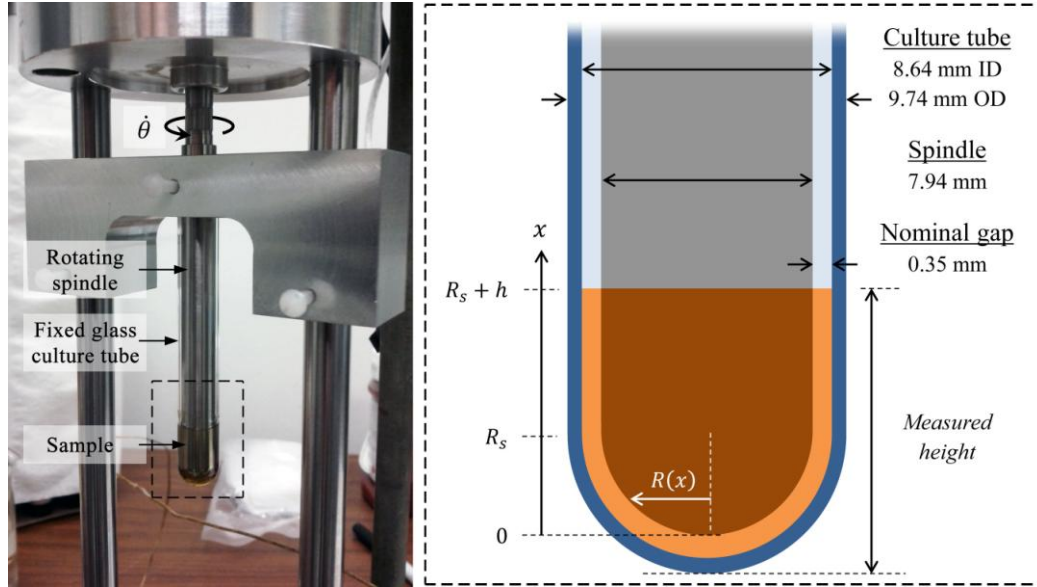
Figure 4.6 The modified rotational viscometer system with relevant dimensions. The modifications allow measurements to be made inside the glass culture tube used to produce the 2MEP4FS prepolymer.

torque required to turn the spindle at the prescribed rotational speed: 200, 105, 10, 5, 1, or 0.1 rev/min. The useful torque range of the instrument was between 10 % and 100 % of the maximum torque, 1.437 mN·m. Since the fluid thickness is small, the torque, T, is related to the dynamic viscosity, η, by assuming a linear variation in Newtonian fluid displacement between the rotating spindle and fixed culture tube:

$$T = \int_0^{R_s+h} \frac{2\pi\eta R(x)^3 \dot{\theta}}{R_t - R_s} dx, \tag{4.8}$$

where $\dot{\theta}$ is the angular speed (rad/sec), R_s is the radius of the spindle, and R_t is the inner radius of the culture tube. Performing the integration and rearranging yields the estimated viscosity:

$$\eta = \frac{8T(R_t - R_s)}{\dot{\theta}\left(3\pi^2 R_s^4 + 16\pi h R_s^3\right)}. \tag{4.9}$$

Viscosity results from the experimental setup were found to underpredict the true viscosity of a known fluid by ~11 % (Chapter 4.8). For the application of 2MEP4FS as the matrix in prepreg composite layers, this constitutes a reasonable estimate.

4.5.2   Room Temperature Measurements

Viscosity measurements were performed at room temperature (22 °C) for neat 4FS and 2MEP4FS prepolymer prepared according to the small-sample procedure. The 4FS monomer exhibited an average viscosity of 94 Pa·s (940 P) at 5 rev/min rotational speed with a measured sample height of 10.2 mm. The initial measurement of 2MEP4FS prepolymer was 345 Pa·s (3450 P) at 1 rev/min with a measured sample height of 20.6 mm.   The viscosity of the 2MEP4FS prepolymer was tracked as polymerization proceeded (Figure 4.7), until the required torque exceeded the capability of the instrument.   Since approximately 10 minutes elapsed between the completion of the small-sample processing method and the first viscosity measurement, an exponential fit of the data gives the initial viscosity of the 2MEP4FS prepolymer as 208 Pa·s (2080 P). This indicates that the combination of the 2MEP and 4FS monomers roughly doubles the viscosity of the 4FS monomer alone at room temperature.

Two DSC samples were prepared from the 2MEP4FS prepolymer immediately after completion of the small-sample processing method. The samples were tested at time periods coinciding with the beginning and end of viscosity measurements to obtain the T_g of the prepolymer at these points. The glass transition temperature associated with the first sample was correlated with polymer conversion. Using the average conversion rates previously determined at room temperature, the 2MEP4FS viscosity data points
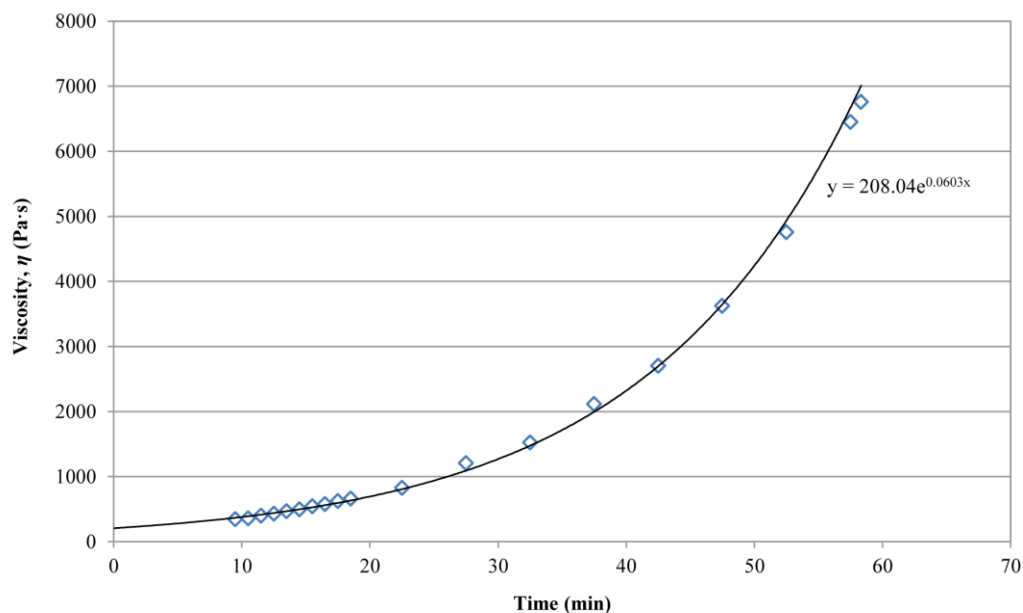
Figure 4.7 The viscosity of 2MEP4FS prepolymer as a function of time at room temperature after the conclusion of the small-sample processing method. The exponential fit gives an initial viscosity of 208 Pa·s.

were correlated with the conversion. During testing, the second DSC sample was stored near the instrument to maintain a similar sample temperature. The second DSC-measured T_g indicates very good agreement between the predicted and measured conversions (< 0.3 % difference).

4.5.3 Elevated Temperature Measurements

Since the 2MEP4FS prepolymer needs to be cured at an elevated temperature to achieve maximum cross-linking, knowledge of the viscosity at such a temperature is useful. A new prepolymer sample was prepared according to the small-sample processing method, and a DSC sample was taken to measure the initial T_g. The viscometer spindle and a large oil bath had been preheated to 90 °C. The hot spindle was

quickly attached to the viscometer, and the room temperature culture tube was mounted and slid into position. The bottom half of the apparatus was then lowered into the oil bath. A video camera recorded the time, torque, and rotational speed for later analysis. Initially, the sample required the highest rotational speed, 200 rev/min, in order to effectively measure the torque. This speed was periodically stepped down as the polymerization proceeded and the torque would reach 100 %. Once the required torque exceeded the capability of the instrument at the lowest rotational speed, the instrument was turned off and raised out of the bath. The culture tube and spindle were quickly cooled and separated, leaving the 2MEP4FS intact as a thin film inside the culture tube. The height of the polymer was measured as 25.4 mm, and a small sample was removed for DSC testing to determine final T_g. The initial and final T_g were used with the DiBennedeto equation and the fitted autocatalytic model to estimate viscosity as a function of conversion (Figure 4.8).

Given the initial and final conversions (α_i=0.075, α_f=0.577) and the observed time between them (~7 min), numerical integration of the autocatalytic model gives an average polymerization temperature of 73.1 °C. This is significantly lower than the 90 °C oil bath where the experiment was conducted. The discrepancy can be attributed to a non-constant sample temperature over the course of the test. The spindle had been preheated in an oven, but it had to be taken out and attached to the viscometer prior to sliding the sample into position and lowering the apparatus into the hot bath. The cooling associated with this delay coupled with the sample starting at room temperature likely meant the prepolymer did not approach 90 °C until later in the experiment. The average polymerization temperature is weighted by conversion rate. Since the maximum
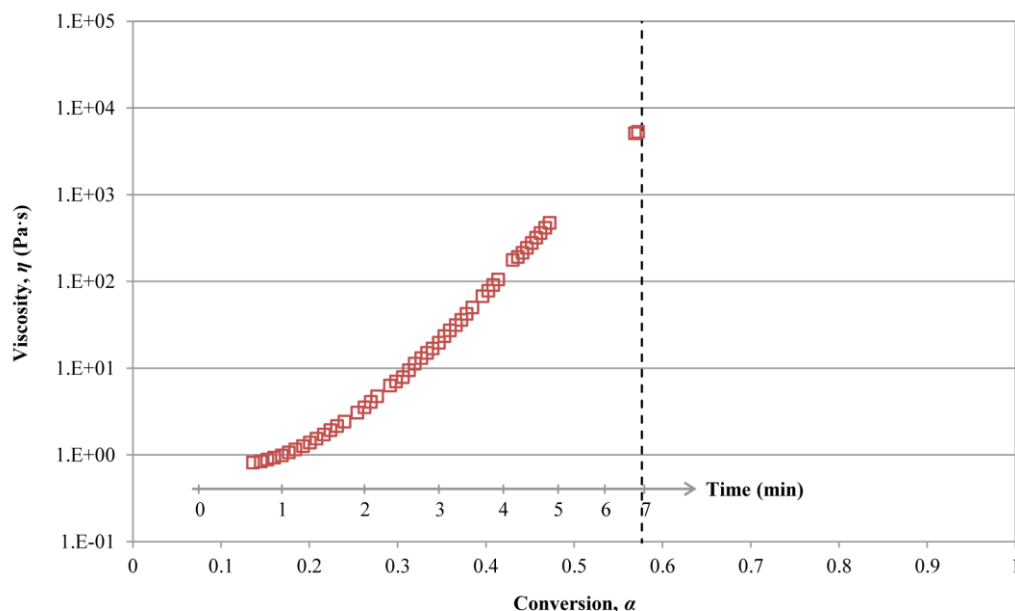
Figure 4.8   The viscosity of 2MEP4FS prepolymer measured in a 90 °C oil bath. The dashed line gives the estimated gel point of the polymer as measured by DSC at the conclusion of the viscosity test. The gaps in the data are due to delays waiting for the reading to stabilize after stepping down the rotational rate of the spindle.

conversion rate for any given temperature occurs at low conversions, an initial period of low temperature will disproportionately skew the average temperature down.   The viscosity data suggest the temperature was relatively low at the start of the test.   The initial viscosity measurement was 0.817 Pa·s (817 cP), which is higher than the 0.112 Pa·s estimated by Plaisted (2007).   Decreasing the temperature would increase the viscosity. Thermal expansion effects on the geometry of the experiment are estimated to be small and were not considered in the calculations.

The final conversion, $\alpha_f=0.577$, can be taken as the approximate gel point of the polymer. Another estimate of the gel point is given by the Flory-Stockmayer equation (Flory 1953):

$$\alpha_{gel} = \frac{1}{\sqrt{r(f_F-1)(f_M-1)}}, \qquad (4.10)$$

where r is the stoichiometric ratio, is f_F the functionality of furan, and f_M is the functionality of maleimide. This equation gives the gel point for stoichiometric 2MEP4FS as α_{gel}=0.577, which matches the DSC-measured estimate. A third estimate of gelation is given by the intersection of the tangents at α=0 and α=1 on the DiBenedetto curve (Figure 4.1) (Wingard 2000). This method gives a gel point of α_{gel}=0.545. For a true measurement of the gel point, dynamic rheometric analysis should be used to find the point where $\tan \delta$ becomes frequency independent (Holly et al. 1988).

4.6   Discussion and Conclusions

The conversion and conversion rate models are useful tools for estimating the number of Diels-Alder cross-links in 2MEP4FS as a function of glass transition temperature, time, and sample temperature. Using DSC measurements and the DiBenedetto relationship between T_g and conversion, the total energy of the reaction was estimated to be 12.5 kcal/mol DA adduct. Comparing this result with another DA adduct measurement in the literature (23 kcal/mol, Chen et al. 2002) and a simple theoretical estimate (40 kcal/mol, Chapter 4.7) suggests that even at the maximum measured conversion, a significant portion of potential DA adducts are unformed in 2MEP4FS. Based on the theoretical estimate, only 31 % of the potential DA adducts are established when α=1. The energy we measured during DSC experiments included the temperature ramp and isothermal portions of the test. It could be argued that these measurements

miss the initial energy given off during manual mixing of the monomers. While true, estimating the elapsed time and the initial reaction rate at room temperature suggests the missed energy accounts for less than 1 % conversion.

The conversion rate model was determined by fitting DSC data for 2MEP4FS cured isothermally at temperatures ranging from 60 °C to 90 °C. Assuming an autocatalytic reaction provided a better fit of the data than an nth order model. These two approximations exhibit significantly different behaviors at low conversion levels, but due to the processing method and temperature ramp, this period of the reaction was not captured. Outside of the fitted temperature range, the conversion rate was underpredicted by the model. At room temperature, insufficient thermal energy to overcome energy barriers or other processes like crystallization could be inhibiting polymerization. The time spent at room temperature before curing at an elevated temperature did not affect the final conversion of the polymer. At 100 °C, the rDA reaction could be separating DA adducts, although this is 10 °C below the estimated onset observed in the literature (Chen et al. 2002; Chen et al. 2003). The rDA reaction would reduce the conversion rate and final conversion of the polymer. The final conversion was found to be highest for 2MEP4FS cured at 90-95 °C.

The small-sample processing method provided an efficient method for effectively mixing small quantities of 2MEP and 4FS monomers, while minimizing the initial conversion. Manual mixing of the monomers was determined to be insufficient to obtain maximum conversion in the final, cured polymer. The developed approach will be useful in future experiments where the 2MEP4FS prepolymer must be manipulated before final curing, such as preparing unidirectional fiber prepreg layers and multilayered healable

composites. The small-sample approach conserves monomer supplies, but experiments must be modified to use small quantities of material. Here, a rotational viscometer was adapted to make viscosity measurements on the small quantity of prepolymer. At room temperature, the prepolymer was estimated to have an initial viscosity approximately twice that of neat 4FS. In a hot oil bath, the first viscosity measurement of 2MEP4FS prepolymer was higher than others have estimated, but DSC results and the autocatalytic model indicate the sample had not yet reached the bath temperature. Modifications to the experimental setup or an alternative approach, such as the electromagnetic spinning sphere, could reduce the temperature variability.

Rotational viscometer measurements were made as a function of time and combined with DSC measurements of T_g to estimate viscosity as a function of conversion. The final conversion of the viscosity sample tested at an elevated temperature was taken as the gel point. Since the final viscosity measurement is limited by the torque capability of the instrument, the quantity of prepolymer in the culture tube will influence the end of the experiment. This suggests the gel point of 2MEP4FS is underpredicted, even though the estimate agrees reasonably well with estimates determined by other methods. Dynamic rheometric analysis would be useful here for monitoring the complex viscosity during polymerization and obtaining a better determination of the gel point.

The developed models can be used to characterize additional mechanical properties of 2MEP4FS as a function of conversion. Fracture toughness would be one property of particular interest, given the healing capability of this polymer. Plaisted and Nemat-Nasser (2007) studied the fracture and healing behavior of 2MEP4FS, and found

that under ideal conditions, samples required more stress to propagate cracks after healing than in their virgin state (Figure 7.4). The samples had been cured at 100 °C for an extended period of time. In a separate DSC study, Plaisted (2007) determines the T_g of the cured 2MEP4FS to be 93 °C. Assuming this polymer has been treated comparably to the polymer used in the fracture study, the data presented here suggest that the conversion of the samples was below the maximum level; they were not fully cured. After fracture, the samples were healed at a temperature of 95 °C, which happens to be the approximate temperature found to achieve maximum cross-linking in 2MEP4FS. Additionally, if there are a significant number of unreacted functional groups in the polymer sample, there would be a surplus of moieties at the fracture surface available to heal the crack. Hence, the present conversion study offers a rational explanation for the observed increase in fracture resistance. New fracture measurements of 2MEP4FS at different levels of conversion will be considered in future work.

4.7   Appendix A: Diels-Alder Adduct Energy

A carbon-carbon single bond gives off 347 kJ/mol, while a carbon-carbon double bond gives off 611 kJ/mol (Wade 1991). The Diels-Alder reaction converts the three double bonds and one single bond of the diene and dienophile moieties to a cyclohexane ring with one double bond and five single bonds. This process requires 2180 kJ/mol reactants and releases 2346 kJ/mol product, resulting in an exothermic reaction of 166 kJ/mol or 40 kcal/mol DA adduct.

4.8   Appendix B: Viscosity Measurement Validation

Since the Brookfield HADVII+ rotational viscometer was modified to make measurements inside glass culture tubes, the accuracy of the measurements was investigated using corn syrup. The syrup was first tested using a falling sphere technique at room temperature. The same syrup was then tested in the rotational viscometer, and the results were compared.

4.8.1   Falling Sphere Viscometer

A 25 mL graduated cylinder was filled with Karo Dark Corn Syrup. The cylinder was backlit and photographed with a Nikon D70 SLR camera externally controlled by an electronic trigger programmed to take a picture every four seconds. A 1/16 inch chrome steel ball bearing was dropped in the center of the cylinder opening and allowed to fall to the bottom of the cylinder. The test was conducted 3 times. Subsequent image analysis was used to determine the velocity of the ball bearing between every two pictures. Assuming no inertial effects (Re<<1), a modified Stokes equation can be used to related the movement of the ball bearing due to gravity with the opposing drag force due to the viscosity, η:

$$\eta = K \frac{2gr_b^2(\rho_b - \rho_c)}{9s}, \tag{4.11}$$

where g is acceleration due to gravity, ρ_b is the mass density of the ball bearing (7.99 g/cm3), ρ_c is the mass density of the corn syrup (1.40 g/cm3), r_b is the radius of the ball bearing, and s is the measured speed of the ball bearing. Here, the corrective factor, K,

accounts for the finite size of the sphere relative to the inner diameter of the cylinder, D=19.11 mm (ASTM D1343 2006):

$$K = 1 - 2.104 \left(\frac{2r_b}{D}\right) + 2.09 \left(\frac{2r_b}{D}\right)^3. \tag{4.12}$$

Each test had 10 useful pictures, yielding 9 speeds. The average viscosity of each test is given in Figure 4.9. The average viscosity of all three tests is 5.77 ± 0.15 Pa·s.

4.8.2 Rotational Viscometer

Small amounts of corn syrup were transferred from the graduated cylinder to a 10x75 mm borosilicate glass culture tube. Three rotational measurements were performed at three different fluid heights: nominally 10 mm, 15 mm, and 30 mm. For each test, a rotational speed was selected such that the required torque could be measured by the viscometer. Using equation (4.9), the viscosity of the corn syrup was estimated (Figure 4.9). The average viscosity of all three fluid levels is 4.92 ± 0.30 Pa·s. The rotational viscometer underpredicts the viscosity measured by the falling sphere method by an average of ~11 %.
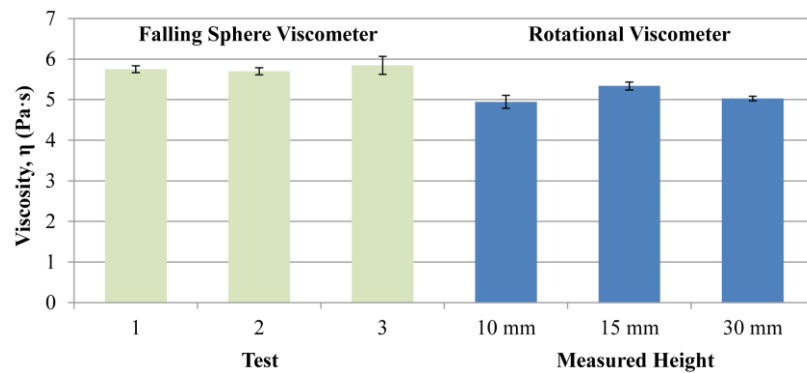
Figure 4.9 The results of the falling sphere viscometer and modified rotational viscometer for corn syrup measured at room temperature.

This chapter was a reprint of a paper in preparation entitled "Thermally reversible cross-links in a healable polymer: estimating the quantity, rate of formation, and effect on viscosity". The dissertation author was the primary investigator and author of this work. The guidance and contributions of co-authors H. Weizman and S. Nemat-Nasser are gratefully acknowledged.

Chapter 5

The DCDC Fracture Test: Experiments and Computational Modeling

The double cleavage drilled compression (DCDC) fracture test was investigated for application to crack healing research. The ability to test samples with uncommon dimensions and still obtain useful results would allow samples to be used for multiple purposes, conserving material quantities.

5.1   Introduction

The double cleavage drilled compression (DCDC) test is a suitable method for evaluating the fracture properties of brittle materials. Originally applied to glass (Janssen 1974), the test has been successfully applied to other materials (He et al. 1995; Indonje et al. 1993; Plaisted et al. 2006; Plaisted and Nemat-Nasser 2007) and interfaces in bi-material sandwiches (Turner et al. 1995). The DCDC test subjects a column of material with rectangular cross-section and central circular hole to uniaxial compression (Figure 5.1). The geometry and Poisson's effect create regions of tension at the apex and base of the hole, leading to mode I cracks. As the axial compression is increased, the cracks are driven along the length of the sample, slowly at first and then more quickly, until being arrested by frictionally-constrained end conditions.

Most DCDC experiments published in the literature have been conducted using increments of load to grow the cracks. Plaisted et al. (2006) used displacement control
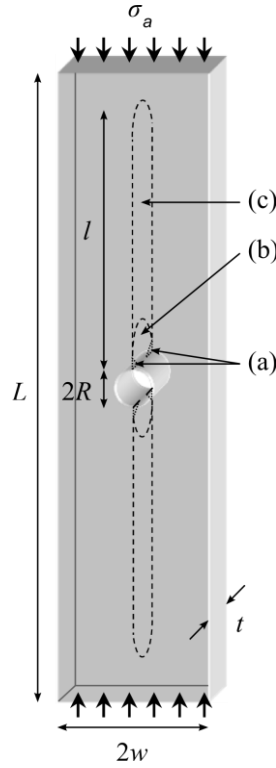
Figure 5.1 A DCDC sample. Under compression, pre-cracks (a) grow together to form cracks (b), which grow along the height of the sample (c).

for DCDC testing and observed two regimes of crack growth. The importance of sample height, width, and hole size was investigated. A theoretical model was developed combining short and long crack approximations. The model treats a DCDC sample with short cracks as an infinite plate containing a hole, with corrective factors accounting for the finite width. Once the cracks are sufficiently long, the DCDC sample is treated as a structure consisting of four beams bending under axial compression.

The DCDC geometry has been used to quantify healing in re-mendable polymers (Plaisted and Nemat-Nasser 2007) and polymers containing microvascular networks (Hamilton et. al 2010). There are several aspects of the DCDC configuration that lends itself to studying healing in these materials. Unlike the standard compact tension test,

crack growth in DCDC samples is generally stable, and the crack length can be controlled by the applied compression. Since the cracks cease to grow before they reach the ends of the sample, the sample remains in one piece, allowing the crack faces to be brought together after unloading. This maximizes contact between the crack faces, which is necessary for effective healing. After the cracks have been healed, the sample can be retested. The new cracks will initiate and grow essentially in the same manner and over the same path as in the original virgin sample.

Healable materials can be difficult to produce and are often available in limited quantities. Repurposing a sample is one way to conserve material, but compromises must be made on the sample geometry to make it suitable for all experiments. Reviewing the DCDC literature, there is limited information on the effect of only some geometric parameters on the observed fracture behavior. In the present work, we investigate the effect of sample thickness and hole size using a readily available polymer: poly(methyl methacrylate) (PMMA). We complement this experimental work with a systematic computational simulation to estimate the critical stress intensity factor from the experimental data.

5.2   Experimental Procedure

DCDC samples were machined from a sheet of Cyro Acrylite GP (PMMA) (Table 5.1). The samples were 50 mm tall and 12 mm wide, with 3, 4, 5, 8, and 11 mm thicknesses. Most of the samples contained a 3 mm diameter central hole, giving a half-width-to-hole radius (w/R) ratio of 4. Two of the 3 mm thick samples contained a 2 mm diameter hole for a w/R ratio of 6. The front and back faces of all samples were polished

Table 5.1   Nominal DCDC sample geometries and whether cracks were initiated via load cycling.

Sample	L (mm)	w (mm)	t (mm)	R (mm)	w/R	Load Cycled
3mm-1	50	6	3	1.5	4	Yes
3mm-2	50	6	3	1.5	4	Yes
3mm-3	50	6	3	1.5	4	Yes
3mm-4	50	6	3	1.5	4	Yes
3mm-5	50	6	3	1.0	6	No
3mm-6	50	6	3	1.0	6	Yes (in LN_2)
4mm-1	50	6	4	1.5	4	Yes
4mm-2	50	6	4	1.5	4	Yes
5mm-1	50	6	5	1.5	4	Yes
5mm-2	50	6	5	1.5	4	Yes
5mm-3	50	6	5	1.5	4	Yes
8mm-1	50	6	8	1.5	4	Yes
8mm-2	50	6	8	1.5	4	Yes
11mm-1	50	6	11	1.5	4	Yes
11mm-2	50	6	11	1.5	4	Yes
11mm-3	50	6	11	1.5	4	Yes
11mm-4	50	6	11	1.5	4	No
Photoelastic	50	8	8	2.0	4	Yes

so the cracks could be clearly seen, while the remaining sides were left as machined. To prevent out-of-plane buckling, the 3, 4, and 5 mm thick samples were tested in a brace. The brace consisted of two acrylic plates loosely bolted together around the sample (Figure 5.2). Cutouts in the plates allowed a clear view of the hole and cracks during testing. The supported faces of the $w/R=4$ samples were lubricated with vacuum grease to reduce interfacial friction between the samples and brace. The brace-sample interfaces of the $w/R=6$ samples were not lubricated, as the experiments were performed much earlier than the $w/R=4$ cases, and friction was not noted as a problem. The $w/R=6$ samples required significantly higher axial stresses for crack propagation due to the smaller hole size, an effect that dominated frictional problems.
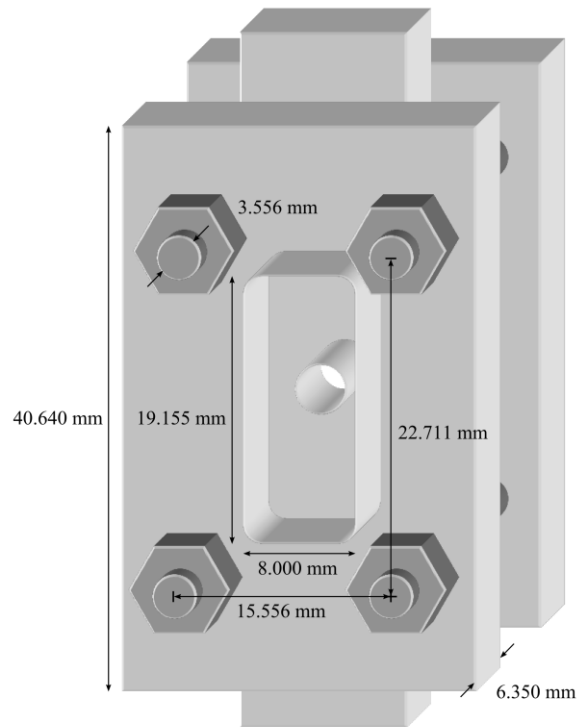
Figure 5.2   Thin samples (3, 4, and 5 mm thick) were fitted with a PMMA brace to prevent buckling out of the sample plane.

Before DCDC testing, a razor blade was used to create 1 mm deep triangular notches in the apex and base of the hole on the front and back of each DCDC sample. This method of pre-cracking was found to be necessary for effective crack initiation in PMMA samples (Plaisted et al. 2006). In the present work, this method was determined to be insufficient for thin w/R=4 samples, as the stored energy before crack initiation was sufficient to start the cracks and propagate them to the ends of the sample. By cycling the applied load and incrementally increasing the maximum compressive stress, the formation and initial growth of the cracks could be carefully controlled. A procedure using 1 Hz sinusoidal load cycling with a 3 MPa increase in peak stress every 120 seconds (Figure 5.3) was developed to supplement the notching.   This scheme was
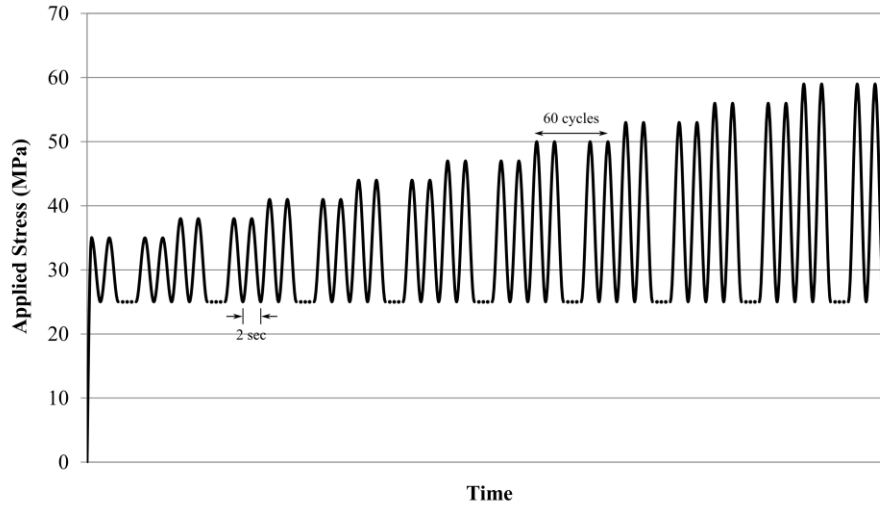
Figure 5.3   Load cycling profile for w/R=4 samples.   The stress was cycled between 25 MPa and a peak value ranging from 35 MPa to 59 MPa in 3 MPa increments. The period of each cycle was 2 seconds, and there were 60 periods for each level of peak stress. The cycling was stopped once cracks had fully formed between the notches.

applied to most DCDC samples (see Table 5.1). A different load cycling procedure was

applied to w/R=6 sample 3mm-6 (this notation gives the thickness and a sample number)

in order to initiate cracks without producing inelastic deformations. For this, the sample

was held in a bath of liquid nitrogen while the applied compression was linearly

increased to 125 MPa in one minute, sinusoidally cycled from 125 to 175 MPa at 1 Hz,

and then linearly decreased to zero in one minute. After load cycling, all samples were

unloaded and left overnight to allow any residual stresses to dissipate before DCDC

testing.

Compression was applied using an MTS 309.20 load frame with a 22.2 kN load

cell at a constant 0.5 µm/sec displacement rate. This rate was chosen to be slower than

the 0.9 µm/sec average displacement rate used by Plaisted et al. (2006). For comparison,

a PMMA sample of similar dimensions to a w/R=4 geometry used by Plaisted was tested

using the constant displacement rate and showed excellent agreement with Plaisted's results. During testing, the sample was loaded by flat, polished maraging steel plungers, 19 mm in diameter, guided by linear bearings in an aluminum frame. Photographs were taken every 30 seconds using a Nikon D70 SLR camera with Micro-Nikkor 70-180 mm ED lens. The autofocus-assist light of the camera was detected by a photoresistor and recorded in the data to allow each picture to be synchronized with the applied load from the load cell. The crack length in each picture was measured by counting pixels and normalized by the number of pixels that measured the hole radius in the undeformed sample. The nominal applied stress was determined using the applied load and undeformed cross-sectional area.

5.3   Experimental Results

Four snapshots of a representative test are shown in Figure 5.4. For the cases where load cycling was performed, the notches were grown into through-thickness cracks with a normalized length (l/R) of approximately 0.7 to 1.0. During DCDC testing, the cracks developed a pronounced thumbnail shape with the maximum height in the middle of the sample and minimum height at the free surfaces. The two cracks propagated axially, away from the central hole, as the axial compression gradually increased. The crack growth was slow at first, requiring relatively large load increments for relatively small increases in crack length. This stage is termed the short crack regime. After a normalized crack length of approximately 1.5 was reached, the crack extension began to accelerate. Beyond a normalized crack length of about 2, the cracks grew by significant lengths with minimal increases in load. This is the long crack regime, where the sample

(a)   (b)   (c)   (d)
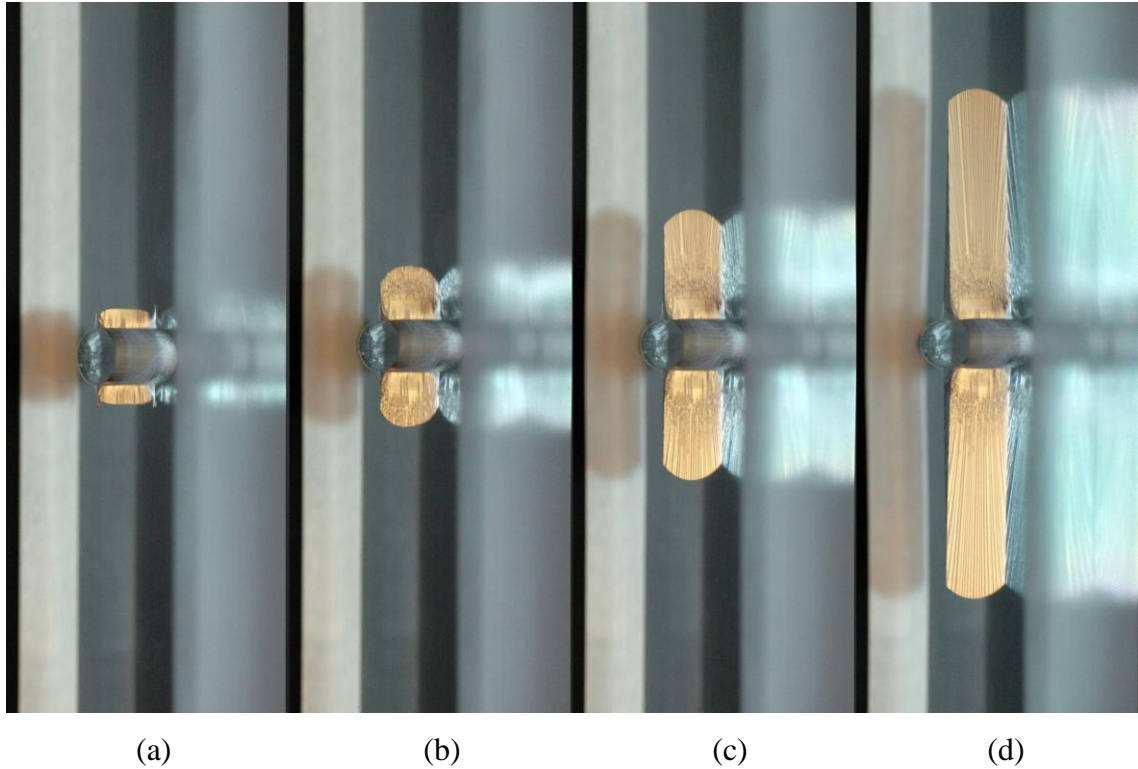
Figure 5.4   A DCDC test (8mm-2). (a) Load cycling has been completed and the pre-cracks have grown together; (b, c) a constant, axially applied displacement rate drives the cracks; (d) the test is stopped.

reaches an almost constant plateau stress. The tests were stopped and the samples unloaded when the cracks grew to a sufficient length or out of view of the camera. Tests of thin samples were stopped much earlier than tests of thicker samples, since the supporting brace obscured the tips of the cracks beyond a normalized crack length of 5 (for $w/R=4$).

The effect of varying sample thickness is shown in Figure 5.5. The short crack regime ($l/R<1.5$) is reasonably independent of sample thickness. Differences could be partially attributed to variations in the initial length of the cracks after load cycling. The long crack regime shows a correlation between sample thickness and plateau stress.
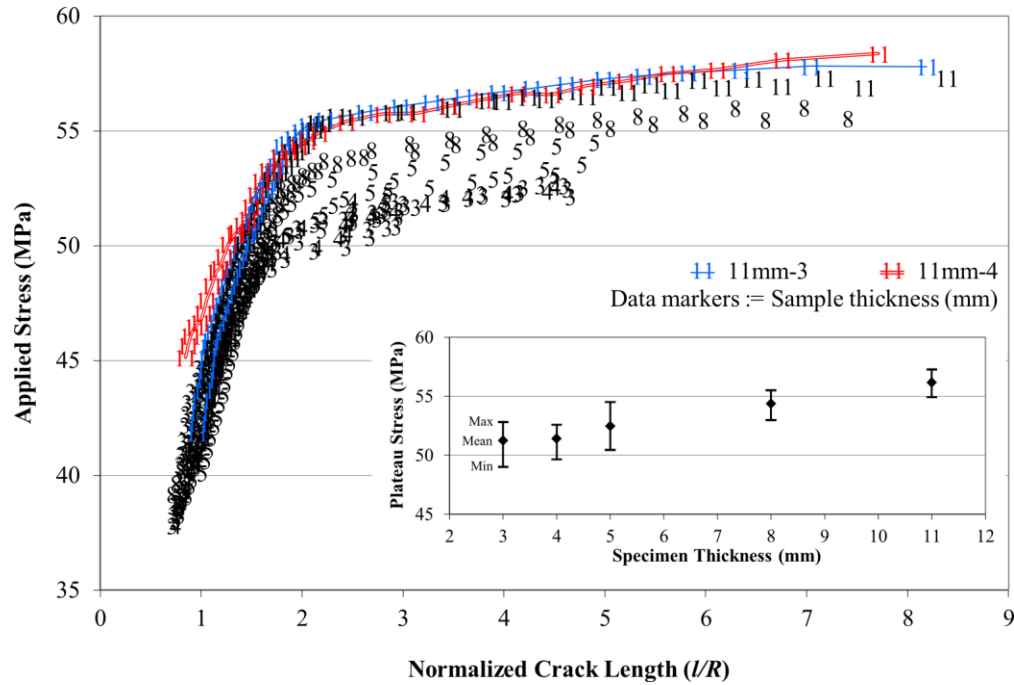
Figure 5.5   DCDC experimental results for all $w/R=4$ samples. Data points are marked by sample thickness. The single-line series, 11mm-3, was tested using 8 mm thick steel inserts between the sample ends and test fixture (Figure 5.6). The double-line series, 11mm-4, had no crack initiation beyond the triangular notches prior to DCDC testing. The insert shows the mean, maximum, and minimum plateau stresses for each tested thickness up to $l/R=5$.

Thicker samples have a higher plateau stress than thinner samples. Increasing sample thickness from 3 mm to 11 mm translates to a ~10 % increase in plateau stress. In other words, it requires 10 % more stress to propagate a long crack along a thick sample than a thin sample. This effect is not attributed to the brace as the unbraced 8 mm thick samples had consistently lower plateau stresses than the 11 mm thick samples.

Several of the thin samples tested in the brace show unexpected jumps in stress in the long crack regime. This was due to the brace becoming too tight, constraining in-plane bending. During initial tests, the brace was loosened when this problem was observed, resulting in the cracks jumping a finite distance. During later tests, the brace

was continuously checked and loosened when needed. Before a sample gets bound up in the brace, its plateau stress appears lower than other samples that never become confined. This effect was observed in the 3, 4, and 5 mm thick sample sets. The out-of-plane compressive stress caused by the brace may enhance crack growth before ultimately the frictional and geometric in-plane constraints take over and restrict growth. We have not studied the effect of out-of-plane compression on crack propagation here.

Two of the 11 mm thick samples were tested under altered conditions (single-line and double-line data in Figure 5.5). One sample, 11mm-3, was tested with 8 mm thick boundary conditions. After load cycling, 8 mm thick steel blocks were centered between the sample and steel plungers such that the front and back edges of the sample were unsupported (Figure 5.6). This arrangement allowed the edges to rotate around the boundary during testing. The results appear similar to previous 11 mm samples, indicating sample thickness at the boundary is not affecting the results. A second 11 mm thick sample, 11mm-4, was directly DCDC tested without prior load cycling. The notches grew together to form full cracks during the course of the DCDC test. The stresses in the short crack regime are initially ~10 % higher than the load cycled 11 mm thick samples, but the two sets overlap once the normalized crack length reaches 1.5.

The w/R=6 samples showed significant inelastic deformation. The first sample, 3mm-5, was tested without load cycling. After unloading, new cracks approximately 1 mm in length formed at the horizontal crowns of the hole, normal to the direction of the applied axial compression (Figure 5.7). Similar tensile cracks due to unloading after inelastic deformation have been observed in void collapse experiments (Nemat-Nasser and Chang 1990). The second w/R=6 sample, 3mm-6, was load cycled in a bath of
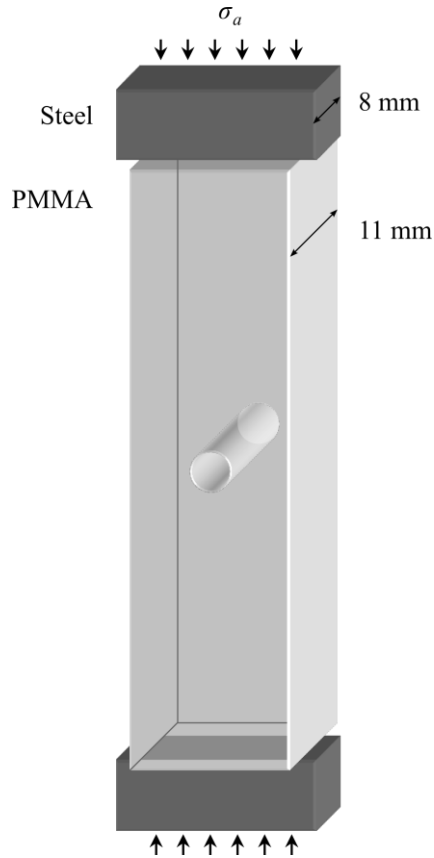
Figure 5.6   DCDC experimental setup for 11mm-3. The 11 mm thick sample was tested using 8 mm steel blocks centered on the top and bottom faces.

liquid nitrogen to prevent inelastic deformation before DCDC testing. After the cracks were initiated, polarized-light photographs were taken to confirm no inelastic deformation had occurred. The DCDC results show the sample load cycled in liquid nitrogen (3mm-6) required less stress than the non-load cycled sample (3mm-5) to propagate the cracks in both the short and long crack regimes (Figure 5.8). Asymmetries in the shape of the 3mm-6 crack tip could indicate the sample was beginning to buckle during DCDC testing despite the presence of the brace (Figure 5.9). The addition of bending out of the sample plane would promote fracture of the DCDC sample.
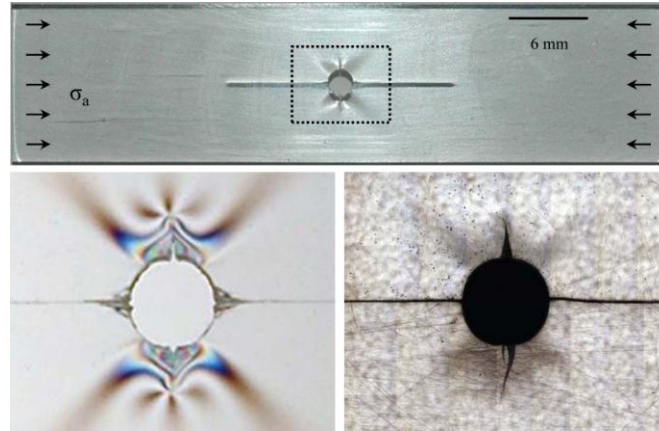
Figure 5.7 *w/R*=6 DCDC sample 3mm-5 after testing. (top) A front view of the entire sample. (bottom left) A close-up image of residual stresses around the hole as viewed using polarized light. (bottom right) A close-up image of the central hole and cracks. The sample has been sanded down to mid-thickness and is viewed using optical microscopy.
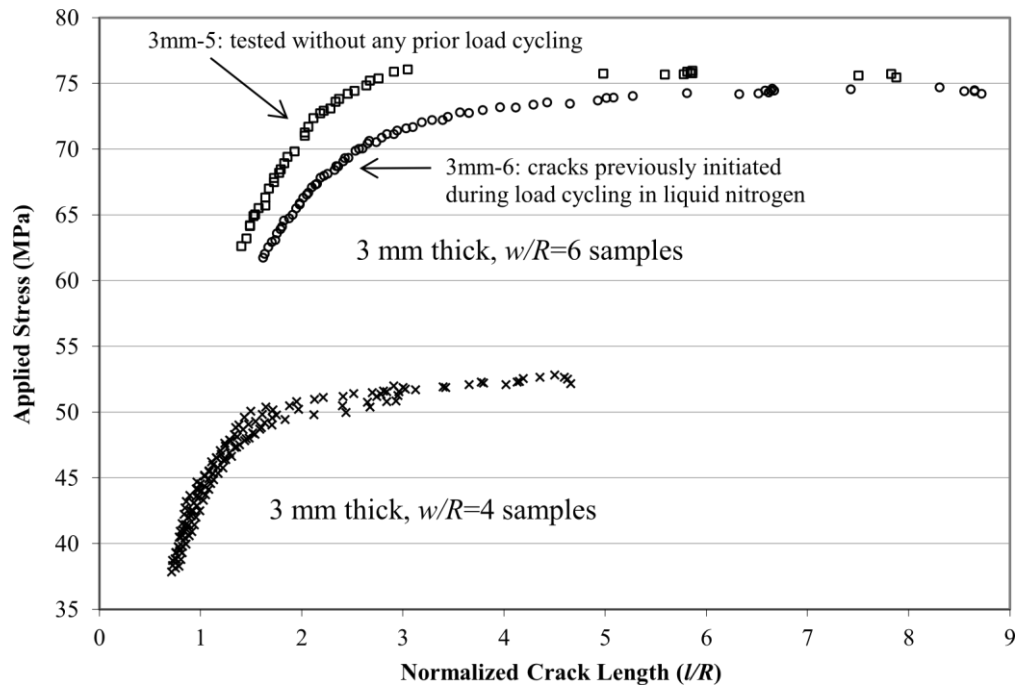
Figure 5.8   DCDC results for all 3 mm thick samples. The *w/R*=6 samples require significantly higher axial stresses than comparable *w/R*=4 samples to propagate cracks.
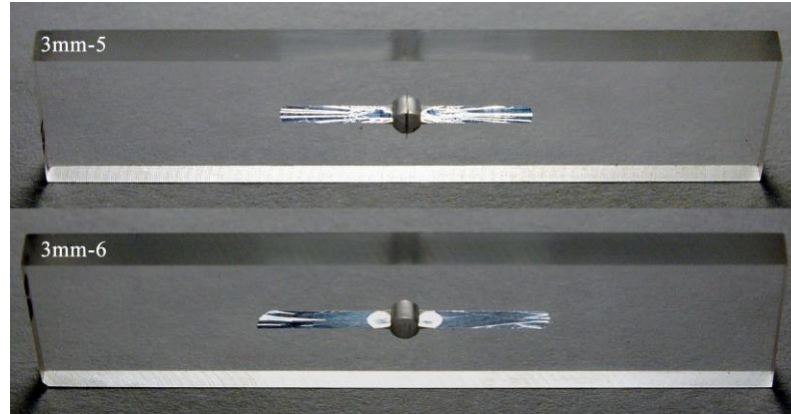
Figure 5.9 w/R=6 DCDC samples after testing. 3mm-5 (top) was tested without prior load cycling, while 3mm-6 (bottom) had been previously load cycled in liquid nitrogen to initiate the cracks (white regions near the hole).

5.4 Morphology of Crack Surfaces

Visual inspection of the fractured w/R=4 DCDC samples reveals three regimes in the crack surface appearance (Figure 5.10). First, closest to the hole, is a region that is either smooth or contains ridges and valleys oriented parallel with the direction of crack growth. The second region has a rougher appearance, with a chaotic collection of pits and peaks that appear as bright speckles in photographs. The third region, farthest from the hole, consists of ridges and valleys radiating outward from the center of the hole. This third region comprises most of the crack surface. Some of the thin w/R=4 samples that were tested in a brace have thumbnail-shaped bands in this region.

Photographs of the samples in the unloaded state were correlated with the crack length versus applied stress data. The photographs were taken with the samples lying flat and the crack plane parallel with the table. The hole was in the center of the image, with the camera angled ~45 degrees above the front face. Each image was scaled such that the hole diameter equaled a normalized crack length (l/R) of 2, as measured by the plot's x-
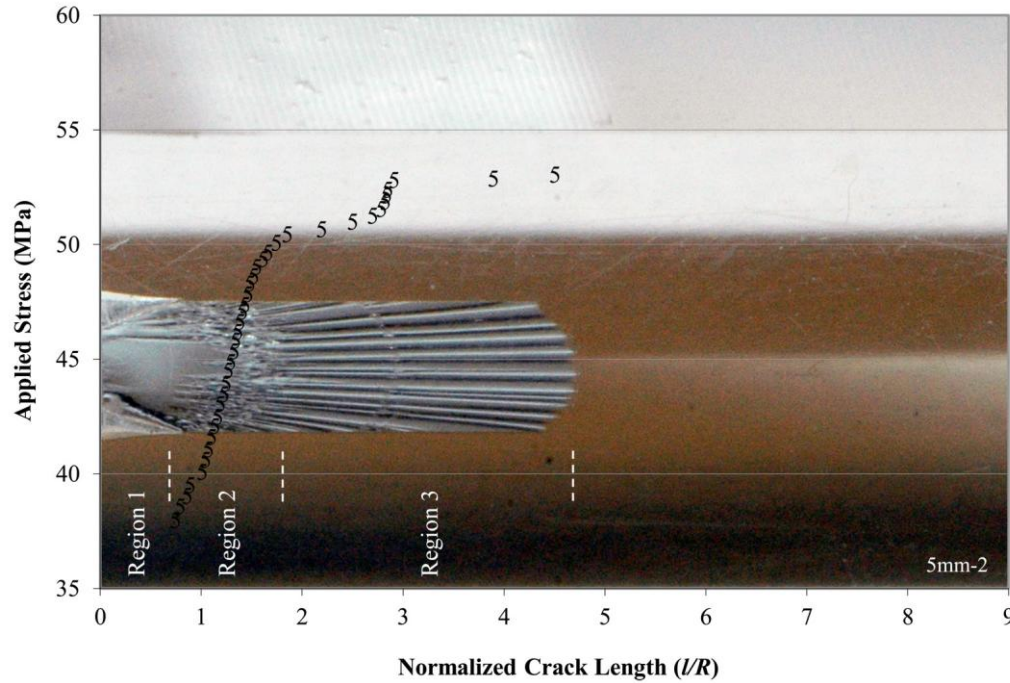
Figure 5.10 DCDC experimental results for w/R=4 sample 5mm-2. The crack surface changes as the sample transitions from short crack to long crack growth. The thumbnail-shaped band in region 3 correlates with the sample being arrested in-plane by the brace.

axis. The images were cropped to the size of the plot area starting from the edge of the hole (beginning of the crack).

Comparing the scaled images with the acquired data (Figures 5.10-14) indicates a correlation between crack surface morphology and axial stress versus crack length DCDC results. As the sample transitions from short crack to long crack behavior, the crack surface transitions from the speckled second region to the smooth ridges and valleys of the third region. All w/R=4 samples exhibited this behavior, including sample 11mm-4, which had not been load cycled. The thumbnail-shaped bands in the long crack regime of several thin samples correlate with the samples being arrested by the brace during testing. This morphology suggests the crack surface features are related to crack tip growth rate
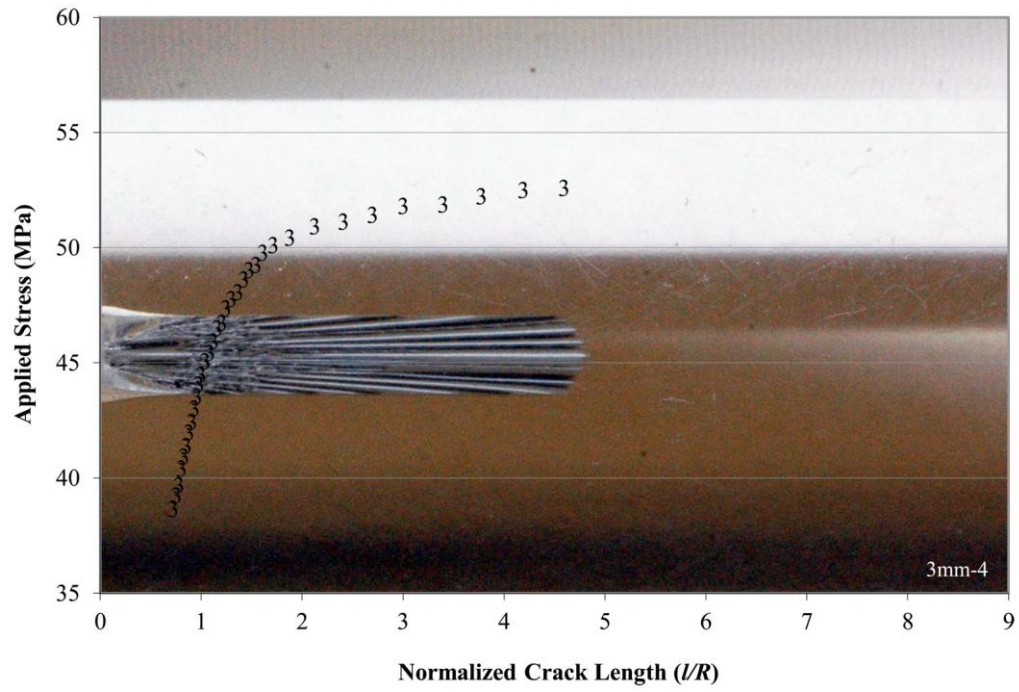
Figure 5.11 DCDC experimental results for w/R=4 sample 3mm-4.
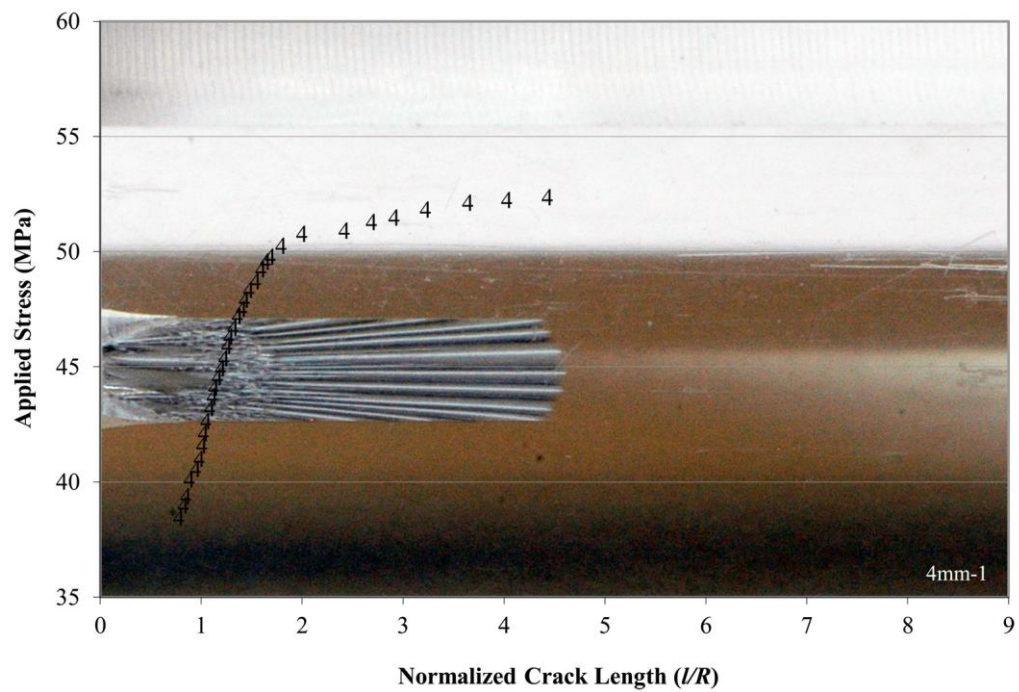
Figure 5.12 DCDC experimental results for w/R=4 sample 4mm-1.
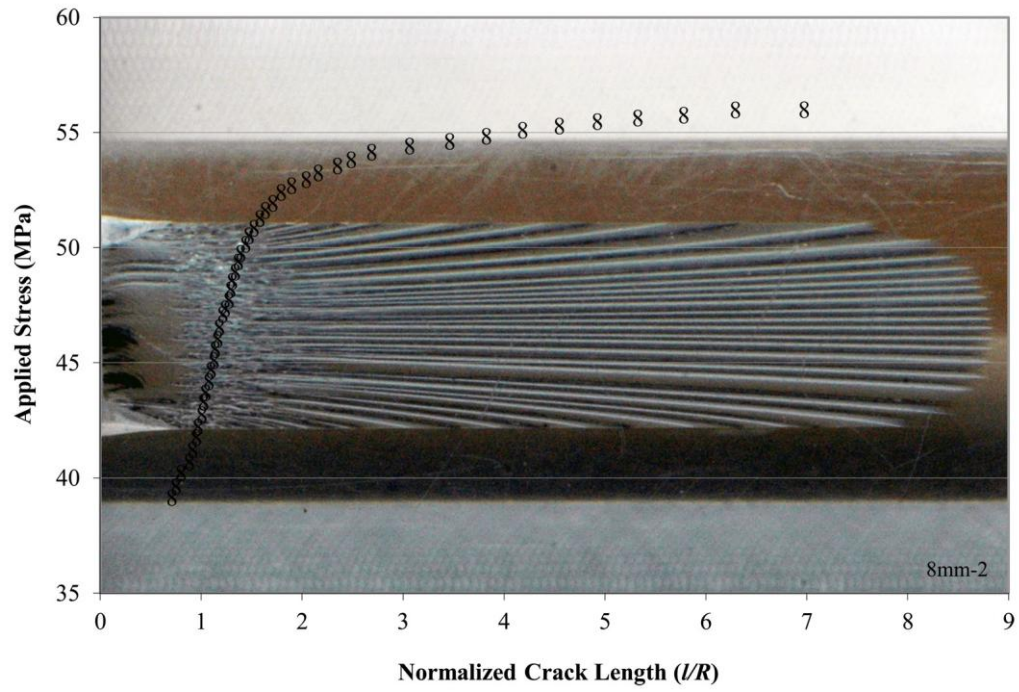
Figure 5.13 DCDC experimental results for w/R=4 sample 8mm-2.
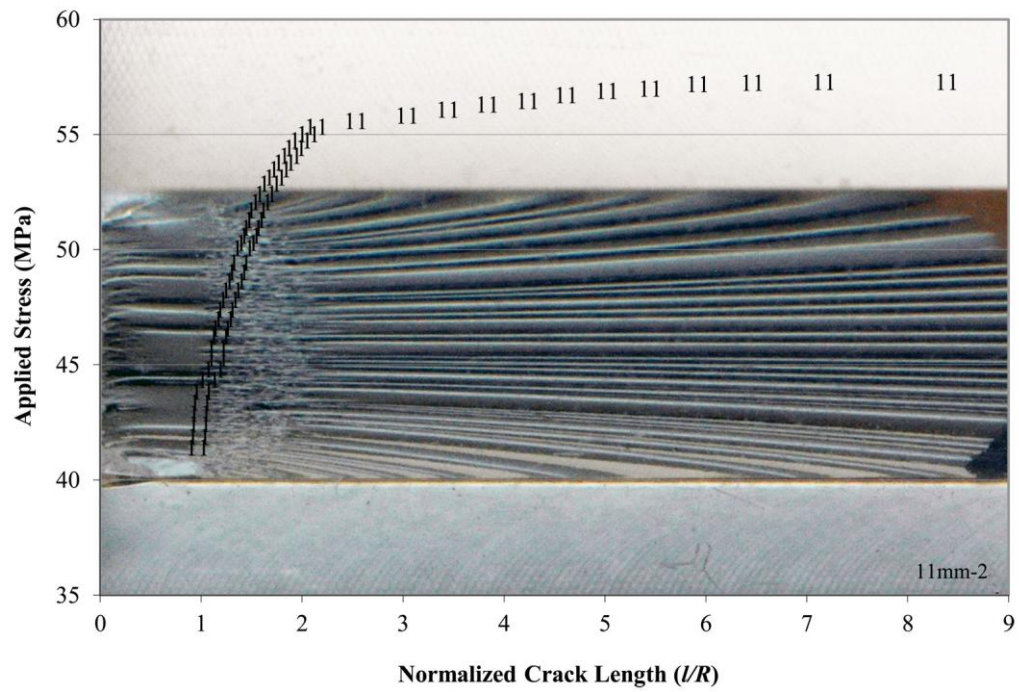
Figure 5.14 DCDC experimental results for w/R=4 sample 11mm-2.

with respect to the applied load. In the short crack regime the crack advances slowly as the axial load is increased, while the long crack regime sees much faster crack growth, unless an over-tightened brace interferes.

The w/R=6 sample 3mm-5, which was not load cycled, contained similar crack surface regions to the w/R=4 samples (Figure 5.9). Since the sample underwent significant inelastic deformation, the pictures could not be scaled and compared with the data as was done with the w/R=4 samples. The second w/R=6 sample, 3mm-6, contained cracks with a bright region corresponding to growth during load cycling in liquid nitrogen and a mostly smooth and clear area corresponding to growth during the DCDC test.

The crack surfaces of a 5 mm thick sample were examined using optical microscopy. After DCDC testing, the sample was split axially, exposing the crack surfaces. The short crack regime where bright speckles appear in macroscopic photographs has numerous shark tooth-shaped structures pointing in the direction of crack growth (Figure 5.15) and consistent with the formation of crazes (Pulos and Knauss 1998). These structures were examined more closely using a scanning electron microscope. Small strands of material protrude from some of the structures. Sample 3mm-6, which did not have the same macro-appearance as the rest of the samples, was also microscopically examined (Figure 5.16). The region of the crack grown during load cycling in liquid nitrogen has a chaotic pattern creating the highly reflective surfaces seen in photographs.
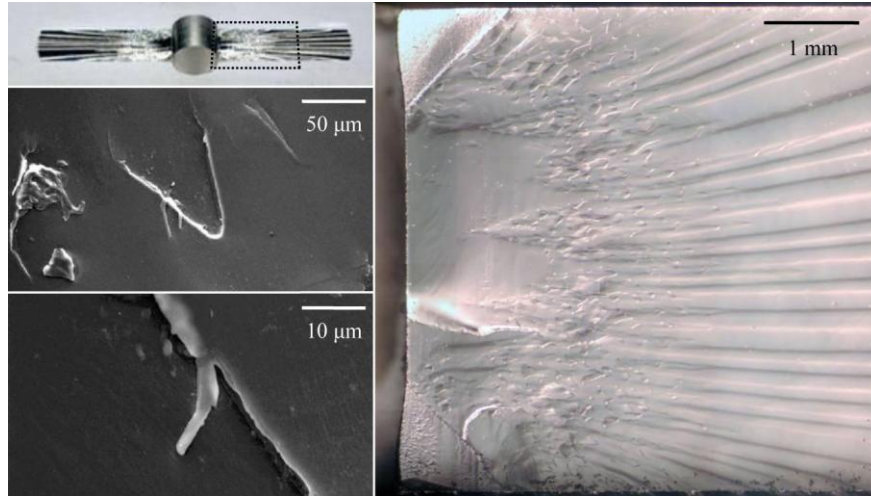
Figure 5.15 Microscopy images of the fracture surface of a 5 mm thick sample. The highlighted area of the crack surface (top left) was viewed using optical microscopy (right). The triangular notches are visible on the top and bottom of the crack surface next to the through-thickness hole. The crack grew from left to right. Small, shark tooth-shaped structures on the crack surface are the cause of the bright speckles in macroscopic photographs. (middle left) SEM view of a tooth-shaped structure, and a craze (bottom left).
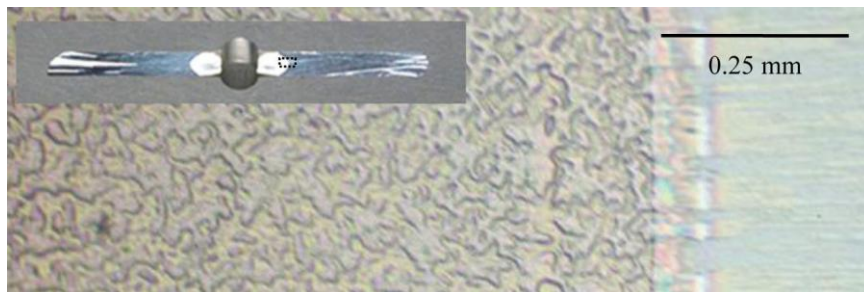
Figure 5.16 Optical microscope image of the 3mm-6 crack surface. The crack grew from left to right. The chaotic pattern covers the region where cracking occurred in liquid nitrogen. The relatively smooth region is where the crack was grown during DCDC testing at room temperature.

5.5   Finite Element Modeling

Models have previously been developed to estimate fracture toughness using DCDC experimental data. He et al. (1995) use a finite element approach and plane-strain linear elasticity, but do not consider nonlinear geometric effects that occur when the cracks are long. The result is a linear relationship between axial stress and crack length that does not capture the plateau regime of crack growth observed in the present work. Pallares et al. (2009) combine linear elastic finite element simulations and experimentally measured crack opening displacements to estimate crack shapes and stress intensity factors as a function of geometry and loading. Plaisted et al. (2006) consider beam bending in their theoretical model for estimating critical stress intensity factors for the DCDC test.

Here, an approach is developed that uses experimental results to estimate stored internal energy, energy release rate, and critical stress intensity. The approach relies on finite element (FE) calculation for a sequence of crack lengths and includes nonlinear geometric effects. In each simulation, one quarter of a DCDC sample is used with boundary conditions accounting for the missing sections (Figure 5.17). Crack length is prescribed through the use of traction-free boundary conditions along the crack surface. Each model consists of 1690 shell elements with1799 nodes. Refining the mesh size by a factor of four did not lead to a significant change in simulation results. The mesh was not concentrated at the crack tip, since we are interested in the total stored elastic energy for each crack length.   While the geometric nonlinearities are included, the constitutive relation for PMMA is approximated by a linearly elastic isotropic model.   Young's modulus E=3100 MPa was determined by uniaxial compression experiments. Poisson's
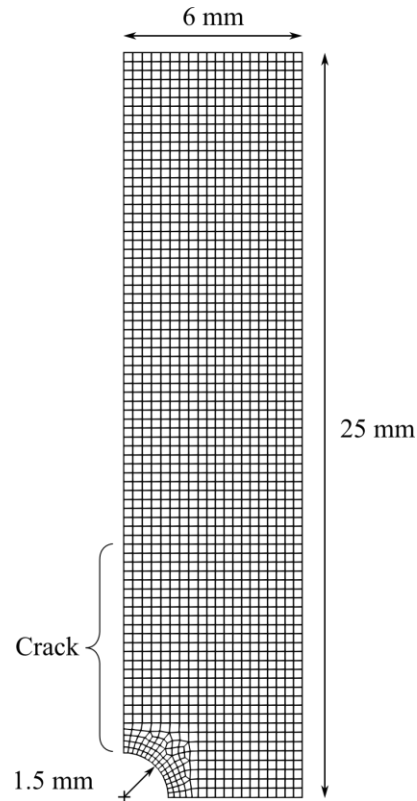
Figure 5.17 Finite element model of the DCDC geometry.

ratio v=0.40 was assumed. Varying the Poisson's ratio from 0.3 to 0.4, values typical for PMMA (Maccagno and Knott 1989), was found to have a minimal effect on the results. Since the w/R=6 samples clearly deformed inelastically, the simulations focused on the w/R=4 geometry. Both plane stress and plane strain cases are considered. The simulations are performed using the LS-DYNA implicit solver.

For each crack length, a complete simulation begins with a series of small displacement steps applied to the top nodes. The total force required at each displacement step is determined and compared with experimental data for the associated crack length. Once the axial load of the model has been correlated with experiment, the internal energy is recorded and compared with the internal energy at the same

displacement in the next FE simulation where the crack is one element longer. In this manner the computer script "grows" the crack by one element length, Δl ($\Delta l/R \approx 0.2$ for the studied element sizes), while holding the displacement constant. Comparing the internal energy, U, before and after crack growth yields the strain energy release rate:

$$G = -2\frac{\Delta U}{\Delta l}.$$ (5.1)

The change in internal energy must be multiplied by two because the finite element model includes only one side of the complete crack. The critical stress intensity factor is then:

$$K_{Ic} = \sqrt{GE'}$$ (5.2)

$$E' = E \qquad \text{for plane stress, and}$$

$$E' = \frac{E}{1-v^2} \qquad \text{for plane strain.}$$

The simulations estimate the K_{Ic} of PMMA to range from 0.6 to 0.75 MPa·m$^{\frac{1}{2}}$ (Figure 5.18). These critical stress intensities are on the low end of the range given in literature for a variety of fracture experiments (Marshall and Williams 1973). Using a long crack approximation for the DCDC experiment, Plaisted et al. (2006) estimates the K_{Ic} of PMMA to be 0.71 MPa·m$^{\frac{1}{2}}$, which falls within the range estimated here.
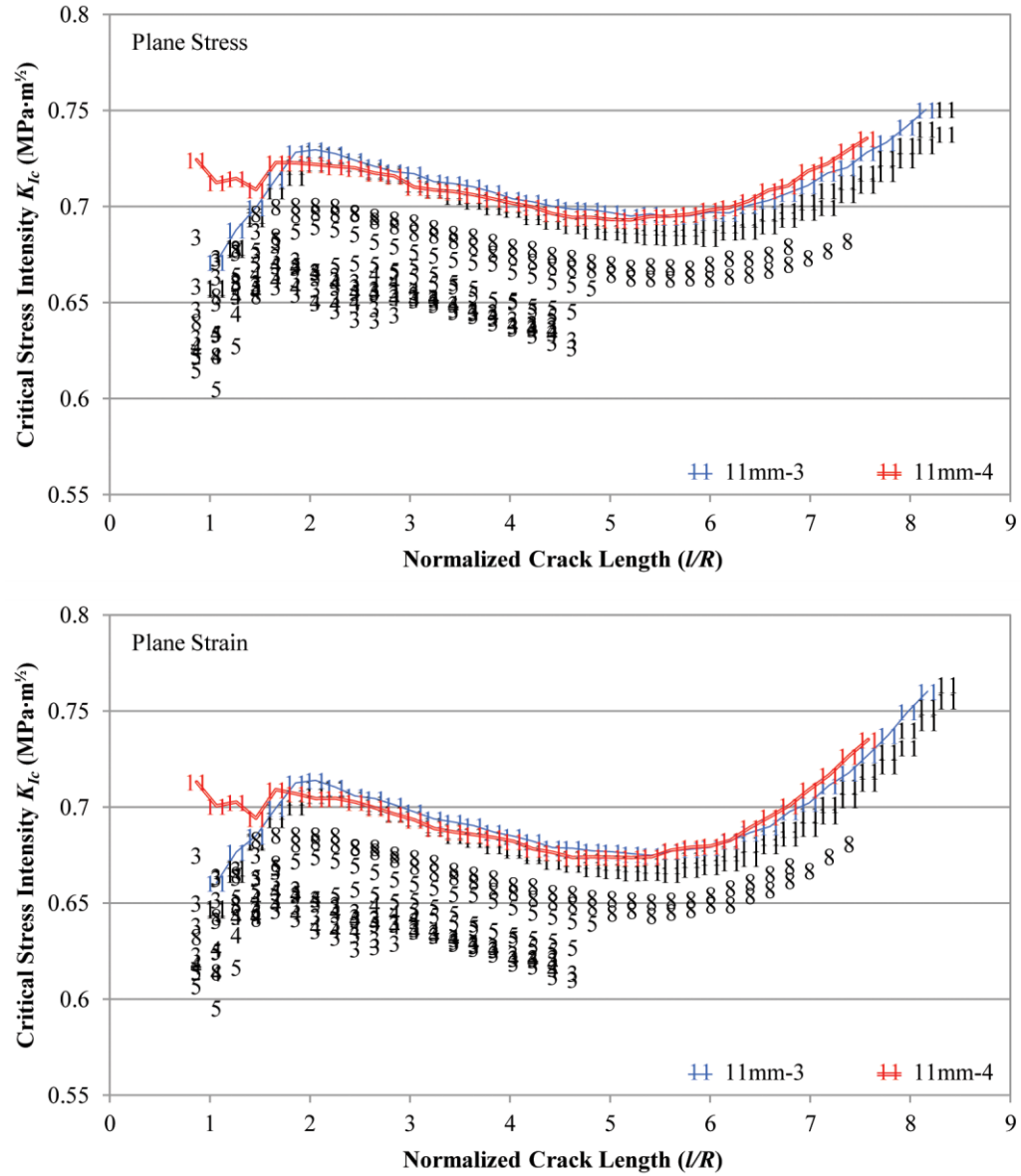
Figure 5.18 Finite element simulation results of the DCDC test using two dimensional plane stress (top) and plane strain (bottom) shell elements.

Examining individual simulation results, the thickest samples (11 mm) have a ~10 % higher K_{Ic} than the thinnest samples (3 mm), which is consistent with plateau stress observations. The critical stress intensity factors estimated using plane stress analysis are generally ~1-3 % higher than those calculated using plane strain analysis. The total variation in the estimated K_{Ic} as the cracks grow is relatively small (±10 % maximum), but follows a distinct pattern. During short crack growth ($l/R<2$), K_{Ic} for the load-cycled samples generally increases with crack length, particularly in the thicker, load-cycled samples. Since the non-load-cycled sample maintains a relatively constant K_{Ic} in this regime, the increase suggests some damage has accumulated ahead of the crack tips during initiation. Damage would facilitate the initial crack growth during the DCDC test. Once the cracks become long ($l/R>2$), the estimated K_{Ic} decreases with crack length, indicating the cracks are becoming easier to drive. The sides of the DCDC sample are now starting to bend outward, away from the crack plane, and viscoelastic effects coupled with this change in geometry could increase the energy available to drive the cracks and therefore the material appears to lose toughness. Once the cracks become very long ($l/R>5.5$-6), however, the sides of the DCDC sample have bent outward so significantly that the sample deforms permanently (Figure 5.20). Each marginal increase in crack length now requires additional energy for plastic work. Since the simulation uses a linear elastic material model, it can only interpret the crack growth in this regime as the sample appears tougher.

5.6   Photoelastic Verification

A DCDC experiment was conducted using polarizing light filters to observe the photoelastic effect.   The photoelastic fringes are compared with the stress fringes determined by finite element simulation.

The DCDC experimental setup previously described was modified slightly to accommodate additional equipment.   A lamp with a polarized filter was positioned behind the sample. A second cross-polarized filter was attached to the camera lens. The flash was covered so the only light captured by the camera passed through both polarizing filters.   The sample was oriented to face the camera.   A first-surface mirror was positioned next to the sample so the camera could observe the crack.   This setup ensured that each photograph would capture a front view and an angled view of the sample. A new DCDC sample was machined out of Acrylite GP PMMA. It measured 50 mm tall, 16 mm wide, and 8 mm thick with a 4 mm diameter central hole for a w/R ratio of 4. It was prepared for testing in the same manner as discussed previously, including load cycling to initiate the cracks.

A qualitative comparison of the photoelastic pictures taken during DCDC testing and the results of the finite element simulation indicates reasonably good agreement (Figure 5.19). The distribution of Von Mises stresses within the finite element models has a pattern analogous to the photoelastic fringes observed.   Around the hole, a butterfly-shaped experimental stress distribution is estimated to have a 52 degree angle from the horizontal midline.   The simulation produced a similar shape with an angle estimated to be 57 degrees.

Figure 5.19 Experimental photoelastic results (converted to grayscale) compared with finite element simulation results. (Left) The DCDC cracks are visible in the angled view created by the mirror. (Center) Frontal view of the DCDC sample under polarized light. (Right) Von Mises stress determined by finite element analysis. The stress concentration around the hole makes an angle of 52 degrees in the experiment and 57 degrees in the FEM simulation. Note: the grayscale fringe levels only apply to the finite element results.

The sample was also photographed using polarized light before and after DCDC preparation and testing (Figure 5.20). Prior to any loading, the sample shows two small areas of inelastic deformation at the apex and base of the central hole. This is where the razor was pushed into the sample to create the notches. Immediately after load cycling, residual stresses are apparent, but they dissipate within a few minutes. After DCDC testing, significant residual stresses remain, particularly around the hole, 90 degrees from the direction of loading. The inelastic deformation that led to these residual stresses is
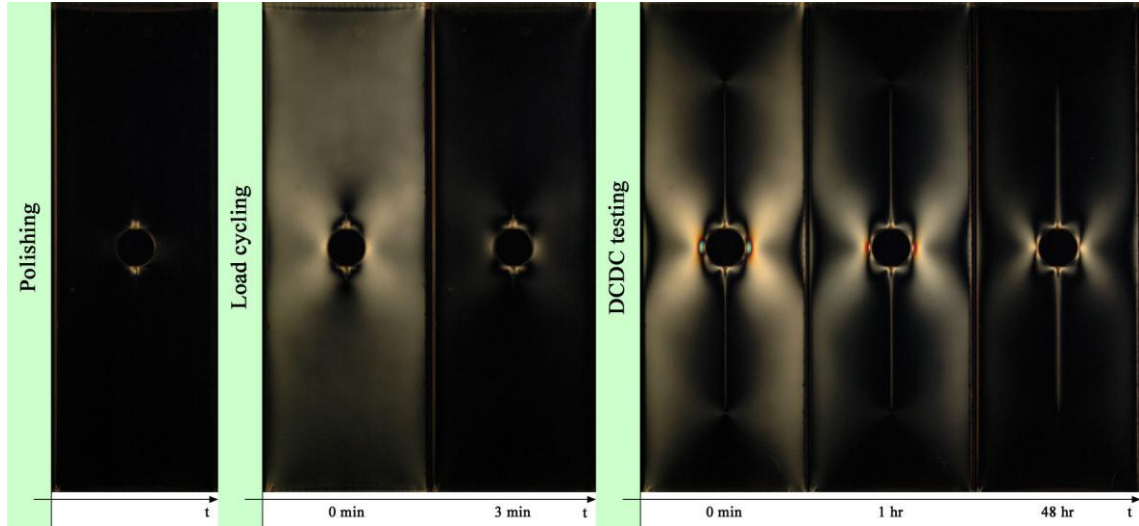
Figure 5.20 The photoelastic DCDC sample at different stages during testing: after polishing, after load cycling, and after DCDC testing.

likely the cause of the discrepancy between the angles associated with the experimental and simulated stress distributions. The non-linear material effects in the experiment were not captured by the simulation, which assumes perfectly elastic behavior.

5.7 Discussion

Even though our analysis is presented both using plane stress and plane strain conditions, the plane stress case may be more appropriate for our experiments. Plane strain conditions enforce an unrealistic global stress state, i.e. very large stress component through thickness (out-of-plane component). However, the arched shape of the crack tip is developed due to the locally different stress states between the free surface and the center; the height of the arch in the long crack regime was 1.2 mm in an 11 mm thick sample, and only 0.2 mm in a 3 mm thick, $w/R=4$ sample. As expected (Fernando and Williams 1980; Dowling 1999) given the less constrained conditions for plastic

deformation on the free surfaces, the crack growth is slower than inside the sample. This effect can also be interpreted as a higher toughness at the free surfaces. In the thinner samples, the stress condition is more uniform through the thickness and therefore one observes a less pronounced arch.

Each crack grows due to the tensile stress state ahead of the crack tip. This can be related to the applied axial load and may be influenced by the way in which the end loads are applied. In general, the crack length is correlated with the applied axial stress. Furthermore, the stress required to extend the crack has to be increased by a small amount for thicker samples (~10 % increase for 3 mm and 11 mm thick samples). The distinction between thicker (e.g. 11 mm thick) samples and the thinner ones (e.g. 3 mm thick) may be attributed to the more constrained global deformation of the sample. To evaluate this hypothesis, we simulated 3D FE models of typical thick and thin (11 mm vs. 3 mm) $w/R=4$ quarter geometries with the same crack length: $l/R\approx4$. In both cases the sample was expected to be in the plateau regime of crack growth. The axial load was adjusted such that the opening stress component, averaged along the crack tip line would be equal. The value of axial applied stress was then compared. It was found that the 11 mm model requires 3.9 % higher axial stress compared to the 3 mm model, to produce the same average opening stress. Note the experimentally observed difference between the plateau stresses in these two extreme thicknesses is ~10 %; however this entire effect is simply ignored in a 2D analysis. We must further note a few observations and limitations about the analysis just mentioned. First and foremost, the analysis clearly gives us an average state of stress, essentially masking the singular fields. Second, in our 3D FE models we assumed a straight crack tip. Third, even though the average opening

stresses are made equal, the maximum opening stress (in both cases located at the center of the crack tip line) is different. In fact the maximum is about 11 % higher in the 11 mm model. However, it decreases more sharply towards the free surfaces in the 11 mm model, while it is relatively flat in the 3 mm model. Finally, we observed a substantial difference in the other stress component: the out-of-plane stress. In a 2D plane stress analysis, this component of the stress tensor is assumed zero, while in plane strain analysis, it is predominantly compressive. However, in both 3D analyses (11 mm and 3 mm), the out-of-plane stress is observed to be tensile and of the same order of magnitude as the opening stress. Furthermore, on average and at the maximum point (center of the crack line) it is about 60 % higher in the 11 mm model compared to the 3 mm model. This difference could clearly contribute to the crack growth and suggests the 2D simulations are more accurate for the relatively thin samples. However, the effect of the three-dimensional state of stress around the crack tip will require further detailed study.

5.8   Conclusions

Decreasing DCDC sample thickness to reduce the volume of material was found to decrease not only the force but actually the axial stress necessary to propagate long cracks. Using a brace that could frictionally constrain the in-plane motion of the reduced-thickness samples to prevent their out-of-plane buckling is not recommended, as it clearly influenced the results of several tests. However, using other buckling-prevention mechanisms that eliminate or minimize friction may be a viable alternative when material quantities are limited. Furthermore, a 2D geometrical analysis is more applicable to a thinner shape as discussed earlier. Reducing the DCDC hole size by one

third led to significant inelastic deformation, with one sample forming new, stress-relieving cracks upon unloading. The morphology of the crack surfaces was correlated with the regimes of crack growth data. The short cracks and long cracks have distinct surface features that are believed to be associated with the velocity of the crack tip. A series of finite element calculations was developed to estimate critical stress intensity factors based on the experimental data. The calculations include the nonlinear geometric effects, but use a linearly elastic constitutive relation. A qualitative comparison of experimental and simulated stress distributions showed reasonably good agreement, the limitations of 2D stress analysis notwithstanding.

Chapter 6

The DCDC Fracture Test: Simulations and Empirical Modeling

The computational model developed in Chapter 5 (Nielsen et al. 2012) was adapted to study a wider range of DCDC sample geometries, material properties, and boundary conditions.

6.1   Introduction

Axial compression is used to drive tensile cracks in a double cleavage drilled compression (DCDC) sample. This interesting fracture behavior is the result of a geometric effect created by a hole in a rectangular column of material. A detailed description of the sample geometry and a displacement controlled experimental setup are given in Chapter 5. The DCDC method leads to highly oriented crack growth with long periods of stability. The traditional compact tension or single-edge notched bending tests create unstable crack growth and lead to separation of the sample. For crack healing studies, this is problematic as the two faces must be carefully realigned. The advantage of these tests over the DCDC geometry is the critical stress intensity factor, K_{Ic}, can be easily and reliably calculated from the experimental measurements (Tada et al. 2000).

Fracture toughness models have been developed for the DCDC test. Perhaps the most popular model was developed by He et al. (1995) using finite element methods to evaluate geometry effects. A simple linear model was fitted to the simulated results:

$$\frac{\sigma_a \sqrt{\pi R}}{K_{Ic}} = \frac{w}{R} + \left(0.235\frac{w}{R} - 0.259\right)\frac{l}{R}, \tag{6.1}$$

where σ_a is the axial stress and the geometric parameters, w, R, and l, are given in Figure 6.1. The effect of material properties was not considered. For typical geometries, the model predicts relatively large increases in axial stress with changes in crack length.

The linear behavior predicted by equation (6.1) does not agree with the DCDC experimental observations made Plaisted et al. (2006). After an initial period of increasing axial stress with increasing crack length, the stress plateaued and the cracks grew at an almost constant stress level. A theory-based model was developed to estimate K_{Ic} from the experimental results. Conceptually, the DCDC test is subdivided into short crack and long crack growth regimes. In the short crack regime, the sample is treated as a plate with cracks near the central hole. Once the cracks are sufficiently long, the long crack regime treats the DCDC sample as four beam-columns subjected to bending due to a moment created by the hole and axial compression. As the cracks grow, the lengths of the beams increase. In the linear case, the moment is assumed to be independent of crack length, allowing the critical stress intensity factor to be estimated as:

$$K_{Ic} = \frac{2\sigma_a R}{\sqrt{w}} g\left(\frac{w}{R}\right), \tag{6.2}$$

where $g(w/R)$ is a non-dimensional function relating to the bending moment. The model predicts crack growth in the long crack regime requires a constant stress, an assumption that fits the experimental results. Other experimental results, such as those obtained by Michalske et al. (1993), did not exhibit a similar plateau stress. Adding nonlinear geometric effects is discussed by Plaisted et al. (2006), but this would lead to unstable crack growth in their model as the stress intensity factor becomes an increasing

function of crack length. A better estimate of the moment, particularly as a function of crack length, could improve the long crack model.

In Chapter 5.5, a finite element simulation scheme was established to study the DCDC test. The method was originally developed to study the evolution of the bending moment during the test, but it was determined that K_{Ic} could be directly estimated from the output. One quarter of the DCDC geometry was simulated, and the change in internal energy was calculated as the crack was progressively lengthened. The simulation data were correlated with the experimental results to estimate K_{Ic} as a function of crack length. But this method is time consuming; a simple, single-value estimate of K_{Ic} would be useful.

In the present chapter, a series of finite element simulations are performed where the DCDC sample hole size, width, length, Young's modulus, Poisson's ratio, critical stress intensity factor, and boundary conditions are alternately varied from the experimental conditions in Chapter 5. The results are used to develop a simple estimate of K_{Ic} as a function of hole size, sample width, and a fictitious applied stress at zero crack length estimated from a linear fit of long crack data. The model is shown to provide reasonably good estimates of K_{Ic} over all simulated geometries and materials, as well as all considered experiments.

6.2   Simulation

The 2D finite element simulation approach previously discussed was modified to investigate the effect of sample geometry and material properties on the DCDC fracture test. The new method uses a prescribed critical stress intensity factor to estimate the

applied stress as a function of crack length, essentially reversing the order of the original calculation. As a result of this change, no experimental data is required as an input for analysis.

One-quarter of the DCDC geometry is modeled (Figure 6.1), and the test is simulated for a given crack length, l, using two-dimensional, plane stress, shell elements and a linear elastic, isotropic material model. At each displacement step, the crack is virtually grown by one element, and the change in internal energy, energy release rate, and critical stress intensity factor, K_{Ic}, are calculated. When the simulation K_{Ic} matches the prescribed K_{Ic}, the applied force (stress) at that displacement is associated with the
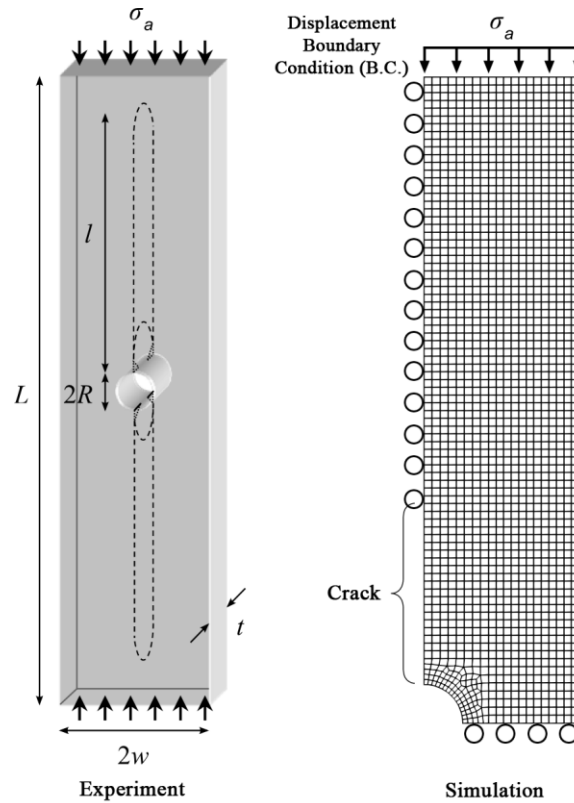
Figure 6.1   The DCDC sample geometry for fracture experiments and simulations.

crack length l. Repeating this procedure at successive crack lengths yields a curve of applied stress versus crack length. The approach was applied to experiments on fused silica by Michalske et al. (1993). The sample geometry and material properties given in the paper were used in the simulation. The critical stress intensity factor of 0.740 MPa·m$^{\frac{1}{2}}$ had previously been determined by double cantilever beam (DCB) fracture experiments (Weiderhorn et al. 1974). The results of the simulation give stress versus crack length results that closely match the experimentally observed behavior (Figure 6.2a).

The simulation method was applied to the experimental geometry and material properties in Chapter 5. Similar to experimental observations, an initial region of increasing stress is followed by a plateau region with smaller changes in the fracture stress. This curve has a positive slope when the crack growth is stable. Regions of instability where continued crack growth requires less applied force (a negative slope) were observed. This instability may be due to nonlinear geometric effects associated with lateral displacement and bending. Sammis and Ashby (1986) predict an eventual decrease in axial stress due to elastic buckling in a uniaxially compressed finite plate containing a central hole. Amirkhizi (2012) has mathematically shown that periods of unstable crack growth are possible for purely displacement controlled fracture conditions. It's important to note that the simulation is designed to give non-physical results when the crack growth becomes unstable. Rather than having the crack grow rapidly at a relatively constant stress due to the instability, the simulation calculates fracture stresses that decrease. The simulation does not consider the previous length of the crack, only its current and future length. The method is easily modified to account for the previous

crack length and give only physical results, but this change was not made in order to better observe regions of instability.

The sample length, width, hole size, critical stress intensity factor, Young's modulus, Poisson's ratio, and displacement boundary condition were alternately varied from the experimental conditions in Chapter 5. Table 6.1 summarizes the evaluated geometries, material properties, and boundary conditions. Figure 6.2a-h gives the applied stress versus normalized crack length simulation results.

Table 6.1 The simulated DCDC geometries, materials properties, boundary conditions, and linear fits of the long crack regimes. A single fit was used for simulation results that appeared to have to similar linear regions.

Geometry			Material			B.C.	$\sigma_a = m\left(l/R\right) + \sigma_0$	
w/R	w (mm)	L (mm)	E (GPa)	K_{Ic} (MPa·m^{½})	ν		m	σ_0 (MPa)
3.75	3.75	75	73	0.740	0.17	Frictional	5.7273	58.366
4	6	50	3.1	0.7	0.4	Frictional	1.4215	50.490
2	6	50	3.1	0.7	0.4	Frictional	0.8289	14.028
3	6	50	3.1	0.7	0.4	Frictional	1.3344	29.582
5	6	50	3.1	0.7	0.4	Frictional	1.1400	76.475
4	4	50	3.1	0.7	0.4	Frictional	1.4787	60.892
4	8	50	3.1	0.7	0.4	Frictional	0.0055	45.644
4	6	30	3.1	0.7	0.4	Frictional	0.3995	47.311
4	6	100	3.1	0.7	0.4	Frictional	1.4215	50.490
4	6	50	1	0.7	0.4	Frictional	-1.4727	48.481
4	6	50	10	0.7	0.4	Frictional	3.3126	50.342
4	6	50	73	0.7	0.4	Frictional	4.3675	49.976
4	6	50	3.1	0.4	0.4	Frictional	1.4244	28.948
4	6	50	3.1	1.0	0.4	Frictional	0.9059	71.561
4	6	50	3.1	0.7	0.3	Frictional	1.4215	50.490
4	6	50	3.1	0.7	0.495	Frictional	1.4215	50.490
4	6	50	3.1	0.7	0.4	Friction-free	1.4215	50.490
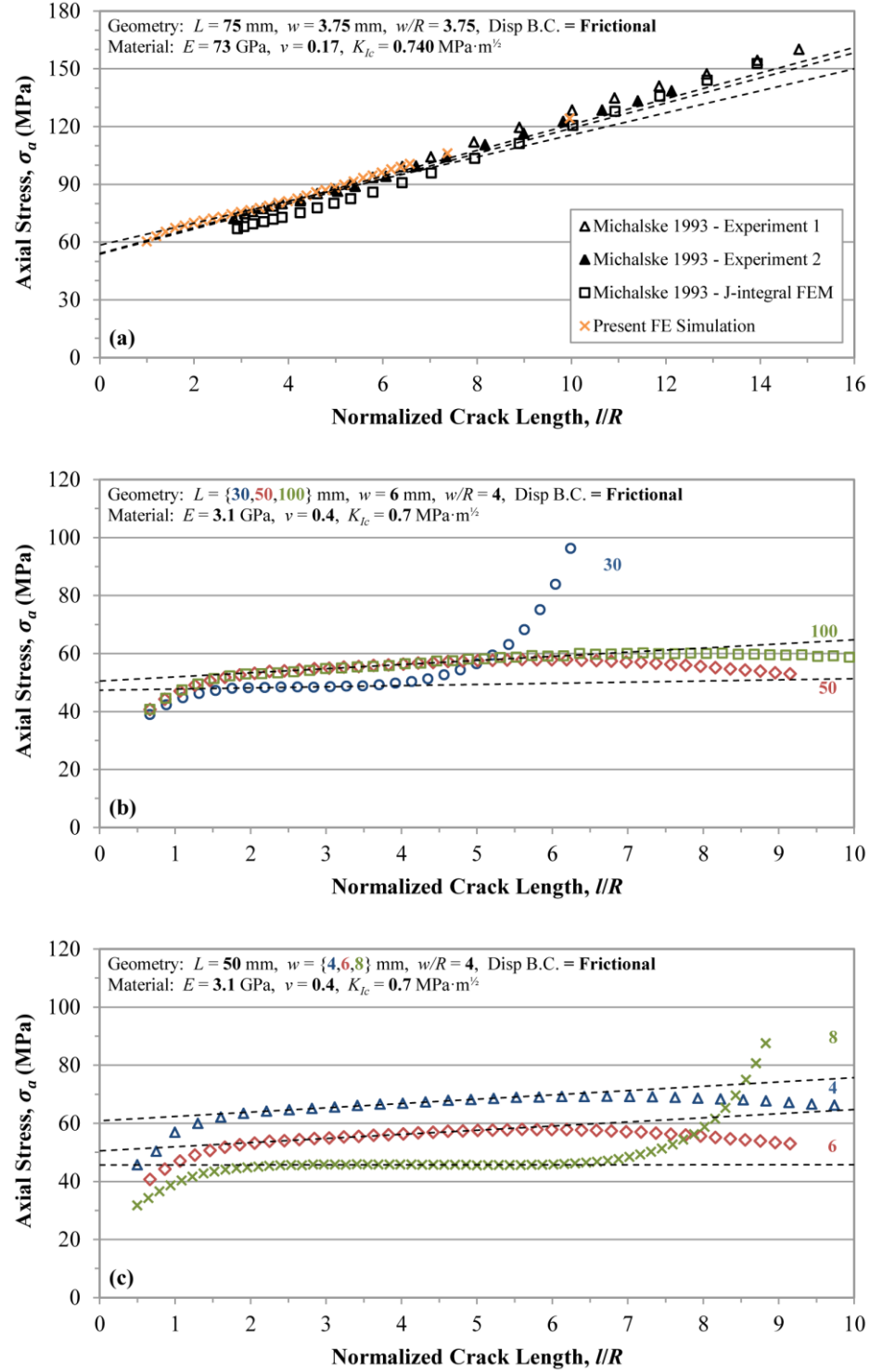
Figure 6.2 (a) DCDC experimental and computational results from Michalske et al. (1993) as well as simulation results for the same geometry, material, and boundary condition. Simulation results are presented for the experimental conditions in Chapter 5, with the sample length (b) and width (c) varied.
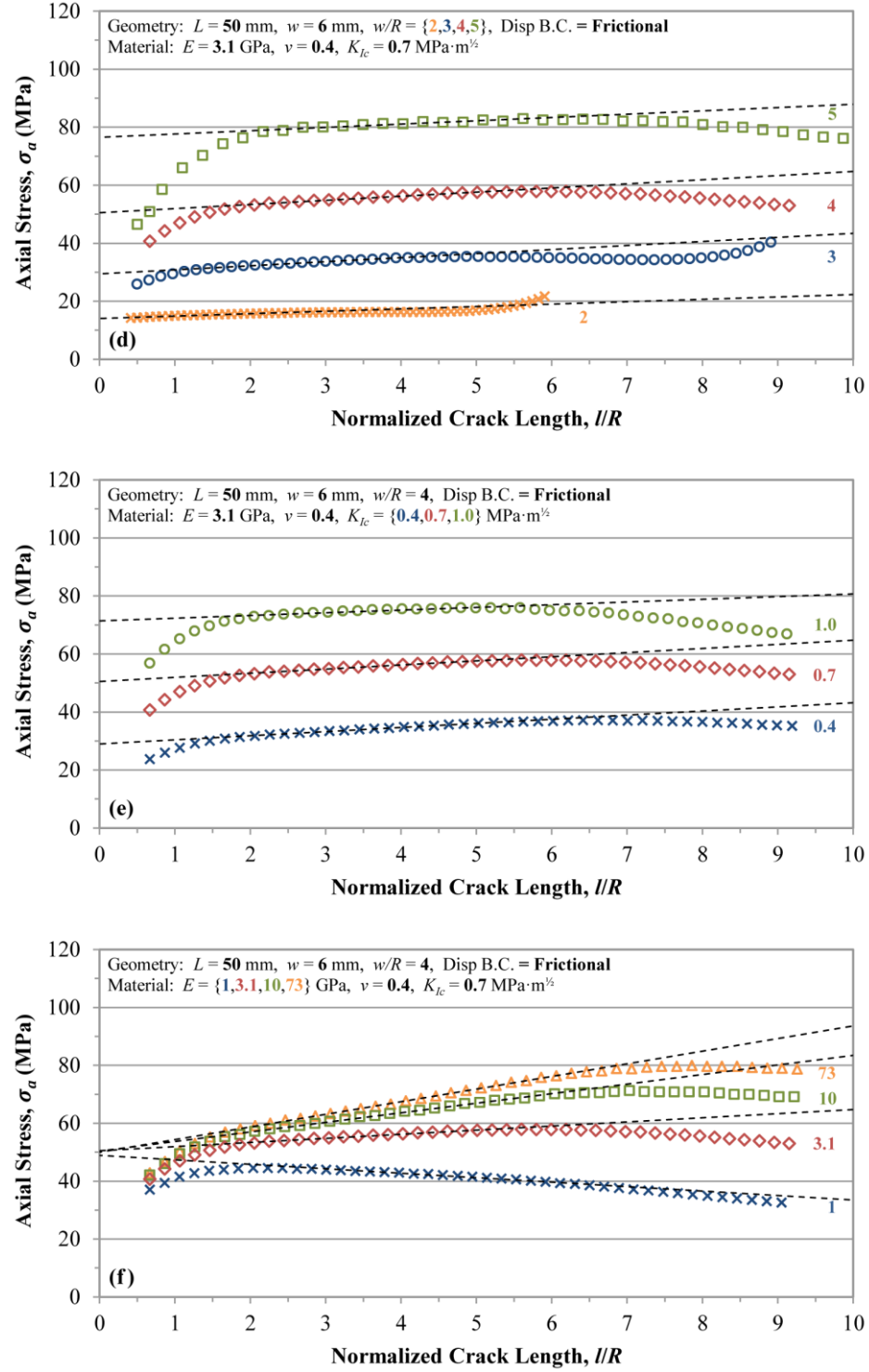
Figure 6.2 Simulation results continued for the experimental conditions in Chapter 5, with the sample hole size (d), critical stress intensity factor (e), and Young's modulus (f) varied.
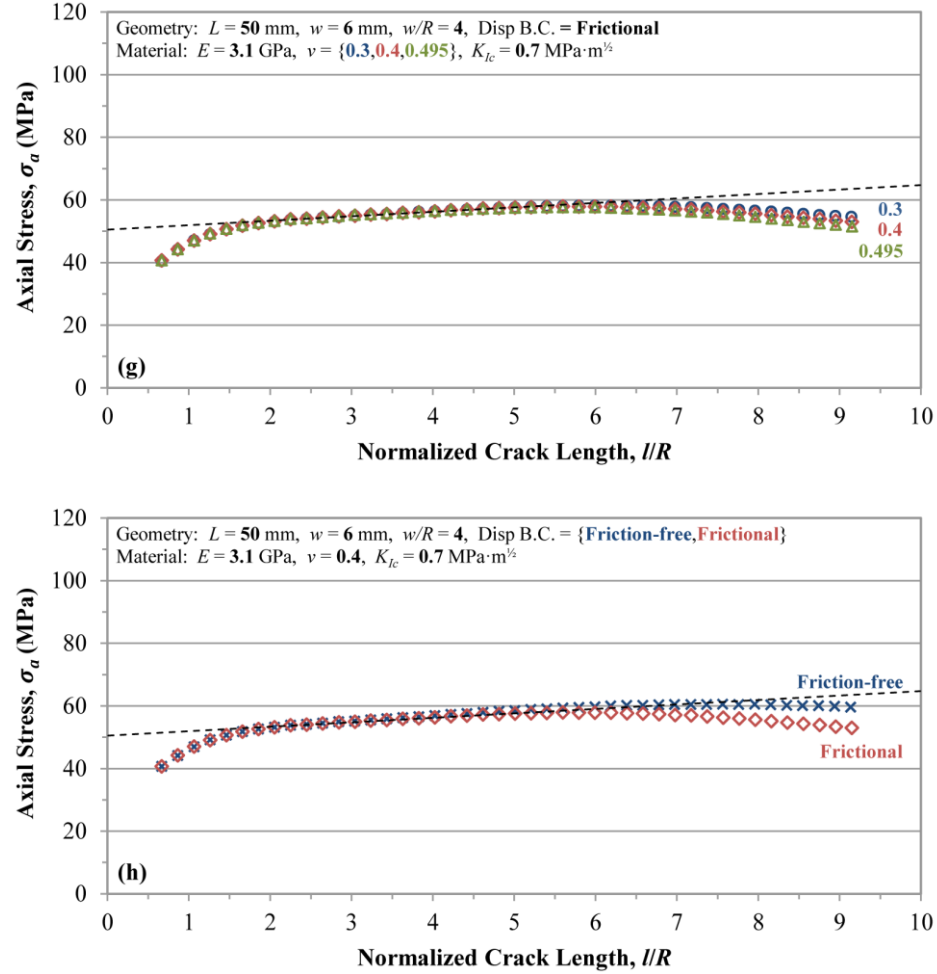
Figure 6.2   Simulation results continued for the experimental conditions in Chapter 5, with the sample Poisson's ratio (g) and displacement boundary condition (h) varied.

6.2.1   Length, *L*

Sample lengths of 30, 50, and 100 mm were investigated. Crack growth in the 50 mm case became unstable beyond a normalized crack length of 5.6.   Increasing the sample length to 100 mm postponed the onset of the instability.   This suggests the instability is related to the end conditions, an ironic finding as it's the end conditions that ensure stability at the end of the test.   Indeed, crack growth in all cases was ultimately arrested by the flat, frictional boundary conditions, as seen by the sharp increase in

applied stress at the end of the 30 mm test (similar results at the end of the 50 and 100 mm tests are not shown). The simulations show good initial agreement between the 50 and 100 mm cases, indicating that 50 mm is a sufficient sample length for the material properties and other geometric parameters. The 30 mm sample was clearly influenced by the end conditions at every point of the test, but was stable over most of the crack growth.

6.2.2 Width, $2w$

Sample widths of 8, 12, and 16 mm were tested. Increasing the width decreased the axial stresses required to propagate a crack. Reducing the width delayed the onset of unstable crack growth, similar to the effect observed by increasing sample length. Since the hole size has to decrease proportionally with the width to maintain the w to R ratio, narrower samples can support longer crack lengths, making them effectively taller. This analogy does not explain the decrease in stress required to drive the crack.

6.2.3 Hole Radius, R

Sample half-width to hole radius ratios (w/R) of 2, 3, 4, and 5 were studied by varying the hole size. Increasing the ratio significantly increased the axial stresses required to propagate both short and long cracks. Crack growth in the $w/R=2$ sample did not become unstable, while the $w/R=3$, 4, and 5 samples became unstable at increasing normalized crack lengths.

6.2.4   Critical Stress Intensity Factor, K_{Ic}

Critical stress intensity factors of 0.4, 0.7, and 1.0 MPa·m$^{\frac{1}{2}}$ were considered. Increasing the critical stress intensity factor increased the axial stresses required to propagate the crack. Since increasing K_{Ic} corresponds to the crack releasing more energy per unit length, higher axial stresses are required to increase the internal energy available for crack growth.

6.2.5   Young's Modulus, E

Young's moduli of 1, 3.1, 10, and 73 GPa were investigated. The lowest modulus (E=1 GPa) sample required the least axial stress of the three cases to propagate the crack. Crack growth was unstable during most of the simulation. In order to generate sufficient internal energy for crack growth, more axial strain was required in the low modulus sample. This led to increased geometric nonlinearity created by additional lateral displacement and bending. By contrast, increasing the modulus of the material led to stable crack growth over a longer range of crack lengths.

6.2.6   Poisson's Ratio, ν

Poisson's ratios of 0.3, 0.4, and 0.495 were tested. Before the instability, the axial stresses required for crack growth were similar for all three cases. During unstable crack growth, increasing the Poisson's ratio decreased the necessary axial stresses. Moving towards the volume-preserving condition (ν=0.5), more energy goes into lateral displacement and bending, increasing the geometric nonlinearity of the sample.

6.2.7 Displacement Boundary Condition, B.C.

The influence of the displacement boundary condition on the fracture behavior of the DCDC test was considered. Specifically, a frictionally-confined case was compared with a laterally unconfined case (e.g. grease has been applied to the loading platens). The friction-free condition postpones the onset of unstable crack growth in a manner similar to having a longer sample. If conserving material is important, greasing the platens may provide a similar benefit for stable crack growth as lengthening the sample.

6.3 Estimating K_{Ic}

The He et al. (1995) and Plaisted et al. (2006) models for estimating K_{Ic} were applied to the axial stress versus crack length simulation results. Generally, the estimates of fracture toughness varied significantly from the prescribed values, and the overall linear fits were poor. Both models fail to properly capture the slope of the data, with He's empirical model expecting a relatively steep slope and Plaisted's theoretical model expecting a constant plateau stress. The simulation results exhibit a wide range of slopes. Earlier models given by Michalske et al. (1993) and Sammis and Ashby (1986) were also considered and found to give poor fits of the data and estimates of K_{Ic}.

Inspecting the simulation results, a linear region is apparent during long crack growth, typically from approximately $l/R=2$ to $l/R=5$. A linear fit was applied to this region in each simulation. The parameters of these fits are given in Table 6.1. The y-intercept of the linear fit, σ_0, appears to only depend on the sample width, hole size, and critical stress intensity factor. Plotting σ_0 as a function of these parameters (Figure 6.3 solid squares) gives an approximately linear relationship. A simple model:
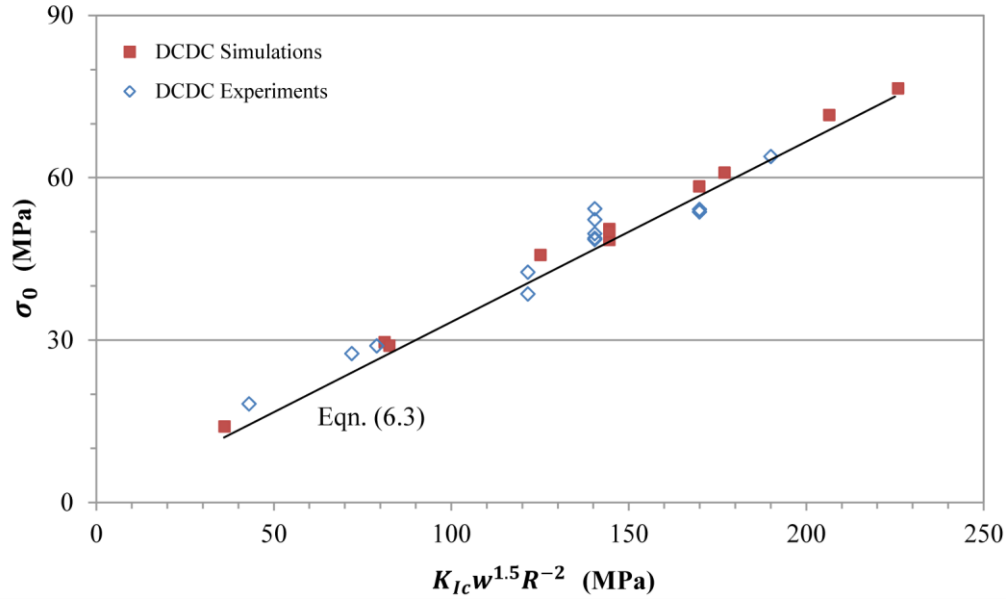
Figure 6.3 The σ_0 fit parameters from the simulation results (solid squares) and experimental results (open diamonds) are plotted and compared with a simple linear model: equation (6.3).

$$\frac{K_{Ic}}{\sigma_0\sqrt{w}} = 3\left(\frac{R}{w}\right)^2, \tag{6.3}$$

is found to closely follow the observed behavior (Figure 6.3 line), with an R-squared value of 0.998.

6.4 Comparison with Experiments

Published DCDC experimental results (Michalske et al. 1993; Plaisted et al. 2006; Nielsen et al. 2012) were compared with equation (6.3). The linear fit parameters (m, σ_0) for the experimental data are listed in Table 6.2, and the results are plotted as hollow diamonds in Figure 6.3. The experimental points follow the same linear trend observed in the simulations results, although with more variation from the simple linear model (R^2=0.954).

Table 6.2   Experimental DCDC geometries, material properties, boundary conditions, and linear fits of the long crack regimes. A single fit was used for experimental results that appeared to have to similar linear regions.

Data Source	Geometry				Material			B.C.	$\sigma_a = m\left(l/R\right) + \sigma_0$	
	w/R	w (mm)	L (mm)	t (mm)	E (GPa)	K_{Ic} (MPa·m$^{\frac{1}{2}}$)	ν		m	σ_0 (MPa)
Michalske et al. 1993	3.75	3.75	75	6.5	73	0.740	0.17	Frictional	6.6878	54.112
Michalske et al. 1993	3.75	3.75	75	6.5	73	0.740	0.17	Frictional	6.5426	53.664
Plaisted et al. 2006	2	4	50	11	3.1	0.68	0.4	Frictional	1.5598	18.186
Plaisted et al. 2006	2	4	100	11	3.1	0.68	0.4	Frictional	1.5598	18.186
Plaisted et al. 2006	3	6	50	11	3.1	0.68	0.4	Frictional	0.6956	28.901
Plaisted et al. 2006	3	6	100	11	3.1	0.68	0.4	Frictional	0.6956	28.901
Plaisted et al. 2006	3	8	100	11	3.1	0.68	0.4	Frictional	0.5890	27.525
Plaisted et al. 2006	4	8	50	11	3.1	0.68	0.4	Frictional	1.0554	42.561
Plaisted et al. 2006	4	8	100	11	3.1	0.68	0.4	Frictional	0.5155	38.488
Plaisted et al. 2006	5	8	50	11	3.1	0.68	0.4	Frictional	1.1592	63.895
Chapter 5	4	6	50	3	3.1	0.68	0.4	Frictional	0.8603	48.793
Chapter 5	4	6	50	4	3.1	0.68	0.4	Frictional	0.9449	48.600
Chapter 5	4	6	50	5	3.1	0.68	0.4	Frictional	0.9386	49.628
Chapter 5	4	6	50	8	3.1	0.68	0.4	Frictional	0.6409	52.228
Chapter 5	4	6	50	11	3.1	0.68	0.4	Frictional	0.5447	54.254

Linear fits of the experimental data from Michalske et al. (1993) and simulation results for the same geometry and material (Figure 6.2a) yield fit parameters (σ_0) that straddle the line given be equation (6.3), with the experimental parameters 8 % below the simulation parameter. Since the stress versus crack length data from the experiments and simulation are similar over the period of crack growth where they coincide, the discrepancy could be attributed to the lack of experimental data points before l/R=3. The simulation results were fit between l/R=2 and l/R=5. Having sufficient data points and choosing the appropriate domain for fitting are two challenges associated with linear extrapolation and applying equation (6.3).

Data for PMMA from Plaisted et al. (2006) was grouped by sample geometry and linear fits were applied to the initial portions of the long crack regimes. The critical stress intensity factor was assumed constant and the average of the range determined in Chapter 5.5. The average fit parameter σ_0 from the each group of experimental data was compared with equation (6.3) and generally in good agreement, although two of the geometries show a >10 % variation. In the case of the w/R=2 samples, most had a limited number of data points for fitting, which led to wide variation in the fit results. The longer, 100 mm w/R=4 samples required lower axial stresses for crack propagation than the 50 mm w/R=4 samples. This effect was not observed in the simulation results presented earlier, although a different sample width had been considered. Additional simulations could be helpful in understanding the effect of sample length.

The experimental results from the DCDC sample thickness study conducted by Nielsen et al. (2012) show an increase in the axial stresses required to propagate long cracks in thicker samples. This translates to an increasing fit parameter σ_0. Since the linear model, equation (6.3), was developed using two dimensional simulations, thickness is not considered, and the associated changes in σ_0 leads to variation in the results. For the assumed K_{Ic} for PMMA, the thinnest samples show the best agreement with the linear model. This correlates with the conclusion in Chapter 5.7 that the two dimensional simulations are more applicable to the thinner tested geometries.

6.5   Discussion and Conclusions

A series of finite element simulations were used to investigate the effect of sample geometry, material properties, and displacement boundary condition on crack

growth behavior during the DCDC fracture test. The results indicate that the axial stress necessary for crack propagation can be reduced by selecting a material with a low K_{Ic} and low modulus and using a relatively wide sample with a large hole. A period of unstable crack growth was observed in most simulations, and appears to be primarily influenced by the material properties as well as the location and boundary condition of the sample ends.

The DCDC experimental results given in Chapter 5.4 were inspected to look for indications of crack instability. The simulations indicate unstable crack growth should have started at a normalized crack length of 5.6, but no rapid jumps in crack length were noted during testing of the 8 and 11 mm thick samples, the only ones with cracks that exceeded this critical length. Reviewing the data, six of the seven thick samples tested show a slight decrease in the applied stress beyond a crack length of ~7. Modifying the simulation method to properly consider unstable crack growth also shows a small decrease in the stress that is likely due to lateral displacement and bending in the sample. While the simulation considered a linear elastic material, the experiments were conducted on PMMA, a viscoelastic polymer. Local, non-linear and time-dependent inelastic deformation around the hole where the compressive stresses were magnified by the geometry may have slowed or masked the unstable crack growth during experiments. In comparing the pictures of the crack surfaces with the data, it is also apparent that the crack growth was unstable in the thick samples as the tests were stopped and the samples unloaded (Figure 5.13). The crack length in the picture taken after unloading far exceeds the final data point recorded. The test had been stopped soon after the final data point,

and the sample was rapidly unloaded over the course of a few seconds. The picture suggests the cracks grew rapidly as the sample was unloaded.

The linear region of the long crack regime was used to develop a simple estimate of K_{Ic}: equation (6.3). While the models given by He et al. (1995) and Plaisted et al. (2006) are applicable to separate, limited ranges of materials and geometries, the empirical model given here was found to give reasonable estimates of K_{Ic} for all considered DCDC cases. A drawback of this model is that the linear region is not always obvious for fitting, and there is variation in the appropriate range of crack lengths. Care must be taken in applying this model to experimental data. Unstable crack growth can be hard to distinguish from stable growth, as noted for a viscoelastic material like PMMA. Developing a model that considers the slope of the linear fits as a second parameter may help. The ability to predict the slope of the crack growth behavior in the long crack regime would also be useful for cases where a constant plateau stress is desired (Hamilton et al. 2012).

The model given here was developed empirically and does not illuminate the underlying reasons for the observed behavior. Future work will focus on understanding these reasons and developing a complete, theory-based model. A fracture mechanics approach outlined by Amirkhizi (2012) offers hope that the model given by Plaisted et al. (2006) can be modified and improved to apply to all of the DCDC geometries, materials, and boundary conditions considered in the present work.

Chapter 7

Healing Damage in Thermally Reversible Polymers

In Chapter 5, each PMMA double cleavage drilled compression (DCDC) sample was tested only once since the cracks could not be healed without flowing the thermoplastic polymer chains. In this chapter, the damage healing capabilities of polymers with thermally reversible cross-linking bonds are investigated. Specifically, mechanical damage, including scratches and cracks, and thermal degradation are considered.

7.1   Mechanical Damage: Scratches

The simplest method of observing the thermal reversibility of Diels-Alder (DA) adducts is imparting small scratches on a sample and healing them with a thermal treatment. Since the scratching process removes a small amount of material, the polymer must be flowed across the gap in a manner similar to thermoplastic healing. Unlike a thermoplastic however, once the sample cools, the DA reaction will re-establish covalent cross-links and the sample will harden. Given the simplicity of the experiment, intuitive results, and small quantity of required material, this qualitative method of verifying thermal reversibility would be useful as a teaching tool in an organic chemistry laboratory class (Weizman et al. 2011).

Scratch healing was applied to two polymers shown by differential scanning calorimeter (DSC) measurements in Chapter 3 to have thermally reversible DA adducts: DPBM4FS and 2MEP4FS.

7.1.1 DPBM4FS

A thin sample of DPBM4FS was prepared for scratching and healing. The commercial maleimide DPBM was dissolved in dichloromethane (DCM) and combined with a stoichiometric proportion of the synthesized furan, 4FS. A few drops of the solution were deposited on a hot glass slide, and the slide was placed in a 120 °C oven for 2 hours and allowed to slowly cool to room temperature overnight. The rapid heating and large surface area of the solution on the slides removed the DCM solvent, leaving the DPBM and 4FS monomers to polymerize. The sample was lightly scratched with a razor blade, then heated to 120 °C to activate the retro-Diels-Alder (rDA) reaction and flow the material at the interface (Figure 7.1). After 2 hours, the scratch had mostly disappeared.
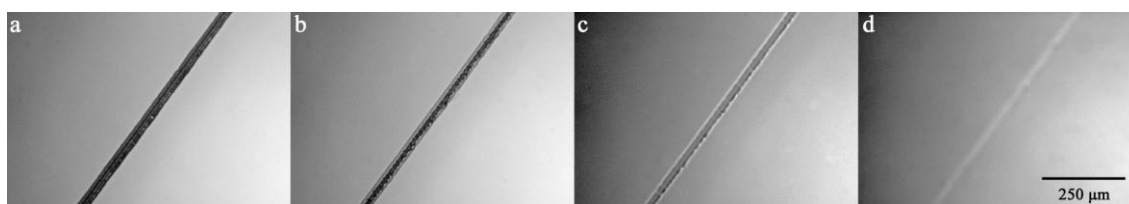
Figure 7.1   Optical microscopy is used to view a scratch in a thin layer of DPBM4FS (a). After 5 min (b), 1 hr (c), and 2 hr (d) at 120 °C, the scratch is nearly gone.

7.1.2 2MEP4FS

Polymer 2MEP4FS was prepared using a solvent-based mixing process and tested in a similar manner to DPBM4FS. Monomer 2MEP was dissolved in DCM and mixed with a stoichiometric proportion of 4FS. The solution was dripped onto a hot slide, and the resulting thin film of prepolymer was cured at 95 °C for 5 hours before slowly cooling to room temperature overnight. The curing temperature and time were selected based on the DSC results in Chapter 4 showing 2MEP4FS cured under these conditions will have a maximum number of established cross-links. DSC measurements of the cured sample confirmed full conversion was achieved, indicating all of the DCM solvent had been removed.

The sample was lightly scratched and then healed in a 125 °C oven. After 2 hours, the scratch had mostly disappeared (Figure 7.2), similar to the observations made of DPBM4FS. The sample was lightly scratched a second time in a virgin region of material and healed again at 125 °C. After 3 hours, the second scratch had only partially healed (Figure 7.3), indicating the polymer wasn't softening and flowing as readily as it had during the first healing treatment. Thermal damage is investigated in Chapter 7.3.

7.2   Mechanical Damage: Cracks

DSC and dynamic mechanical analyzer (DMA) measurements in Chapter 3.1 indicate abutting crack faces in 2MEP4FS can be healed by re-establishing Diels-Alder adducts. Since no material is removed like in a scratch, polymer chains do no need to flow and the sample can retain structural integrity during healing. The double cleavage drilled compression (DCDC) fracture test studied in Chapters 5 and 6 was applied to
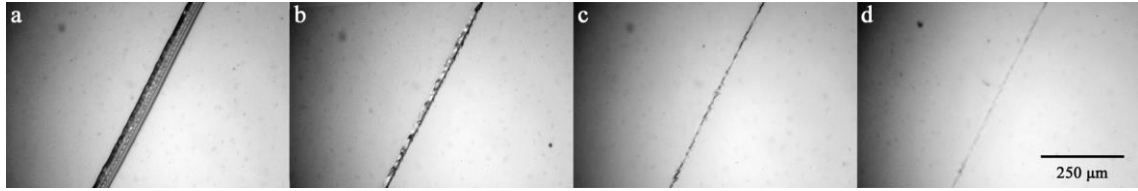
Figure 7.2   Optical microscopy is used to view a scratch in a thin layer of 2MEP4FS (a). After 5 min (b), 1 hr (c), and 2 hr (d) at 125 °C, the scratch is nearly gone.
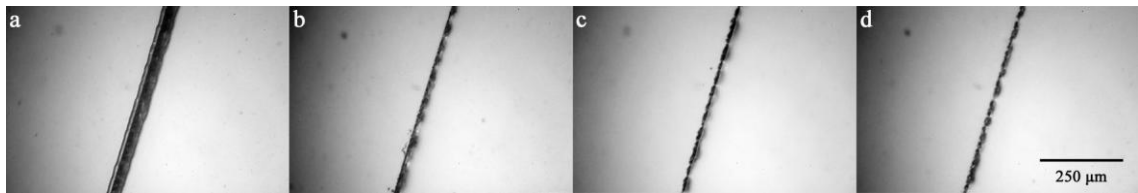
Figure 7.3   A second scratch on the thin layer of healed 2MEP4FS (a). After 5 min (b), 1 hr (c), and 3 hr (d) at 125 °C, the scratch has only partially healed.

2MEP4FS as a quantitative method of introducing cracks and measuring healing efficiency.

7.2.1   Experiments

The DCDC test uses applied compression to drive tension cracks in a sample. A more detailed description of the test and experimental setup is given in Chapter 5. Plaisted and Nemat-Nasser (2007) were the first to use this fracture geometry to establish the healing efficiency of a re-mendable polymer. 2MEP4FS samples were fractured and healed multiple times. The healing efficiency, η_h, was determined from a ratio of the stresses required for crack propagation in the healed and virgin cases:

$$\eta_h = \frac{\sigma_{crit}^{healed}}{\sigma_{crit}^{virgin}}. \qquad (7.1)$$

Complete recovery of the fracture strength was obtained (Figure 7.4) with a two-step healing procedure; (1) the sample was heated to 85 °C with light lateral pressure pushing the crack faces together (Figure 7.5), followed by (2) 95 °C with no applied pressure. Healing was determined to be independent of the dwell time at each step, provided the sample reached thermal equilibrium. As brief as 30 minutes per step yielded full recovery of fracture strength as observed during the subsequent DCDC test.
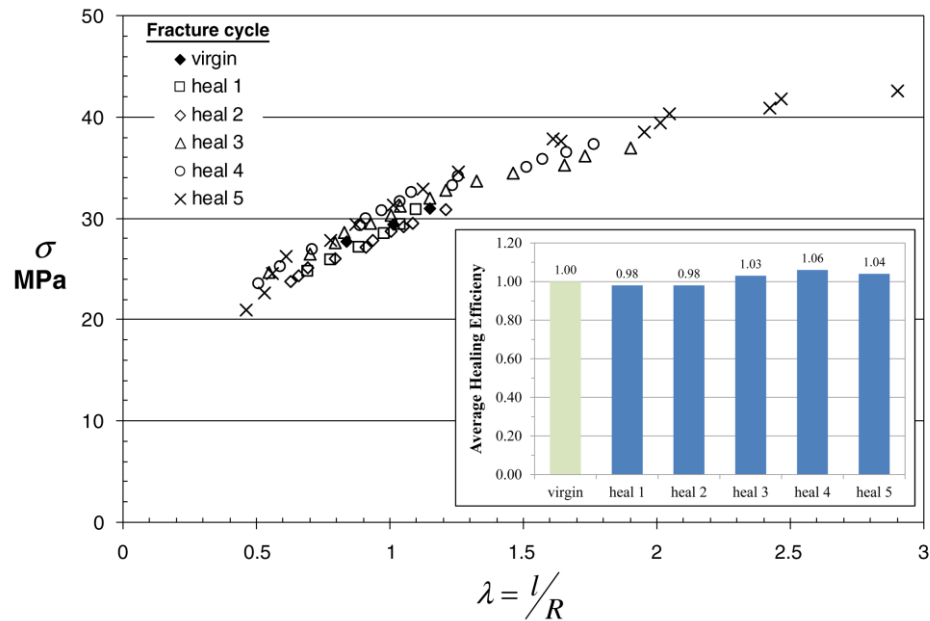
Figure 7.4   DCDC experimental results for 2MEP4FS for DCDC specimen 1 in Plaisted and Nemat-Nasser (2007). (insert) Average healing efficiencies.
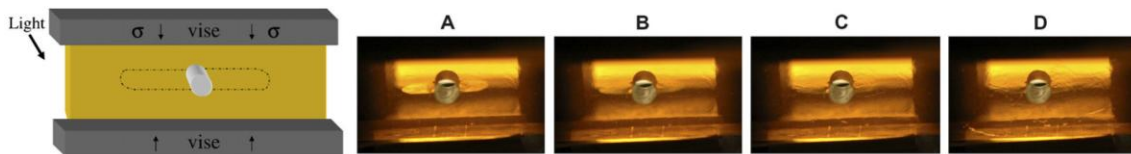
Figure 7.5   DCDC cracks healing at 85 °C under light pressure: after (a) 0 min, (b) 2 min, (c) 4 min, and (d) 15 min. (Plaisted and Nemat-Nasser 2007)

In the present work, a 2MEP4FS DMA sample was repurposed for DCDC testing to conserve material. After machining, the sample measured 30 mm tall, 12 mm wide, and 3.3 mm thick. Most of Plaisted and Nemat-Nasser's specimens had a w/R ratio of 4, but preliminary tests using PMMA indicated that ratio could cause the present geometry to buckle out of the sample plane at the loads necessary for crack propagation. Therefore, a 4 mm diameter central hole was used, giving the sample a w/R ratio of 3 and reducing the forces required for crack propagation. The sample was notched and pre-cracked using axial compression, and a confinement jig prevented the initial cracks from growing too long. DCDC testing was conducted at a constant 0.135 µm/sec displacement rate, chosen so the strain rate matched the average strain rate used by Plaisted and Nemat-Nasser (2007).

The sample was DCDC tested ten times (Figure 7.6). After testing, the sample was immediately healed, initially using the procedure from Plaisted and Nemat-Nasser (2007). Table 7.1 gives the healing efficiency at two crack lengths and the associated healing procedure before each test. During the first DCDC test (Figure 7.7), the cracks grew in discrete jumps, creating steps in the data. The average stress at each step was used for comparisons. Crack growth in subsequent tests was relatively smooth. After three tests the thermal treatment was adjusted to improve the healing. Changing the times, temperatures, and lateral pressure resulted in some improvement, with 72 % maximum recovery at a normalized crack length of 1.5. During the first nine DCDC tests, the cracks were grown only within the short crack regime. During the tenth test, the cracks were grown into the long crack regime. They grew into virgin material at stresses approximately 25 % below the maximum during the first test. Confinement braces for
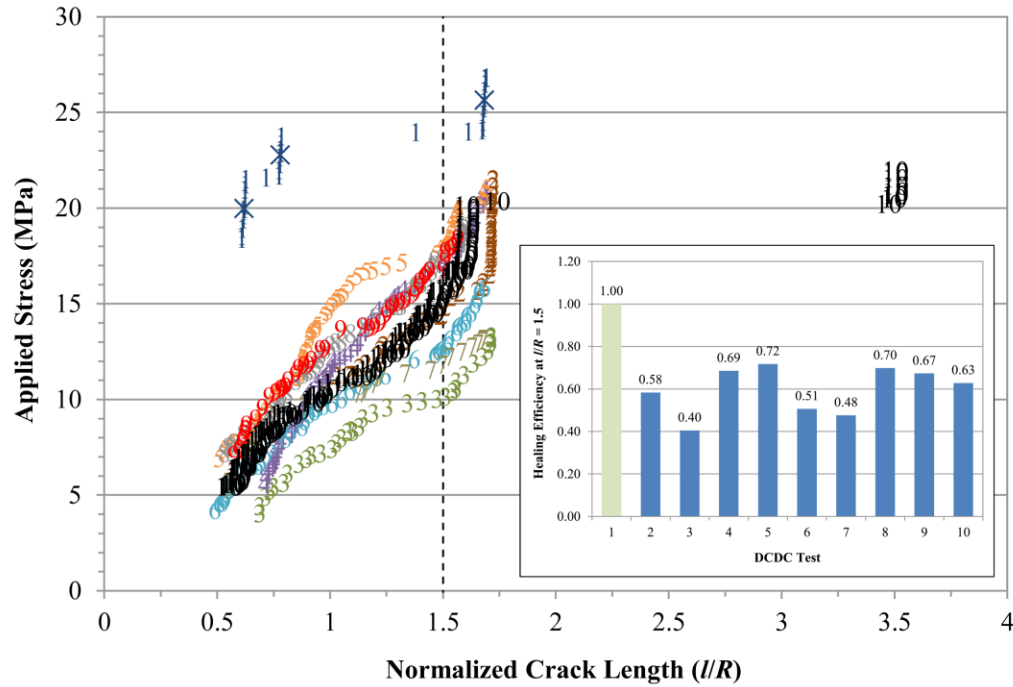
Figure 7.6 DCDC results for all ten tests. Data points are marked by the test number. The average of each step in test 1 (×) was used for comparisons with other tests. (insert) Healing efficiencies for each test at a normalized crack length of 1.5. Linear interpolation was used between data points when calculating stresses.

Table 7.1 Ten DCDC tests were conducted on one sample. The preceding healing steps (including time, temperature, and pressure if applied) are separated by semicolons.

DCDC Test	Preceding Healing Procedure	Healing Efficiency, η_h	
		l/R=0.78	l/R=1.5
1	Virgin	1	1
2	30min 85°C 350kPa; 30min 95°C	-	0.583
3	30min 85°C 350kPa; 30min 95°C	0.246	0.405
4	30min 85°C 350kPa; 30min 95°C; 30min 100°C	0.344	0.686
5	30min 85°C 350kPa; 4hr 100°C	0.466	0.717
6	30min 90°C 350kPa; 30min 100°C	0.345	0.506
7	30min 90°C 530kPa; 30min 100°C	-	0.476
8	30min 90°C 700kPa; 30min 100°C; 15min 110°C; 30min 120°C	0.421	0.698
9	30min 90°C 700kPa; 12hr 100°C	0.465	0.673
10	30min 90°C 700kPa; 2hr 100°C; 2hr 90°C 700kPa; 30min 100°C	0.404	0.628
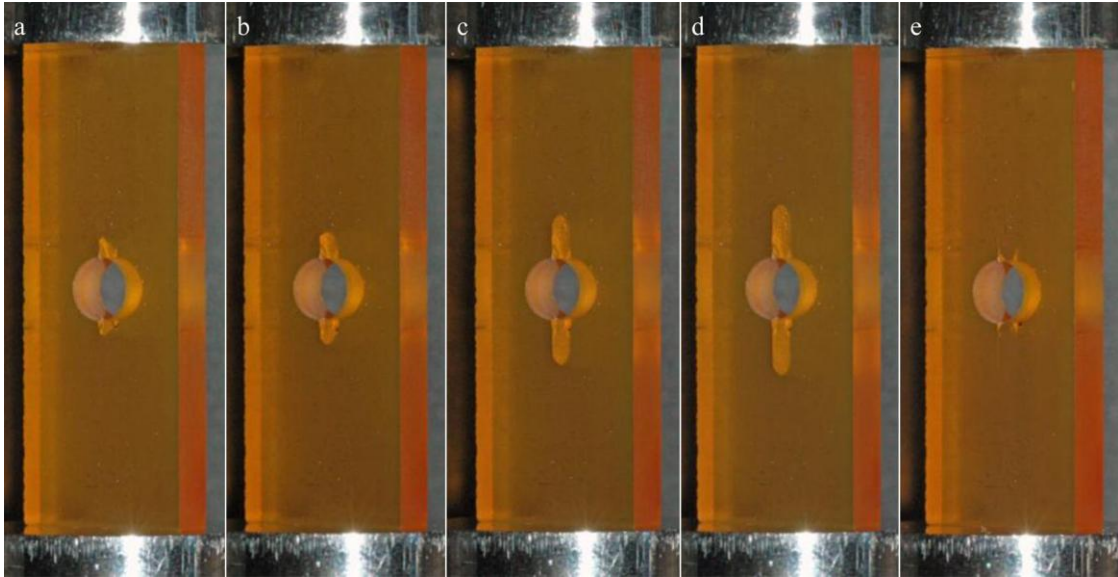
Figure 7.7   2MEP4FS DCDC test 1: (a) the cracks have been initiated and the sample is ready for DCDC testing; (b), (c) the cracks grow as compression is applied; (d) the test is stopped; and (e) the sample after healing.

the top and bottom edges were used to ensure the cracks did not grow to the ends of the sample. Attempts to heal the longer cracks were unsuccessful, with large crack areas still evident after several thermal treatments. More extreme thermal treatments led to dimension changes in the sample, preventing further testing and comparison. Similar long crack problems were encountered by Plaisted and Nemat-Nasser (2007), who attributed them to inelastic deformation around the hole preventing proper abutting of the crack faces during healing.

The shape of the crack tips changed over the life of the sample. In initial tests, they had thumbnail shapes similar to the crack tips observed in PMMA DCDC samples (Chapter 5). This shape is expected since crack propagation at the free surfaces should be more difficult than at the center of a sample (Dowling 1999). With each new fracture test, the crack tip shape becomes flatter and eventually inverts (Figure 7.8). This
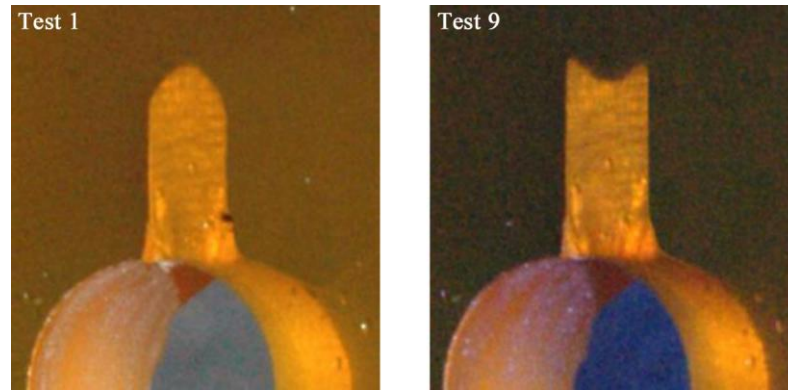
Figure 7.8 Angled view of a DCDC crack during test 1 (left) and test 9 (right). Color differences are due to changes in camera settings and lighting.

suggests healing at the free surfaces is incomplete, allowing the cracks to propagate more easily in these regions. Incomplete healing could be related to the relatively thin sample geometry (3.3 mm). Contamination or mismatches at the free surfaces during healing would have significantly more effect on a thin specimen, where a larger percentage of the crack area is near a free surface. Plaisted and Nemat-Nasser (2007) used 8 to 9 mm thick DCDC samples and didn't experience the same problem.

7.2.2   Computational Analysis

The experimental data was analyzed to estimate the critical stress intensity factor, K_{Ic}, for 2MEP4FS. Data from the virgin and 8th DCDC tests provided the bases for a series of simulations and calculations detailed in Chapter 5.5. The finite element model (Figure 7.9 insert, left) consisted of 1022 two-dimensional, plane stress shell elements and a linear, isotropic material model. For the virgin case, the average stress at each step in the data was determined and used for the simulation. The maximums and minimums of the steps were considered as limits on the range of stress intensity factors. Data from

Plaisted and Nemat-Nasser (2007) was also analyzed for comparison with the present research. The virgin test of specimen 3 was simulated using a finite element model (Figure 7.9 insert, right) with 2232 two-dimensional, plane stress shell elements and the same linear, isotropic material model.

The results of the simulations are given in Figure 7.9. The repurposed 2MEP4FS DMA sample has an average virgin K_{Ic} of 0.58 MPa·m^{½}, with a ± 0.03 MPa·m^{½} range due to the steps during crack growth. Plaisted and Nemat-Nasser's DCDC data and geometry yields an average virgin K_{Ic} of 0.48 MPa·m^{½}. At a normalized crack length of 1.5 where there is overlap between the tests, the repurposed DMA sample's K_{Ic} is 30 % higher.
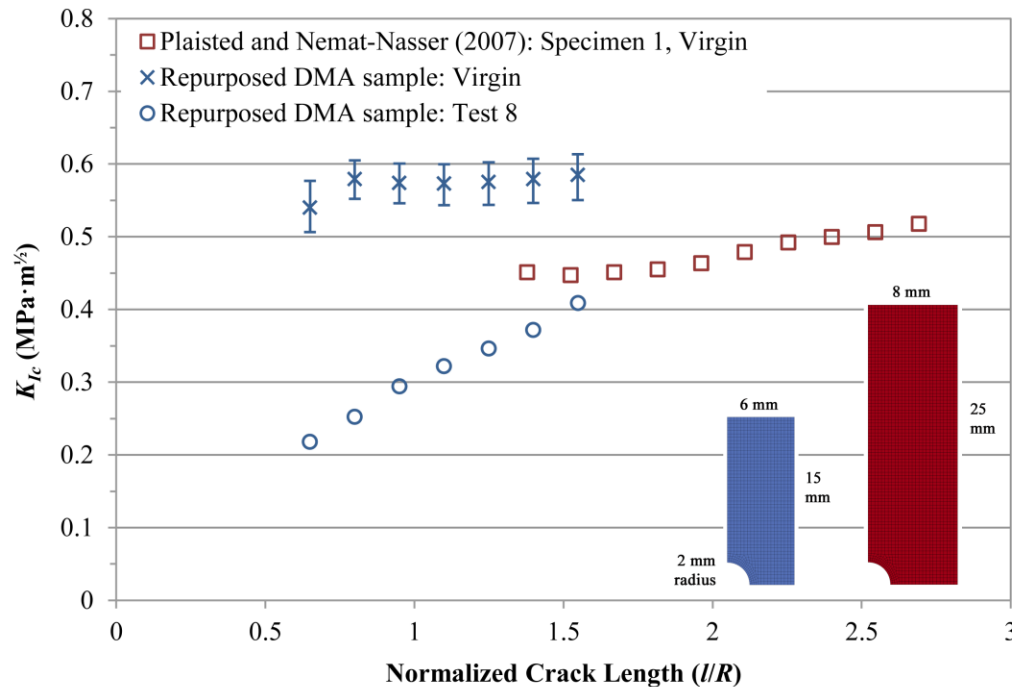
Figure 7.9 Estimated critical stress intensity factors for 2MEP4FS. The error bars represent the maximum and minimums associated with the steps in the repurposed DMA sample DCDC data. (insert) Finite element models for the repurposed DMA sample (left, blue) and Plaisted and Nemat-Nasser (2007) sample (right, red).

Since the experiments use different geometries and the models make several approximations, the DCDC experiments and simulations were repeated using PMMA. Since the samples were made from the same known material, variations in the results are attributed to the sample geometry. At a normalized crack length of 1.5, the smaller 30 mm tall sample yielded a K_{Ic} 13 % higher than the larger 50 mm tall sample. This means more than half of the increase in K_{Ic} is due to the 2MEP4FS polymer. Changes in the monomer synthesis and polymerization methods could have contributed to the calculated differences in fracture properties. DSC measurements in Chapter 4 suggest the current 2MEP4FS polymer has more established DA adducts, which may toughen the material.

7.3   Thermal Damage

Incomplete healing of the second scratch on the 2MEP4FS sample in Chapter 7.1 suggests extended time at elevated temperatures where the rDA reaction occurs may damage the healing capability of the polymer. The effect of time spent at rDA temperatures was investigated using DSC. Three samples from a single piece of cured 2MEP4FS were separately sealed in aluminum pans and heated to 130 °C, where they were held isothermally for 5 min, 1 hr, and 5 hr respectively. At the end of the prescribed period of time, each sample was quenched in liquid nitrogen, warmed to room temperature, and characterized using DSC (Figure 7.10). The exothermic peak at 80 °C associated with the re-establishment of DA adducts is the largest for the sample that spent the minimum time at the elevated temperature. Conversely, the heat flow associated with the sample that spent the most time at 130 °C exhibited no exothermic peaks. Between room temperature and ~85 °C, the heat flow is essentially constant, similar to the
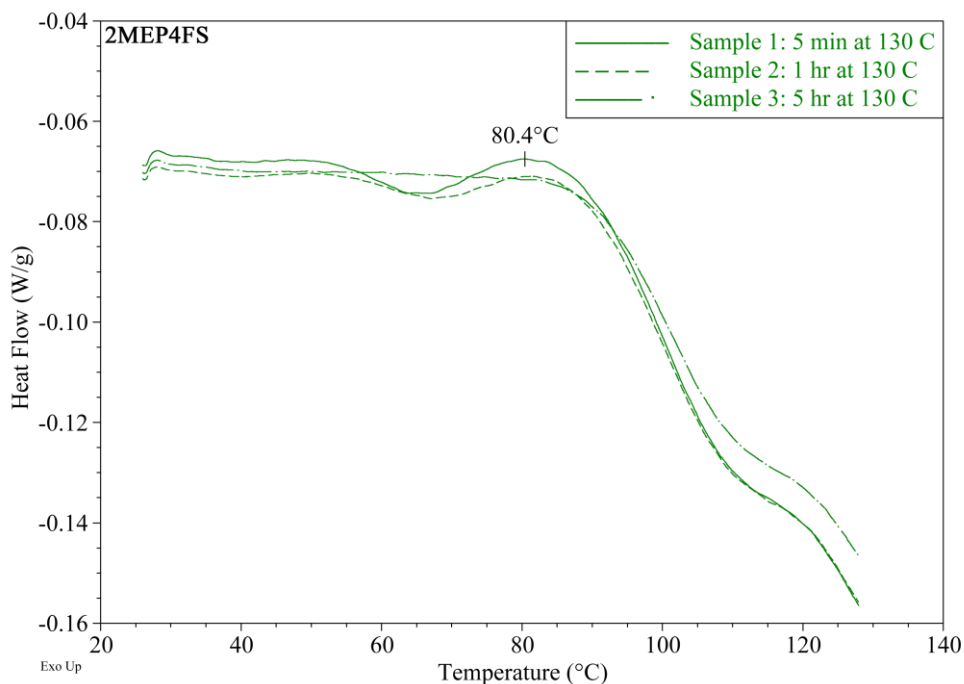
Figure 7.10 2MEP4FS samples after being held at 130 °C for different periods of time. The peak associated with the formation of DA bonds at 80 °C decreases then disappears with increasing time.

quenched DSC results for 2MEP3FT (Chapter 3.2). This behavior indicates no DA adducts are being re-established in the sample.

A sample of cured 2MEP4FS polymer under high vacuum was heated on a benchtop hot plate to 150 °C. At this temperature, the solid polymer turned into a liquid. The liquid had a sufficiently low viscosity that a small magnetic stir bar could easily turn. Over the course of 20 minutes, the viscosity of the liquid increased as observed by the slowing rotation of the stir bar. Eventually, the stir bar stopped moving and the polymer solidified. Increasing the temperature did not lead to the sample softening again. Studying the DSC results for 2MEP4FS, there is a large exothermic peak at these

temperatures (Figure 3.8). The benchtop heating observations suggest this peak is associated with an irreversible reaction occurring in the polymer.

While mechanical damage like cracks can be repeatedly healed, 2MEP4FS appears to be susceptible to thermal damage at elevated temperatures. To avoid thermal damage, polymerization and healing thermal treatments should be kept below rDA temperatures where the DA adducts separate. Increased mobility of the monomers and functional groups at high temperatures may facilitate irreversible chemical reactions.

Chapter 8

Healable Composites: Fabrication

A healable polymer with thermally reversible cross-links would be useful as the matrix constituent in a fibrous composite. Possible fabrication approaches are explored and discussed.

8.1   Challenges

There are several difficulties in creating high-quality neat or fiber-reinforced composite samples using a two-part re-mendable polymer like 2MEP4FS. At room temperature, 2MEP is a solid powder and 4FS is a viscous liquid. The most direct approach is simply mixing the monomers in these states. The 2MEP is partially soluble in 4FS (Wudl 2004), and with sufficient vigorous stirring, the mixture will become macroscopically uniform. Heating the mixture will polymerize the monomers and create 2MEP4FS polymer. But there are several problems with this method. At room temperature, the combined monomers will harden to form a solid over the course of tens of minutes to an hour. This amount of time is not sufficient for removing the myriad of bubbles introduced by the powder and stirring action. Heating the mixture under vacuum will reduce the viscosity and allow more trapped or dissolved gases to be pulled out, but the polymerization rate will increase.

Although the mixture can be visually uniform at room temperature and eventually transparent as the 2MEP melts during heating, the final polymer doesn't form the same

number of DA adducts as a sample prepared by melting the 2MEP monomer before mixing and polymerization are completed. In Chapter 4.4.1, the measured exothermic energy associated with polymerization of manually-mixed 2MEP and 4FS monomers was measured to be less than the case of melted 2MEP mixed with 4FS. Some of the energy difference was attributed to polymerization energy being consumed by the melting of 2MEP. But, after curing, the manually-mixed sample was measured to have a lower glass transition temperature (T_g) versus the melted mixing case, indicating approximately 6 % fewer DA adducts had formed.

Assuming the hand-mixed monomers can be effectively mixed and polymerized, the mixture must still be integrated with fibers to create a fibrous composite. The high viscosity makes this challenging, and the fine filaments could act as sieves, excluding the undissolved maleimide particles which are still necessary for a stoichiometric reaction.

Combining the monomers as liquids is not a straightforward process. At the elevated temperature of 85-90 °C required to melt 2MEP, a stoichiometric ratio of 2MEP and 4FS must be quickly combined, mixed, and poured into the sample mold. Video analysis suggests the entire process must to be completed in less than two minutes, before the prepolymer becomes too viscous. On a large scale, the process could be streamlined, but at a laboratory level, it tends to create a fair amount of waste. Only limited quantities of each monomer were available.

A single component polymer like polymer 400 has its own set of challenges. Monomer 400 will melt and polymerize at 121 °C and 126 °C respectively, meaning careful control over the heating and a strong vacuum are required to create uniform

samples. Not enough monomer 400 was available to prepare a composite sample in this study.

8.2   Approach 1: Resin Transfer Molding

Plaisted (2007) made the first fiber-reinforced composites with a re-mendable polymer matrix. After having success separately melting the monomers and then mixing them to create neat samples for DMA and DCDC testing, Plaisted extended this approach to making fiber-reinforced samples. The monomers were melted, mixed, and injected into an enclosed mold containing oriented fiber layers (Figure 8.1). The process tended to displace the unidirectional fibers, leading to relatively small regions where a usable sample could be cut out. Plaisted successfully prepared carbon fiber and glass fiber samples using this method.

The injection molding approach was refined by Ghezzo et al. (2010). Rather than forcing 2MEP and 4F monomers down through a diaphragm for mixing and fiber integration, the system was inverted, using gravity to keep the monomers separated during heating and degassing (Figure 8.2). Computer controlled pistons pushed the monomers up through a mixing nozzle into a chamber containing layers of woven carbon fiber.
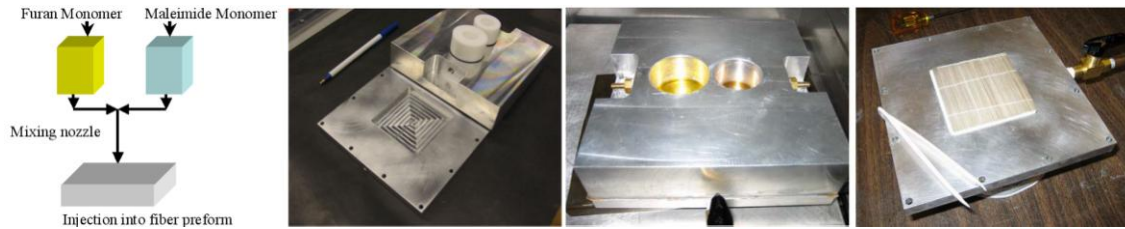
Figure 8.1   The transfer mold used by Plaisted (2007) to create fiber-reinforced 2MEP4FS composite panels.
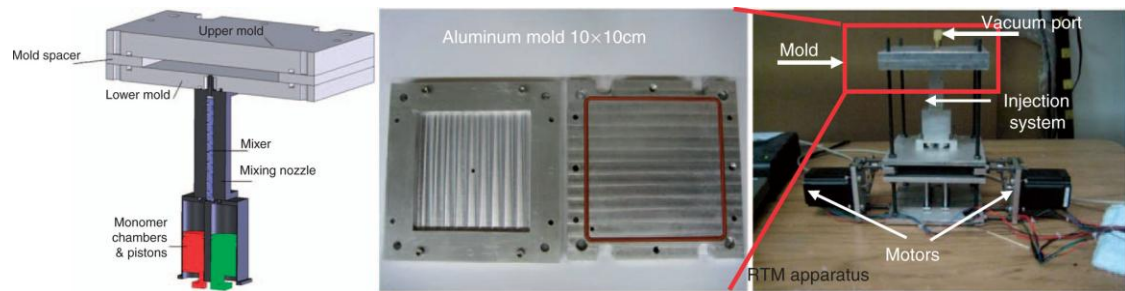
Figure 8.2   The transfer mold for creating 2MEP4F composites developed by Ghezzo et al. (2010).

Both approaches rely on a one step injection process. Once the system is designed and set up, its simplicity is an advantage. The size of the composite panels is limited by the rapid polymerization; the prepolymer can only flow so far. Larger panels must have multiple injection sites and synchronized action, or the composite will have to be molded in multiple stages. A more flexible and adaptable fabrication process would be beneficial, particularly for laboratory applications.

8.3   Approach 2: Solvent-Based Prepreg

A prepreg approach is envisioned for constructing healable composites using polymers with thermally reversible cross-links.   Thin layers of polymer and unidirectional fibers could be stacked in desired orientations and laminated to form a healable composite. A solvent-based approach to mixing and distributing the monomers was investigated.   A solvent ensures uniform mixing of the monomers, and the low viscosity of the solution facilitates distribution in a thin layer of oriented fibers. Chen et al. (2003) used dichloromethane (DCM) solvent to make thick neat polymer samples. A centrifuge had to be used during heating to remove bubbles created during solvent removal. A thin prepreg geometry should facilitate solvent removal without a centrifuge.

DSC samples were prepared to test solvent removal methods. DCM was chosen as the solvent due to its effectiveness dissolving 2MEP and its low boiling point. It was combined with a stoichiometric ratio of 2MEP and 4FS, and the solution was stirred and sonicated until it was transparent and uniform. Thin samples ~1 mm thick were prepared in open DSC pans. Leaving the samples in an open environment tended to allow the solvent to evaporate from the surface, which increased local viscosity and polymerization, trapping solvent below. Upon heating to complete polymerization, the material turned into foam as the trapped solvent would boil. Various combinations of heat and vacuum were also tried with little success. Bubbles were present in the final polymer in every case. Tetrahydrofuran (THF) solvent was also tried with similar results.

Despite the poor DSC results, the solvent-based approach was extended to samples with integrated fibers. Prepreg samples would be thinner than the DSC samples, ~0.3 mm, and the presence of the fibers could aid solvent removal by providing more

surface area within the material. The DCM-monomer solution could be deposited in a layer of fibers and held under low vacuum for 24 hours. Multiple layers could then be laminated and cured under high vacuum using pressure and heat. A polytetrafluoroethylene (PTFE) mold was designed to allow pressure to be applied through the thickness of the sample via a piston while the fibers are constrained from spreading outward in plane (Figure 8.3).

The approach was first used with loose, oriented T300 carbon fibers. After vacuum removal of the solvent over a 24 hour period, the prepreg was solid, but riddled with bubbles and voids. The defects had also displaced the fibers in some regions. After 30 minutes under ~2 MPa pressure in a 120 °C press, the heat was turned off and the sample was allowed to gradually cool to room temperature over a period of 6 hours under continued pressure. All of the bubbles and voids were filled in the single layer composite, but the fibers were further displaced (Figure 8.4). To minimize fiber
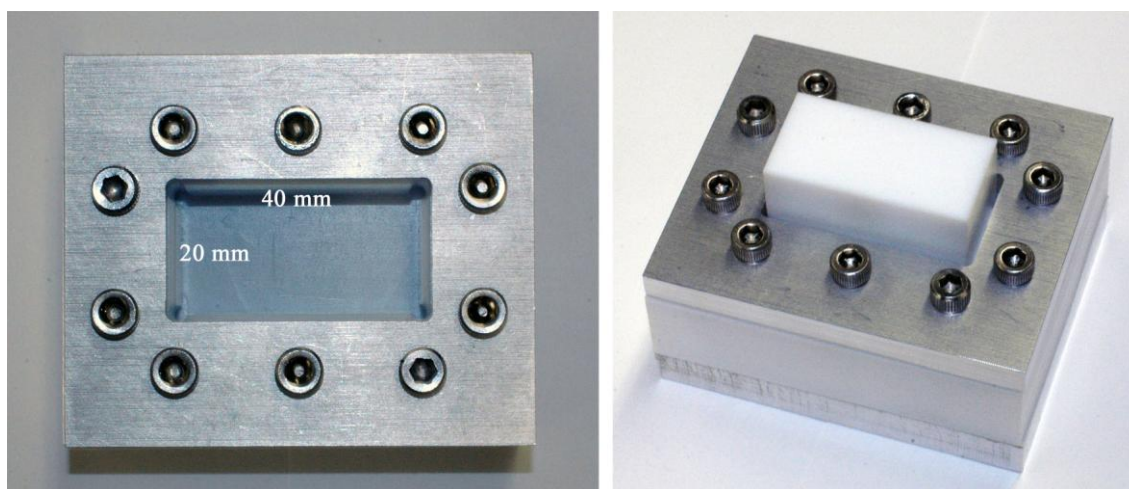
Figure 8.3   A PTFE mold designed to apply pressure to prepreg layers. Heat and pressure were applied in a hot press. A sealed bag around the mold (not shown) allows a vacuum to be held during this process.
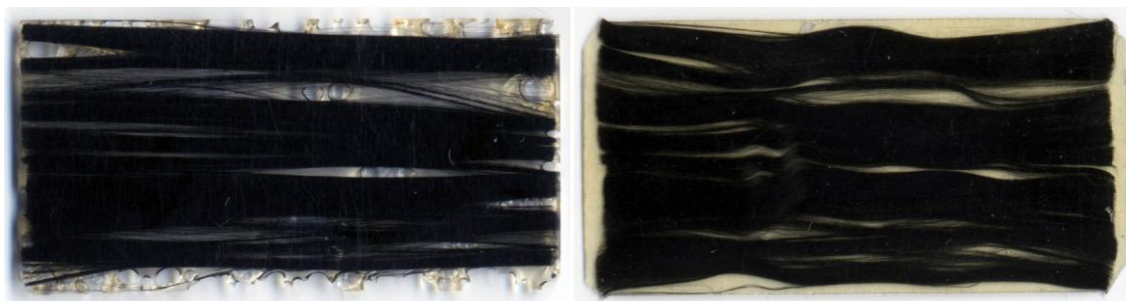
Figure 8.4 Solvent-based 2MEP4FS and T300 carbon fiber. (left) The prepreg layer after 24 hours under low vacuum. (right) The same layer after the application of pressure and heat.

movement, S-glass fibers held together with sparse polyester fill threads were used in a second prepreg layer. Following the same processing approach, the final composite was more unidirectional. Examined using an optical microscope, the polymer appears well integrated with the fibers.

The quality of the solvent-based 2MEP4FS polymer was checked using a similar processing method, but not adding any fibers. After 24 hours under low vacuum, the prepolymer was cured in the mold under pressure for 15 hours at 100 °C. DSC tests of the polymer yield a glass transition temperature at 70 °C, indicating some solvent remained and was acting as a plasticizer. A second sample postcured at 120 °C for 2 hours, had a T_g of 94.3 °C, more in line with cured samples fabricated using other methods.

The results indicate that solvent-based 2MEP4FS at thicknesses comparable to a single layer of unidirectional fiber must be heated to rDA temperatures to fully remove the solvent. At these temperatures, the polymer may have softened enough to allow the

remaining solvent to escape. Removing the solvent quickly displaced loose fibers, creating prepreg layers with inconsistent fiber densities and orientations.

8.4   Approach 3: Controlling the Polymerization Rate

In Chapter 4.2, homogeneous 2MEP4FS prepolymer samples were prepared by using temperature to control the polymerization rate. The monomers were measured and combined at room temperature where the polymerization rate was slow, allowing time to ensure precise stoichiometric ratios. Heating the combined monomers to 90 °C melted the 2MEP and enabled further mixing. Quenching the samples in liquid nitrogen minimized the initial polymerization.

A prepreg process for creating multilayered composites was developed as an extension of this 2MEP4FS prepolymer method. After the quenched homogeneous prepolymer was warmed to room temperature, it was removed from the culture tube and transferred to a unidirectional layer of loose carbon fibers. At this stage, differential scanning calorimetry (DSC) measurements and the conversion model (equation 4.3) indicate the prepolymer had formed approximately 7.5 % of the cross-linking DA adducts present in the final, cured 2MEP4FS. Since room temperature is above the glass transition temperature and the gel point of the polymer has been estimated to between 55 % and 58 % of the final number of DA adducts, the prepolymer is still a viscous liquid. In Chapter 4.5, the prepolymer's initial viscosity at room temperature was estimated to be approximately 200 Pa·s (2080 poise), which is too high for effective integration with the fibers.

Viscosity measurements at elevated temperatures show that rapidly heating the 2MEP4FS prepolymer will lower the viscosity to a few hundred centipoise, an optimal level for fiber integration (Ghezzo et al. 2010). The prepolymer and unidirectional fiber were placed in a nylon film bag, and high vacuum was applied. The bag was briefly placed on a 90 °C steel surface and the prepolymer was manually forced into the fibers. The thin sample was quickly cooled to room temperature, and allowed to continue polymerizing at room temperature.

DSC measurements of 2MEP4FS prepolymer stored at room temperature indicate that after approximately 3-6 hours, the sample's glass transition temperature, T_g, will be above room temperature (Figure 8.5). This allows the nylon film to be easily peeled off,
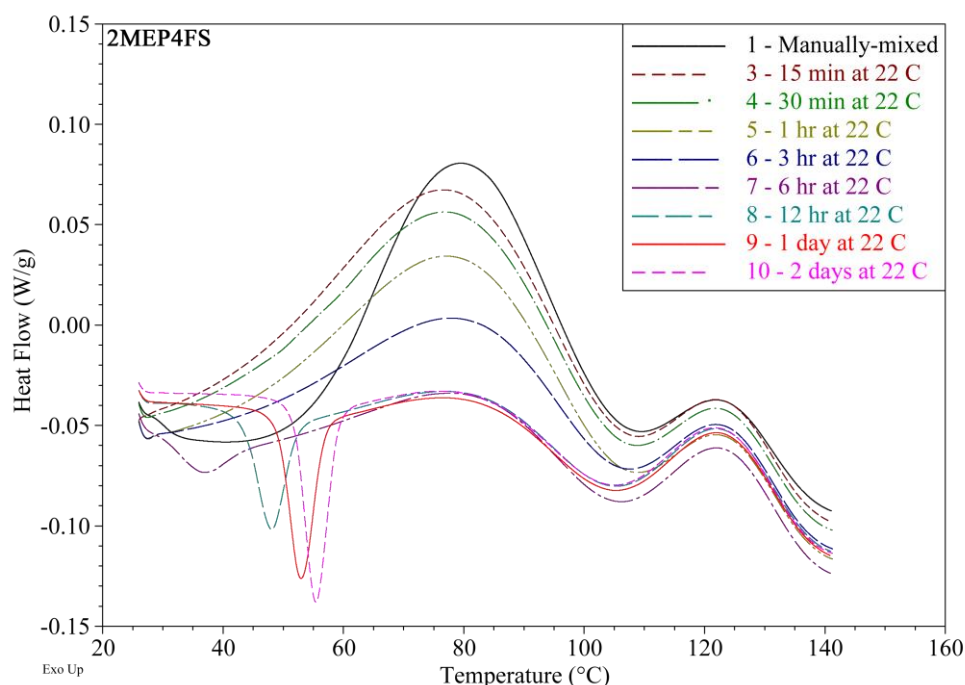
Figure 8.5 DSC results for neat 2MEP4FS prepolymer samples stored at room temperature for different periods of time. The exothermic peak at ~80 °C decreases with time as polymerization proceeds, until the glass transition temperature increases above room temperature.

exposing the prepreg layer for lamination. Increasing the sample's temperature softens the sample, and a DA adduct formation peak is present at 80 °C, even after 2 days at room temperature. This suggests the prepolymer will still flow, allowing prepreg layers to be laminated together.

The nylon films were removed after approximately 6 hours at room temperature and the single prepreg layer was cured in the PTFE mold at 100 °C under light pressure for 15 hours (Figure 8.6). Since the prepolymer was below the T_g before curing, but the level of cross-linking in the sample was still low, it was very brittle when the films were removed, and a few pieces of prepolymer broke off at the edge. During heating and curing in the mold, the remaining prepolymer flowed to fill in these gaps, moving the loose fibers. Regions where the prepolymer had been intact showed no significant fiber movement.

Grinding the neat 2MEP4FS prepolymer into a powder before fiber integration was also explored. The prepolymer was allowed to solidify at room temperature, and then ground into a fine powder using a mortar and pestle. The powder was spread on top

Figure 8.6 A single-layered composite sample with 2MEP4FS polymer and loose T300 carbon fiber prepared by using temperature to control the polymerization rate. (left) The prepreg layer after 24 hours under low vacuum. (right) The same prepreg layer after the application of pressure and heat.

of a layer of loose carbon fibers in the PTFE mold. Approximately 2 MPa of pressure was applied to the piston, and the sample was cured at 120 °C for 2 hours of high vacuum. The powder formed a continuous layer on top of the fibers, but did not appear to penetrate very deeply between filaments. The viscosity of the melting prepolymer particles was likely too high for effective integration.

For effective integration between prepreg layers in a multilayered composite, the prepolymer should be at a low conversion and low viscosity to fill voids and the interlaminar region. Laminating the layers before the T_g of the prepolymer has increased beyond room temperature will reduce the starting conversion. The nylon films can still be removed by briefly cooling them. Increasing the heating rate will reduce the viscosity of the prepolymer. Rapidly heating the PTFE mold will damage it due to temperature gradients and thermal expansion mismatches between the aluminum and PTFE components. The mold was redesigned to use all aluminum parts to address these problems (Figure 8.7). Since aluminum has a much higher thermal conductivity than
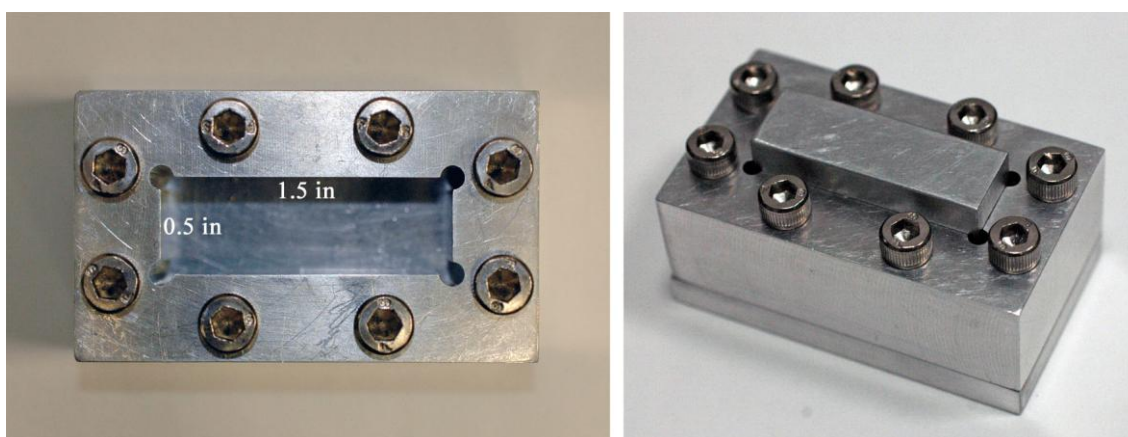
Figure 8.7   An all-aluminum mold designed to apply pressure to prepreg layers. Heat and pressure were applied in a hot press.

PFTE, the composite samples will heat up more quickly. Measurements show a sample reaching 90 % of the preheated press temperature within 100 sec of pressure being applied. Aluminum is also much stiffer than PTFE, enabling the production of samples with more uniform thicknesses. The mold was seasoned with several applications of Slide Universal Mold Release to prevent bonding between the 2MEP4FS polymer and aluminum surfaces. DSC measurements of 2MEP4FS cured on aluminum treated in this manner match measurements of 2MEP4FS cured on PTFE, indicating the mold release does not affect the final sample. The cured 2MEP4FS was removed from the seasoned aluminum as easily as from the PTFE.

Chapter 9

Healable Composites: Characterization and Crack Healing

Fiber-reinforced 2MEP4FS samples prepared using the prepreg technique detailed in Chapter 8.4 were thermally and mechanically characterized.

9.1 Introduction

Fiber-reinforced composite materials are popular in structural applications due to their strength and light weight. They are composed of strengthening fibers embedded in a matrix material that facilitates load sharing. Due to mechanical and thermal property mismatches, composite materials are notoriously susceptible to microcrack damage. Through cyclic loading, these microcracks will grow, coalesce into larger cracks, and ultimately lead to structural failure. Current technology relies on identifying cracks and manual repair or replacement of the composite. If the microcracks could instead be healed before they grow, the useful life of the composite could be extended. This would be particularly useful in foreign environments where human intervention is difficult or impossible.

There are currently two general approaches to creating a composite material that is self-healing or healable via external stimuli. The first approach is to embed liquid healing agent that can bleed out into a crack or other damage and mitigate it. White et al. (2001) incorporated catalyst particles and microcapsules containing a healing agent into a

polymer material which could serve as the matrix in a fibrous composite. Pang and Bond (2005) moved the healing agent out of the matrix and into hollow fibers. In these two approaches, once the healing agent bleeds out into the damaged region and hardens, there is no more available if new damage subsequently forms in the same location. To overcome this limitation, Toohey et al. (2007) investigated using embedded microvascular networks where healing agent can be pumped to the damage site in a biomimetic process. The second approach to creating a healable composite material is through the use of a polymer matrix which can re-form broken cross-linking bonds. This is a fundamentally different process than the flowing of polymer chains to heal damage in a thermoplastic material (Wool and O'Conner 1981). Plaisted and Nemat-Nasser (2007) have demonstrated full recovery of fracture resistance after healing cracks in a neat polymer that uses thermally reversible Diels-Alder (DA) adducts as cross-linking bonds. Plaisted studied 2MEP4FS, a polymer formed from two monomers reacting in a Diels-Alder cycloaddition (Chen et al. 2002; Chen et al. 2003). Since healing was performed at temperatures below where the DA adducts separate, the process requires the crack faces to remain matched and abutted. As the matrix material in a composite, the fibers could help hold the crack surfaces together. These conditions should facilitate healing.

Plaisted (2007) also demonstrated crack healing in 2MEP4FS reinforced with glass fiber and carbon fiber. The composite samples were characterized using single cantilever bending dynamic mechanical analysis. After subsequently subjecting them to cold temperature treatments to introduce microcracks, the samples were recharacterized. They were healed using an elevated temperature thermal treatment and characterized a third time. The composite samples were found to recover a significant portion of the

originally measured stiffness. Park et al. (2009) used a single component, DA-based polymer as the matrix in a carbon fiber composite. The sample was subjected to 3-point bending to measure the stiffness and create cracks. The cracks were healed by using the carbon fiber as an embedded resistive heater. The process was repeated several times and most of the original stiffness was recovered each time.

In studying composite healing, both Plaisted and Park focused on observing changes in mechanical properties after cracking and healing. They did not correlate the number of cracks with the measured mechanical properties. Particularly in Plaisted's study where numerous cracks were present, correlation of the cracks with the measured flexural storage modulus would have been useful in estimating how many cracks were formed and healed by the thermal treatments. A number of analysis techniques have been developed for estimating the mechanical degradation caused by cracks in cross-ply composites like those considered by Plaisted. Broadly termed "finite fracture mechanics" (Hashin 1996), these techniques use each crack as the incremental unit of damage rather than differential crack extension as in classical fracture mechanics. Every new crack is assumed to extend through the ply thickness and be arrested by the boundary conditions without causing failure of the composite. In one dimensional shear lag methods, the load is transferred from a longitudinal ply to a cracked transverse ply by shear stresses which are a function of distance from the crack (Highsmith and Reifsnider 1982; Laws and Dvorak 1988). Two dimensional variational methods for stress analysis have also been developed (Hashin 1986; Nairn and Hu 1992).

In the present work, carbon and glass fiber composites with 2MEP4FS matrices are prepared, characterized, and the mechanical results are compared with simple one-

dimensional analyses. It's found that not only cracks, but also crack healing must be considered to fully explain the experimentally observed behavior.

9.2 Sample Preparation

Composite samples were prepared using a prepreg process to create and laminate multiple layers of unidirectional fiber and 2MEP4FS polymer matrix. Each sample was formed from prepreg layers containing either Toray T300 carbon fiber or AGY S-2 glass fiber. The properties of each composite constituent are given in Table 9.1.

The prepreg process was developed as an extension of the small-sample 2MEP4FS processing method outlined in Chapter 4.2. This method allows small quantities of polymer to be produced with precise monomer ratios and minimal wasted material. The bismaleimide and tetrafuran monomers had been previously been synthesized according to standard procedures (Chen et al. 2003; Weizman et al. 2011). For each composite sample, two prepolymer batches were prepared in parallel to increase

Table 9.1   Composite constituent properties.

	Carbon Fiber [1] $x = f$	Glass Fiber [2] $x = f$	2MEP4FS [3] $x = m$
Mass density, ρ	1.76 g/cm^3	2.488 g/cm^3	1.347 g/cm^3
Longitudinal Young's modulus, E_{xL}	230 GPa	93.8 GPa	3.046 GPa
Transverse Young's modulus, E_{xT}	22 GPa	93.8 GPa	3.046 GPa
Poisson's ratio, ν_x	0.35	0.23	0.367
Shear modulus, G_x	22 GPa	38.1 GPa	1.114 GPa
Longitudinal CTE, α_{xL}	-1.3 μm/m/°C	1.6 μm/m/°C	41 μm/m/°C
Transverse CTE, α_{xT}	7.0 μm/m/°C	1.6 μm/m/°C	41 μm/m/°C

Source: [1]   Kaw (2006)
     [2]   AGY (2006)
     [3]   Chapter 3 and Plaisted (2007)

the quantity of prepolymer. Approximately 600 mg were produced for each composite. A small stoichiometric quantity of monomers were mixed in two glass culture tubes and subjected to high vacuum. The tubes were lowered into a 90 °C oil bath, where the bismaleimide melted and further mixed with the tetrafuran as the polymerization began. The homogenous prepolymers were quenched in liquid nitrogen and returned to room temperature, where they were transferred to a nylon film bag containing a layer of unidirectional fiber. High vacuum was applied to the bag, bringing together the fibers and prepolymer. Still under vacuum, the bag was briefly placed on a steel surface preheated to 90 °C, and the prepolymer was manually forced into the fibers using a brayer. The bag and thin sample were quickly cooled to room temperature and prepreg layers were cut out in the desired orientations.

The prepreg layers were immediately stacked in a [90,0]$_s$ cross-ply sequence. Since intralaminar cracks tend to form parallel with the fiber orientation, the outer 90° plies served to amplify the effect of cracks on bending measurements where the maximum tensile and compressive stresses are at the outer surfaces. The inner 0° plies allowed the samples to retain structural integrity after the formation of cracks in each ply. The stacked layers were placed beneath an aluminum piston in a 0.5 by 1.5 inch opening in an aluminum mold (Figure 8.7). The mold and piston had been lightly seasoned with Slide Universal Mold Release. DSC studies show no effect of the mold release treatment on the thermal properties of cured 2MEP4FS, indicating no solvents or other plasticizers are being introduced. The assembled aluminum mold was placed in a preheated press, and a minimum pressure to ensure good contact was applied to the aluminum piston. A thermocouple placed in the mold near the sample indicated that the sample temperature

varied from 90 to 95 °C during the curing process. The pressure was also monitored, and regularly adjusted as necessary to keep it low, while maintaining contact of the mold with the upper and lower steel platens. After three hours, the press was turned off and the mold and sample were allowed to slowly cool to room temperature over a period of approximately 6 hours. The sample was removed from the mold, cured for an additional 2 hours in a preheated 90 °C oven, and slowly cooled to room temperature again over approximately 10 hours.

The cured composite samples were mounted in a Struers Automated Polishing System and the edges were ground down approximately 0.6 mm to reach the transverse fibers and then polished with successively finer grit sandpapers. Final polishing was performed using a 1 μm alumina slurry. After polishing, the samples were washed with purified water and dried.

9.3   Characterization

The physical, thermal, and mechanical properties of the polished composite samples were measured. The dimensions of each sample were recorded, and the densities determined using the sample masses and volumes of water displaced by the samples. Assuming no voids, the overall fiber volume fraction, V_f, was estimated using the measured sample density, ρ_s, the known densities of the constituent materials, and the rule of mixtures:

$$V_f = \frac{\rho_s - \rho_m}{\rho_f - \rho_m}. \tag{9.1}$$

The carbon fiber and glass fiber composites had similar overall fiber volume fractions: 0.571 and 0.576 respectively.

9.3.1 Microscopy

The composite samples were inspected and photographed using a Nikon Epiphot inverted metallograph. There were a minimal number of voids, mostly near the outer, unpolished surfaces. Cracks were observed in both samples before any mechanical experiments were performed (Figure 9.1). These cracks likely formed during cooling due to differences in thermal expansion coefficients between the plies and between the constituents. The cracks were mostly closed, appearing as fine lines in the images. Only a few were found by inspecting microscopy images. The semi-transparent glass fiber sample was also imaged through-thickness at a high resolution (Figure 9.2). Striations in the longitudinal and transverse directions indicate the presence of numerous cracks. The carbon fiber sample was opaque, so a similar characterization was not possible.
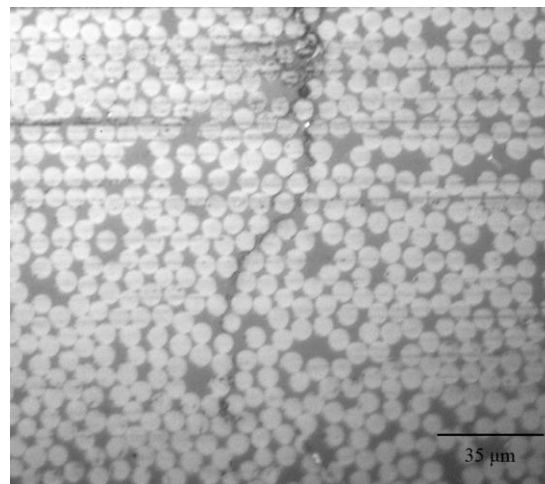
Figure 9.1   Optical microscope image of a transverse ply crack in the carbon fiber composite sample. The crack runs from the top center to the bottom of the image.
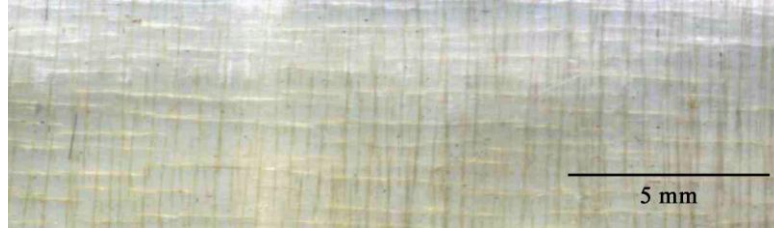
Figure 9.2 Through-thickness view of the glass fiber composite sample. The longitudinal plies are oriented left-right in the image.

The average transverse and longitudinal ply thicknesses were estimated from metallograph images. In both samples, the longitudinal plies were observed to be thinner than the transverse plies. Since the longitudinal and transverse prepreg layers were prepared together, they are assumed to have similar initial thicknesses. The discrepancy may be the result of the prepolymer more easily flowing along the fiber direction when pressure was applied, or the prepolymer being drawn to the hot aluminum mold surfaces at the top and bottom of the sample during the initial, low viscosity stage of curing. Since the fiber quantity in each ply should be constant given the unidirectional fiber tape used, the thickness of the layers must be considered in determining the fiber volume fraction of each layer. The estimates made using mass density can be separated into longitudinal fiber volume fraction, V_{Lf}, and transverse fiber volume fraction, V_{Tf}:

$$V_{Lf} = V_f \frac{2(t_L + t_T)}{4t_L}, \tag{9.2a}$$

$$V_{Tf} = V_f \frac{2(t_L + t_T)}{4t_T}, \tag{9.2b}$$

where t_L and t_T are the average thicknesses of the longitudinal and transverse plies. The updated fiber volume fraction estimates are given in Table 9.2. Fiber volume fractions in the transverse plies were also estimated from photographs. The results are reasonably

close to the fiber volume fraction estimates derived from the density method, varying by a few percent. These measurements were made from only a few photographs and voids were not considered.

9.3.2 Differential Scanning Calorimetry

Thermal measurements were made using a TA Instruments 2920 Differential Scanning Calorimeter (DSC) configured with a liquid nitrogen cooling accessory and 50 mL/min dry nitrogen purge gas. A corner of each composite sample was cut off, individually sealed in a hermetic aluminum pan, and heated at 3 °C/min with ±1 °C/min sinusoidal modulation from 0 °C through the glass transition temperature, T_g, taken here as the inflection of the reversible part of the measured heat flow (TA Instruments 1998). The glass transition temperatures of the carbon fiber and glass fiber composites were 94.7 °C and 100.8 °C respectively. Applying the previously determined model for 2MEP4FS cross-linking as a function of T_g, equation (4.3), gives conversions of 0.956 and 0.998. The relatively low final conversion of the carbon fiber composite may be due to the increased surface area of the smaller diameter carbon fibers and more sizing transferring into the polymer and acting as a plasticizer. Nearly ideal results for the glass fiber composite indicate that the sparse fill threads holding the fibers together did not affect the final polymer matrix. Plaisted (2007) also noted inconsistent DSC thermal results from his carbon fiber composite. Here, the change is deemed small and ignored for the purposes of analysis.

9.3.3 Dynamic Mechanical Analysis

Mechanical measurements were made using a TA Instruments 2980 Dynamic Mechanical Analyzer (DMA). The composite samples were tested in the single cantilever bending configuration, where both ends are fixed against rotation and one end of the sample is moved up and down (Figure 9.3). Each sample was mounted in the rear position of the dual cantilever bending clamp (Figure 3.9), and the clamp screws were tightened with 8 in·lbf of torque. The instrument's thermocouples were positioned near the sample for temperature measurements. A multi-frequency scan of 0.1, 1, 2, 5, 10, and 20 Hz was performed with a displacement amplitude of ±10 μm. In this mode of operation, the instrument uses the prescribed displacement amplitude and the measured force and time lag between signals to determine the storage modulus, E', and loss modulus, E'', of the sample. The DMA calculates the storage modulus of the sample using one dimensional Euler-Bernoulli beam theory with additional non-dimensional terms to account for imperfect fixation at the grips and shear deformation (TA Instruments 2002):

$$E' = \frac{PL^3}{12Id}\frac{1}{F_c}\left[1 + \frac{12}{5}(1 + v)\left(\frac{t}{L}\right)^2\right] \tag{9.3}$$
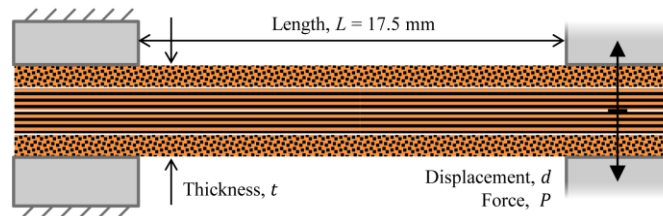
Figure 9.3 Diagram of single cantilever bending DMA measurements made on the composite samples.

where d is the prescribed displacement, P is the measured force, I is the second moment of area, and F_c is a clamping correction factor.

The scan was performed eight times, with the sample removed and remounted in a different orientation each time. The measurements were made at room temperature with the furnace open. This method was verified using a single cantilever polycarbonate standard sample provided by TA Instruments. The results of a single frequency measurement at room temperature with the furnace open match the reference data provided by TA Instruments. The average storage and loss moduli for the 2MEP4FS composite samples are given in Figure 9.4.

After multi-frequency testing, the samples were remounted a final time in the DMA and scanned with the furnace closed at 1 Hz from 20 °C to 130 °C at 3 °C/min. The resulting storage moduli and $\tan \delta$ are given in Figure 9.5. Both samples show an initial decrease, then increase, peak, and strong decrease in storage moduli as the temperature increases. This behavior was unexpected as the 2MEP4FS matrix only exhibited a decreasing modulus with temperature when tested alone. The mechanical properties of the fibers were not expected to vary significantly over this temperature range. These results are explored and explained in the following analyses.
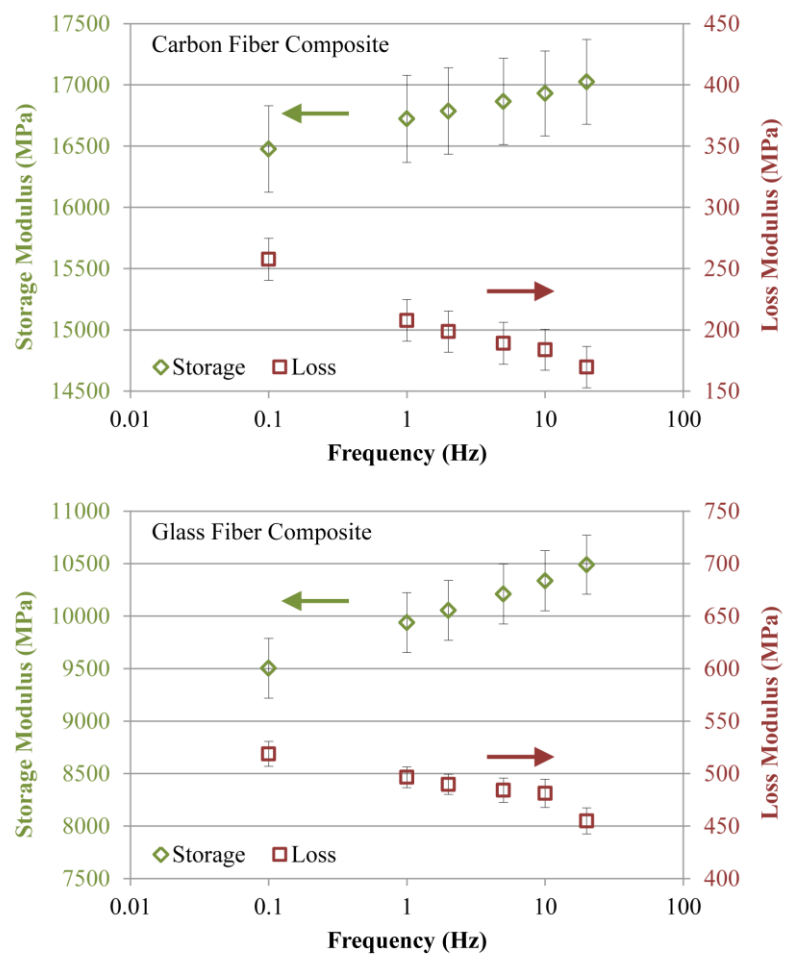
Figure 9.4   Room temperature DMA results for the carbon and glass fiber composites as a function of frequency.
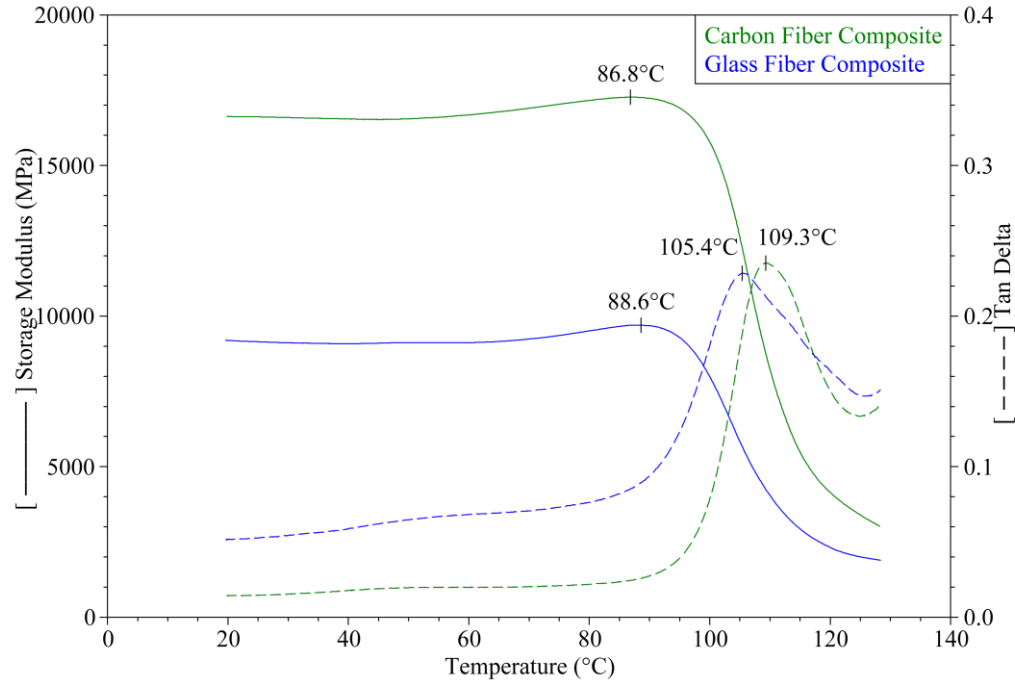
Figure 9.5 Single frequency (1 Hz) DMA results for the carbon and glass fiber composites as a function of temperature.

9.4 Analysis

The composites were analyzed using simple one dimensional approximations for comparison with the one dimensional DMA experimental results. Below the glass transition temperature, T_g, the loss moduli of the samples were found to be minimal compared with the storage moduli; i.e. $\tan \delta$ was small. The sample was treated as linear elastic and the storage modulus was taken as Young's modulus for the purpose of calculations. The fibers and matrix were homogenized to form a single material with effective properties for the transverse and longitudinal directions of each ply. The samples are first treated as fully intact, the ideal case. The effect of transverse cracks is subsequently considered using a shear lag model, and the effective tensile moduli of the

damaged transverse plies are estimated as a function of crack density. Crack healing is finally included as a linear function of temperature. The effective properties of the transverse and longitudinal plies are homogenized to form a single beam with effective properties. This beam is considered as an Euler-Bernoulli beam in bending with small displacements. The results of the homogenization estimates and DMA measurements are compared.

9.4.1 Ideal, Intact Composites

As a first approximation, the composite samples were treated as fully intact with no cracks affecting the mechanical properties. Using the constituent properties (Table 9.1), fiber volume fractions, and sample dimensions, the fibers and matrix of each ply were homogenized using standard strength of materials methods to obtain effective properties (Kaw 2006). The sample geometry and a representative volume element are depicted in Figure 9.6. In the following notation, the first subscript refers to the ply (T,
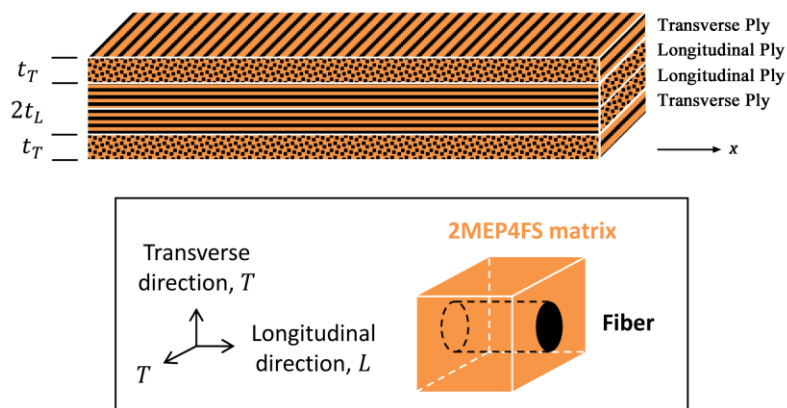
Figure 9.6 The layup of each composite and a representative volume element of the fiber and matrix.

L) or constituent (f, m) and the second subscript denotes the direction (T, L) or constituent (f, m).

The effective Young's modulus in the longitudinal direction of each ply is determined using the Voigt model, where the strain of each constituent is assumed constant and the overall stiffness is given by the rule of mixtures:

$$E_{LL} = V_{Lf} E_{fL} + \left(1 - V_{Lf}\right) E_{mL}, \tag{9.4a}$$

$$E_{TL} = V_{Lf} E_{fL} + \left(1 - V_{Tf}\right) E_{mL}. \tag{9.4b}$$

Conversely, the effective Young's modulus in the transverse direction of each ply is determined using the Reuss model, where the stress in each constituent is assumed constant and the overall compliance is given by the rule of mixtures:

$$\frac{1}{E_{LT}} = \frac{V_{Lf}}{E_{fT}} + \frac{1 - V_{Lf}}{E_{mT}}, \tag{9.5a}$$

$$\frac{1}{E_{TT}} = \frac{V_{Tf}}{E_{fT}} + \frac{1 - V_{Tf}}{E_{mT}}. \tag{9.5b}$$

The effective Poisson's ratio of each ply in the plane of bending is determined using the rule of mixtures:

$$\nu_{LT} = V_{Lf} \nu_f + \left(1 - V_{Lf}\right) \nu_m, \tag{9.6a}$$

$$\nu_{TT} = V_{Tf} \nu_f + \left(1 - V_{Tf}\right) \nu_m. \tag{9.6b}$$

The effective shear modulus of the longitudinal plies is determined from the rule of mixtures for the shear compliance, while the effective shear modulus of the transverse plies is estimated from a simple isotropic assumption:

$$G_{LT} = \left(\frac{V_{Lf}}{G_f} + \frac{1 - V_{Lf}}{G_m}\right)^{-1} \tag{9.7a}$$

$$G_{TT} = \frac{E_{TT}}{2(1 + \nu_{TT})}, \tag{9.7b}$$

The calculated mechanical properties for each composite are given in Table 9.2.

Given the fiber-matrix geometry of the transverse direction of the transverse plies, equations (9.6b) and (9.7b) are generally not appropriate estimates of effective properties. Micromechanics methods given by Nemat-Nasser and Hori (1999) are better approximations. The self-consistent method for a random distribution of aligned reinforcing microfibers includes interaction between the fibers. Using this method, the effective transverse ply Poisson's ratio, ν_{TT}, can be extracted from the overall bulk modulus, and the effective shear modulus, G_{TT}, can be determined. The micromechanics method estimates the transverse shear moduli of both samples to be on the order of 2 GPa, which is comparable to the estimates given by equation (9.7b). The shear modulus controls the number of estimated cracks in later calculations.

Table 9.2   Homogenized lamina properties.

		Carbon Fiber Composite	Glass Fiber Composite
Longitudinal Ply	Thickness, t_L	0.165 mm	0.153 mm
	Fiber volume fraction, V_{Lf}	0.623	0.623
	Longitudinal Young's modulus, E_{LL}	144 GPa	59.6 GPa
	Transverse Young's modulus, E_{LT}	6.58 GPa	7.67 GPa
	LT-plane Poisson's ratio, ν_{LT}	0.325	0.282
	LT-plane shear modulus, G_{LT}	2.73 GPa	2.82 GPa
	Longitudinal CTE, α_{LL}	-0.96 μm/m/°C	2.36 μm/m/°C
	Transverse CTE, α_{LT}	41.1 μm/m/°C	35.3 μm/m/°C
Transverse Ply	Thickness, t_T	0.196 mm	0.178 mm
	Fiber volume fraction, V_{Tf}	0.527	0.536
	Longitudinal Young's modulus, E_{TL}	123 GPa	51.6 GPa
	Transverse Young's modulus, E_{TT}	5.58 GPa	6.32 GPa
	TT-plane Poisson's ratio, ν_{TT}	0.358	0.294
	TT-plane shear modulus, G_{TT}	2.05 GPa	2.44 GPa
	Longitudinal CTE, α_{TL}	-0.68 μm/m/°C	2.32 μm/m/°C
	Transverse CTE, α_{TT}	34.7 μm/m/°C	30.3 μm/m/°C

The homogenized layers were considered as plies in a rectangular $[90,0]_s$ composite beam subjected to bending (Figure 9.3). The samples are thin and the experimental displacements were small relative to the sample length, so one dimensional Euler-Bernoulli beam theory applies. The neutral axis, $\bar{y}$, of the beam is located where the axial force due to bending is zero:

$$\int_T \sigma_{TL}(y)dA + \int_L \sigma_{LL}(y)dA = 0, \tag{9.8}$$

where A is the cross-sectional area of the beam. Since the ideal, intact beam is symmetric both in geometry and material properties, the neutral axis will be at the center of the beam:

$$\bar{y} = t_L + t_T. \tag{9.9}$$

The moment-curvature relationship is:

$$E_{flex}I\kappa = \int_T \sigma_{TL}(y)ydA + \int_L \sigma_{LL}(y)ydA, \tag{9.10}$$

where κ is the curvature, which is approximated as constant through the thickness of the beam. The overall flexural modulus of the intact beam is found to be:

$$E_{flex} = \frac{8E_{TT}t_T\left(3t_L^2 + 3t_Lt_T + t_T^2\right) + 8E_{LL}t_L^3}{(t_L+t_T)^3}. \tag{9.11}$$

The Euler-Bernoulli flexural moduli were compared with estimates given by laminated plate theory and found to be in very good agreement (< 0.5 % difference).

The calculated flexural moduli were compared with the DMA storage moduli measured at 1 Hz at room temperature. Although the calculations are for static cases, the 2MEP4FS moduli were determined using DMA at 1 Hz. Assuming the carbon and glass fiber moduli are independent of frequency, the comparison is appropriate. The carbon fiber composite sample was predicted to have a modulus 14 % higher than measured, and

the glass fiber composite sample was predicted to have a modulus 26 % higher than measured. In the literature, it has been noted that unidirectional fiber that has been sitting out at atmospheric conditions for extended periods of time will yield composites with poor bonding between the fibers and matrix, likely due to moisture accumulation at the fiber surface (Sjögren and Berglund 2000). To rule out interfacial problems, new unidirectional S-2 glass fiber tape was purchased and stored under high vacuum. This fiber was used to produce a third composite sample, which was prepared and characterized in a similar manner. The DMA single cantilever bending results show a comparable reduction in stiffness relative to the calculated properties, suggesting moisture at the interface is not a concern.

The calculated flexural moduli and measured DMA storage moduli for the composite samples were also compared as a function of temperature. The storage modulus of neat 2MEP4FS has previously been characterized at 1 Hz as a function of temperature, from 20 °C to 130 °C at 3 °C/min (Figure 3.11). These experimental parameters were the same for the composite DMA measurements. Assuming changes in fiber properties as a function of temperature are minimal, the ply and beam properties, equations (9.4a), (9.5b), and (9.11), are evaluated as a function of temperature. Comparing the calculated and measured moduli, the values are initially poor, but converge between 90 °C and 100 °C (Figure 9.11). Beyond the glass transition temperature, the calculations and experiments can no longer be meaningfully compared. At the T_g of 2MEP4FS, the storage modulus precipitously drops and $\tan \delta$ sharply increases, precluding further consideration of the polymer as a linear elastic material. Softening of the polymer and composite samples also leads to viscous deformation in the

gripped regions. Since the experiment is sensitive to sample thickness, this deformation quickly skews the measured flexural moduli.

9.4.2 Composites with Cracks

The discrepancy between the calculated flexural moduli for the ideal, intact case and the measured storage moduli at room temperature may be attributed to the presence of cracks in the composite plies. Cracks were seen in microscopy images of the transverse plies in both the glass fiber and carbon fiber composite samples. The transverse plies are the furthest from the neutral axis and the cracks are oriented along the fiber direction, normal to the plane of bending, meaning the observed damage would have a significant effect on the DMA measurements.

Since the cracks were observed before any mechanical measurements had been performed, the damage must have occurred during sample preparation. The samples were gently removed from the aluminum mold and tightly clamped with only the edges exposed during grinding and polishing, so crack formation during these steps is unlikely. The samples had been cured at a maximum temperature of 95 °C and then cooled to room temperature for characterization. Residual thermal stresses due to differences in the coefficient of thermal expansion (CTE), α, between the constituents and between the cross-oriented plies could be the source of the observed cracks. Specifically, the CTE of 2MEP4FS is an order of magnitude higher than both the carbon and glass fibers (Table 9.1). An effective CTE for each ply was determined following similar strength of materials homogenization methods as previously employed (Kaw 2006). The longitudinal CTE for each ply is:

$$\alpha_{LL} = V_{Lf}\left(\frac{\alpha_{fL}E_{fL}}{E_{LL}}\right) + (1 - V_{Lf})\left(\frac{\alpha_{mL}E_{mL}}{E_{LL}}\right), \tag{9.12a}$$

$$\alpha_{TL} = V_{Lf}\left(\frac{\alpha_{fL}E_{fL}}{E_{TL}}\right) + (1 - V_{Lf})\left(\frac{\alpha_{mL}E_{mL}}{E_{TL}}\right). \tag{9.12b}$$

The transverse CTE for each ply is:

$$\alpha_{LT} = V_{Lf}[\alpha_{fL} - v_f(\alpha_{LL} - \alpha_{fL})] + (1 - V_{Lf})[\alpha_{mL} - v_m(\alpha_{mL} - \alpha_{LL})], \tag{9.13a}$$

$$\alpha_{TT} = V_{Tf}[\alpha_{fT} - v_f(\alpha_{TL} - \alpha_{fT})] + (1 - V_{Tf})[\alpha_{mT} - v_m(\alpha_{mT} - \alpha_{TL})]. \tag{9.13b}$$

The calculated CTEs for each composite ply are given in Table 9.2. The resulting residual stresses in the transverse ply of each composite are estimated by balancing the forces and strains between the cross-plies:

$$t_L\sigma_{Lr} + t_T\sigma_{Tr} = 0, \tag{9.14}$$

$$\alpha_{LL}\Delta T + \epsilon_{Lr} = \alpha_{TT}\Delta T + \epsilon_{Tr}, \tag{9.15}$$

where ΔT=-75 °C is the change in temperature experienced by the sample after curing. Assuming each composite is still intact and a linear stress-strain relationship, the residual thermal stress in the transverse ply is:

$$\sigma_{Tr} = \frac{E_{TT}\Delta T(\alpha_{LL}-\alpha_{TT})}{1+E_{TT}t_T/E_{LL}t_L}. \tag{9.16}$$

The carbon and glass fiber composites are estimated to have residual, transverse ply stresses of 14.25 MPa and 11.80 MPa respectively. This level of stress is comparable to the axial stresses used to drive cracks in neat 2MEP4FS during the DCDC fracture test (see Chapter 7.2 and Plaisted and Nemat-Nasser 2007). At short crack lengths in the DCDC geometry, the tensile opening stress is approximately equal to the axial stress (Plaisted et al. 2006). Stress concentrations and interfaces created by the fibers are also expected to facilitate crack formation and propagation in the composite samples.

During mechanical characterization, tensile stresses due to bending may also generate cracks in the transverse plies. The maximum stress during single cantilever bending is expected near the grips and is estimated to be (TA Instruments 2002):

$$\sigma_{TT\_max} = \frac{6d(t_L+t_T)F_cE_{TT}}{L^2\left[1+\frac{48}{5}(1+\nu)\left(\frac{t_L+t_T}{L}\right)^2\right]}.$$
(9.17)

Assuming intact lamina, DMA characterizations of the carbon and glass fiber composites are estimated to create maximum stresses of 1.15 MPa and 1.20 MPa respectively. Although these applied tensile stresses are in addition to the residual thermal stresses, they are significantly smaller in magnitude. Nairn and Hu (1992) notes that that progressive tensile loading of [90,0]$_s$ composites will lead to the generation of fewer and fewer new cracks until a saturation crack density is reached. This observation suggests the marginal increase in transverse ply tensile stresses due to bending will create relatively few cracks compared with the initial residual thermal stresses due to CTE mismatches.

The effect of cracks on the mechanical properties of the composite samples was estimated using a shear lag model given by Lee and Daniel (1990). The model was developed for [0,90]$_s$ composites loaded in tension and is adapted here for application to [90,0]$_s$ composites subjected to bending. Others have successfully used shear lag models derived for tensile loading to estimate the mechanical properties of cross-ply composites in bending (Smith and Ogin 1999, 2000). Here, the transverse ply cracks are assumed to be symmetric between the top and bottom layers (Figure 9.7). Longitudinal ply cracks are neglected as they will have minimal effect on the bending measurements due to their orientation.
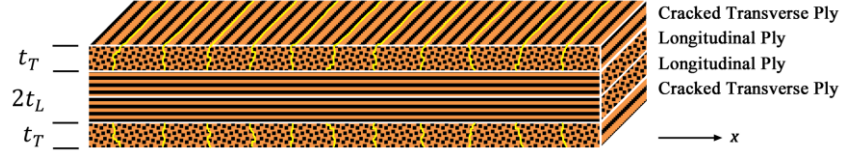
Figure 9.7 The cracks in the transverse plies are assumed periodic and symmetric. Cracks in the longitudinal plies are not considered.

The one-dimensional shear lag method for cross-ply composites assumes load is transferred from intact longitudinal plies to cracked transverse plies by shear stresses. The interfacial shear stress, τ_i, is considered proportional to the difference in average x-displacements between cross-plies ($\bar{u}_L$, $\bar{u}_T$):

$$\tau_i(x) = H[\bar{u}_T(x) - \bar{u}_L(x)],\tag{9.18}$$

where H is a shear lag parameter to be determined later. For a linear relationship between stress and strain and periodically spaced cracks, a normal stress distribution in each ply can be determined. The tensile stress between two cracks in a damaged transverse ply is:

$$\sigma_{TT}^*(x) = \left(\frac{E_{TT}(t_L+t_T)}{E_{LL}t_L+E_{TT}t_T}\sigma_a + \sigma_{Tr}\right)\left(1 - \frac{cosh(\alpha S-\alpha x)}{cosh(\alpha S)}\right),\tag{9.19}$$

where σ_a is the applied stress, S is one half of the crack spacing, and:

$$\alpha^2 = H\left(\frac{1}{t_L E_{LL}} + \frac{1}{t_T E_{TT}}\right).\tag{9.20}$$

Neglecting the contribution of the transverse ply and assuming the average strain of the longitudinal plies is equal to the average strain of the entire composite, the average normal stress of the cracked transverse ply corresponds to an effective Young's modulus:

$$E_{TT}^* = \left(\frac{\alpha S - tanh(\alpha S)}{\alpha S + \frac{t_T E_{TT}}{t_L E_{LL}}tanh(\alpha S)}\right)E_{TT}.\tag{9.21}$$

Details of the calculations are given by Lee and Daniel (1990). The effective moduli of the damaged transverse plies are deetermined as a function of crack density in Figure 9.8.

To determine the shear lag parameter, H, for a composite subjected to bending, a parabolic variation in the shear stress distribution is assumed for each ply. For cubic variations of ply x-displacements through the thickness (y-direction):

$$u_L(x,y) = A_1(x)y^3 + A_2(x)y^2 + A_3(x)y + A_4(x), \qquad (9.22a)$$

$$u_T(x,y) = B_1(x)y^3 + B_2(x)y^2 + B_3(x)y + B_4(x), \qquad (9.22b)$$

the shear stresses can be approximated as:

$$\tau_L(x,y) = G_{LT}\frac{du_L(x,y)}{dy} = G_{LT}[3A_1(x)y^2 + 2A_2(x)y + A_3(x)], \qquad (9.23a)$$

$$\tau_T(x,y) = G_{TT}\frac{du_T(x,y)}{dy} = G_{TT}[3B_1(x)y^2 + 2B_2(x)y + B_3(x)]. \qquad (9.23b)$$
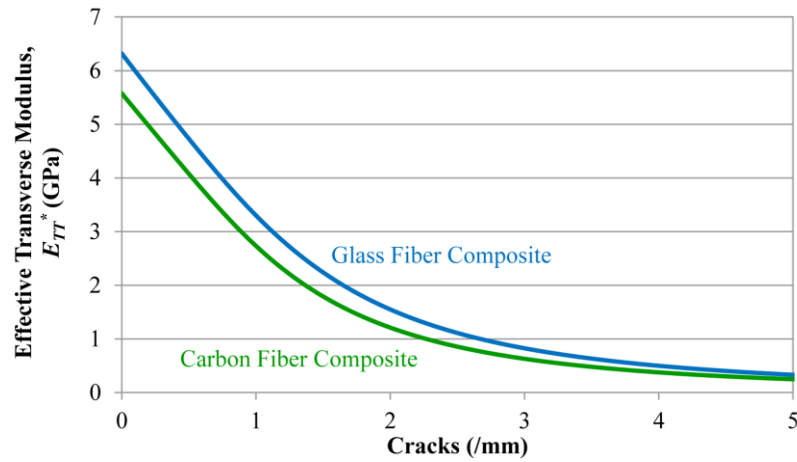
Figure 9.8 Effective tensile Young's moduli of the cracked transverse plies.

The boundary and continuity conditions are:

$$\tau_L(x, y = 0) = 0, \tag{9.24a}$$

$$u_L(x, y = t_L) = u_T(x, y = t_L), \tag{9.24b}$$

$$\tau_L(x, y = t_L) = \tau_T(x, y = t_L) = \tau_i(x), \tag{9.24c}$$

$$\frac{d\tau_L}{dy}(x, y = t_L) = 0, \tag{9.24d}$$

$$\frac{d\tau_T}{dy}(x, y = t_L) = 0, \tag{9.24e}$$

$$\tau_T(x, y = t_L + t_T) = 0. \tag{9.24f}$$

Averaging the displacements through the thickness and rearranging equation (9.18) gives the shear lag parameter:

$$H = \frac{12G_{LT}G_{TT}}{5(G_{LT}t_T + G_{TT}t_L)}. \tag{9.25}$$

The geometry and material properties are considered symmetric in this derivation of the shear lag parameter. Specifically, the boundary conditions suggest the cracks are open and must not close so the transverse laminate behaves similarly in compression as in tension. But microscopy observations indicate the cracks are mostly closed, and closed cracks are assumed in later beam bending analyses. A finite element simulation was used to verify the applicability of the determined shear lag parameter to the single cantilever bending of the carbon fiber composite sample with four closed cracks: one in each transverse ply at each DMA grip. Due to the symmetry of the single cantilever experiment, one half of the sample was modeled (Figure 9.9) using 8112 plane strain shell elements and orthotropic material models with the previously determined effective properties (Table 9.2). At the fixed end, the longitudinal plies and transverse ply subjected to compression were fixed against x-displacement and in-plane rotation. The
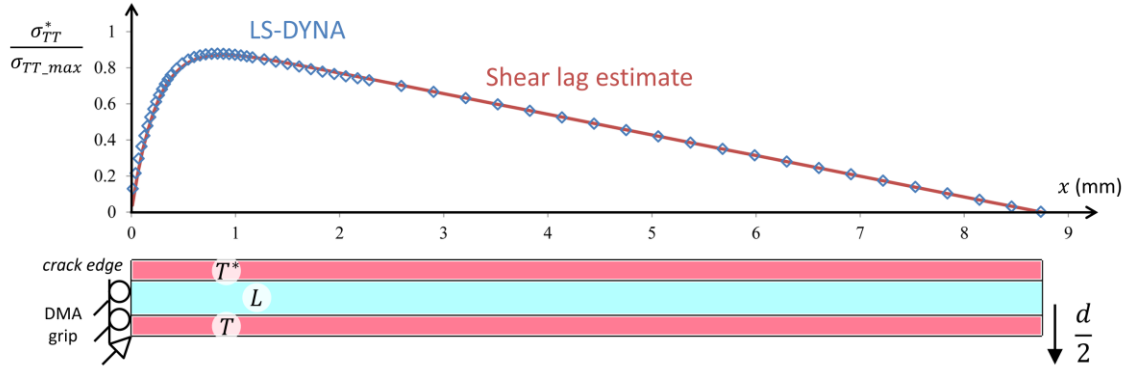
Figure 9.9 One-half of the single cantilever DMA test on the carbon fiber composite was simulated using LS-DYNA. The average stress through the thickness of the cracked transverse ply (T^*) was compared with the stress predicted by the shear lag model.

edge of the transverse ply subjected to tension was left free as a crack surface. At the opposite end of the sample, a periodic boundary condition was applied to all four layers and a uniform bending displacement $d/2$ was applied. The tensile transverse ply stress was averaged through the thickness of the ply at several locations and compared with the predicted stress distribution given by equation (9.19) (Figure 9.9). The correlation between the theoretical model and the finite element simulation is judged to be very good, indicating the shear lag parameter can be applied to analyses with closed cracks.

The effective properties of the damaged transverse plies are incorporated into the beam calculations. Assuming closed cracks, equation (9.8) is re-evaluated to find the neutral axis:

$$\bar{y} = \frac{4E_{LL}t_L(t_L+t_T)+t_T(4E_{TT}^*t_L+E_Tt_T+3E_{TT}^*t_T)}{4E_{LL}t_L+2t_T(E_{TT}+E_{TT}^*)}, \tag{9.26}$$

and equation (9.10) is re-evaluated to find the overall flexural modulus:

$$E_{flex} = \frac{C_1+C_2+C_3}{16(t_L+t_T)^6}, \tag{9.27a}$$

where:

$$C_1 = 2E_{LL}t_L(4t_L^2 + 6t_L(t_T - \bar{y}) + 3(t_T - \bar{y})^2), \qquad (9.27b)$$

$$C_2 = E_{TT}t_T(t_T^2 - 3t_T\bar{y} + 3\bar{y}^2), \qquad (9.27c)$$

$$C_3 = E_{TT}^*t_T(12t_L^2 + 18t_Lt_T + 7t_T^2 - 12t_L\bar{y} - 9t_T\bar{y} + 3\bar{y}^2). \qquad (9.27d)$$

The crack spacing parameter S is selected for each composite analysis such that the calculated flexural moduli matches the DMA measurements at room temperature. This fitting method gives crack densities of 3.21 cracks/mm and 2.23 cracks/mm for the carbon and glass fiber composites respectively. The calculations were also carried out as a function of temperature. Initially, the slow decline in the measured storage modulus is well predicted, but the experimental data eventually diverges, resulting in poor agreement at higher temperatures (Figure 9.11).

The estimated crack density for the glass fiber composite sample can be correlated with microscopy observations. Counting the number of transverse cracks in the through-thickness image (Figure 9.2) gives approximately 3.66 cracks/mm. Since longitudinal cracks are also apparent in the images, the observed transverse cracks may be from both transverse plies. Although the shear lag stress distribution assumes symmetric cracks, other researchers have noted that, in practice, transverse cracks in [90,0]$_s$ cross-ply composites tend to form in a staggered manner (Nairn and Hu 1992). Assuming every crack is indeed staggered and visible, there are an estimated 1.83 cracks/mm in each 90° glass ply. The estimate of 2.23 cracks/mm is very reasonable given that not every crack may have been visible. The cracks are not ideally periodic, and will tend to form at defects, which may lead to some being symmetric and therefore obscured from view. The observed number of cracks also does not include any cracks formed during DMA

testing. Previous discussion has estimated the number of additional cracks to be minimal. DMA measurements were observed to be reasonably consistent over all tests. Since the carbon fiber sample is not transparent, a similar correlation between analysis results and observations could not be made.

9.4.3   Composites with Cracks that Heal

The cracked composite approximation shows good agreement with the DMA measurements at low temperatures, while the ideal, intact composite approximation shows good agreement at high temperatures. This suggests the damage is being mitigated as the sample temperature is increased. One possibility is the cracks are slightly open at room temperature and progressively close without healing as the sample is heated and residual thermal strains are relieved. But crack closing would not increase the tensile modulus of the transverse plies, limiting the recovered bending stiffness of the composite. Additionally, the DMA measurements indicate the storage modulus doesn't immediately begin to diverge from the cracked assumption as would be expected if the cracks were closing. For these reasons and given the previously establishing healing capability of neat 2MEP4FS (Chapter 7.2; Plaisted and Nemat-Nasser 2007), the cracks are assumed to heal during the DMA temperature ramp experiments.

For healing to occur, the crack faces must directly abut, which will most truly occur near the crack tips. The crack tips in the 90° transverse plies are generally located near the longitudinal 0° plies where the cracks were arrested. It is expected that the cracks will first heal near this interface, and, as the temperature increases and thermal strain decreases, the cracks will continue to heal and the crack tips will retreat toward the

free surface. As simple model for this assumed behavior, the transverse plies are separated into two layers: a healed layer with ideal properties and a cracked layer with the reduced modulus in tension (Figure 9.10). The thickness of each layer depends on the temperature, T, and the total ply thickness remains constant:

$$t_T = t_T^*(T) + t_{Th}(T). \tag{9.28}$$

Since the CTE of 2MEP4FS is approximately constant over the tested temperature range (Plaisted 2007), the thickness of the healed layer, t_{Th}, is assumed to be a linear function of temperature. DSC measurements of 2MEP4FS with separated DA adducts show the adducts will begin to re-establish at ~48 °C (Figure 3.8). The DSC measurements were made at the same average heating rate (3 °C/min) as was used for the DMA mechanical measurements. This temperature agrees with the observed onset of divergence between the DMA experimental results and the cracked composite calculations. During curing, the maximum temperature experienced by the samples was approximately 95 °C. This temperature is taken as the stress-free temperature for the composite, and the cracks are assumed to be fully healed. This is also the temperature Plaisted (2007) used to finalize crack healing in neat 2MEP4FS and composite samples. The thickness of the healed transverse layer is then:

Figure 9.10 The cracks in the transverse plies are assumed to heal. The transverse plies are subdivided into a healed layer and cracked layer. The thickness of each layer is assumed to be linearly related to the sample temperature.

$$t_{Th} = \begin{cases} 0 & T < 48\ °C \\ \frac{T-48}{95-48} t_T & 48\ °C \le T \le 95\ °C \\ t_T & T > 95\ °C \end{cases} \tag{9.29}$$

The crack healing assumptions are used to calculate the composite beam properties as a function of temperature. For closed cracks, equation (9.8) gives the neutral axis as:

$$\bar{y}(T) = \frac{4E_{LL}t_L(t_L+t_T)+E_{TT}^*t_T^*(4t_L+4t_{Th}+3t_T^*)+E_{TT}\left(4t_Lt_{Th}+(2t_{Th}+t_T^*)^2\right)}{4E_{LL}t_L+2E_{TT}\left(2t_{Th}+t_T^*\right)+2E_{TT}^*t_T^*}. \tag{9.30}$$

and equation (9.10) gives the overall flexural modulus as:

$$E_{flex}(T) = \frac{D_1+D_2+D_3}{16(t_L+t_T)^6}. \tag{9.31a}$$

where,

$$D_1 = E_{LL}((2t_L+t_T-\bar{y})^3 - (t_T-\bar{y})^3), \tag{9.31b}$$

$$D_2 = E_{TT}((2t_L+2t_{Th}+t_T^*-\bar{y})^3 - (2t_L+t_T-\bar{y})^3 + (t_T-\bar{y})^3 + \bar{y}^3), \tag{9.31c}$$

$$D_3 = E_{TT}^*((2t_L+2t_T-\bar{y})^3 - (2t_L+2t_{Th}+t_T^*-\bar{y})^3), \tag{9.31d}$$

The temperature dependent flexural modulus, equation (9.31), is compared with the DMA measurements in Figure 9.11, and the correlation is deemed excellent over the entire temperature range. Small deviations in the glass fiber composite results could be attributed to inconsistent crack paths. The cracks observed by microscopy were generally more torturous in the glass fiber sample than the carbon fiber sample, with more branching and more variation in the x-direction. This may be due to differences in filament size (10 µm glass diameter (AGY 2006), 7 µm carbon diameter (Toray Carbon Fibers America Inc 2012)) and interfacial shear strength.
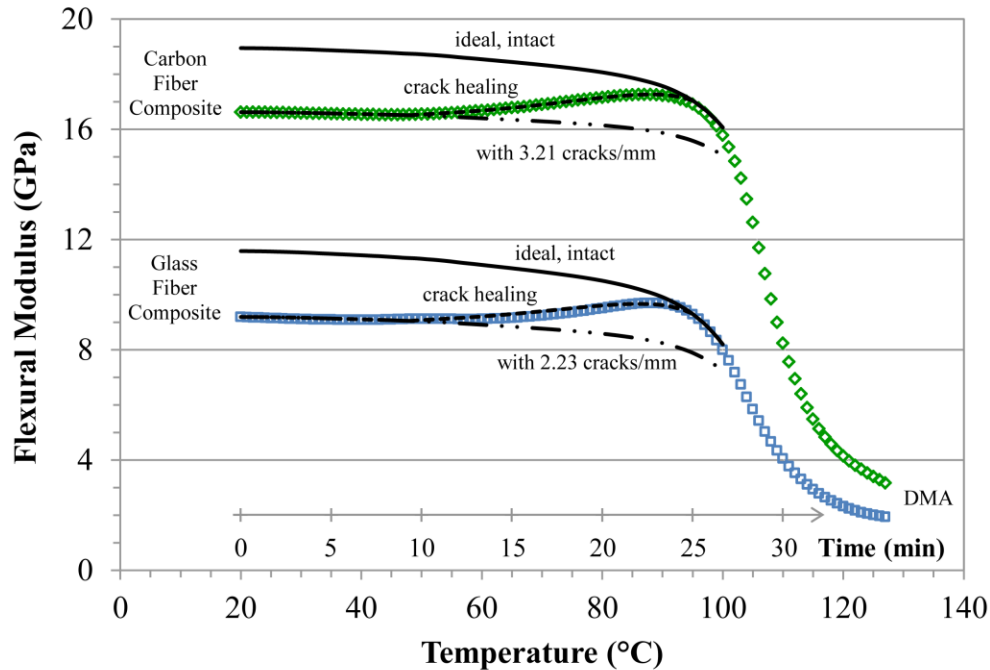
Figure 9.11 The various composite analyses compared with the DMA experimental measurements.

9.5 Discussion

Carbon and glass fiber cross-ply composites were characterized, and analytical approximations were used to describe the observed behavior. The experimental and analytical results indicate crack healing occurs as the sample temperature is increased. Healing was not directly observed, however, due to the elevated temperatures and closed DMA instrument. Examining the samples after DMA characterization, the cracks that were observed before testing were still observed after testing. Since the sample was cooled back to room temperature, the residual thermal stresses returned and re-formed the cracks. The crack locations are controlled by the stress distribution and local defects, which would still be present after testing. Identical crack paths indicate incomplete

healing at the fiber-matrix interface. Previous studies that showed ideal healing were for the neat 2MEP4FS polymer (Plaisted and Nemat-Nasser 2007).

Since the cracks re-formed in the same locations, it is difficult to claim the samples were completely healed, even at elevated temperatures and despite the analytical results. Due to the essentially zero thickness of the cracks relative to the length of the sample, even poor crack healing that barely holds the crack faces together would have a dramatic impact on DMA bending measurements. Similar DMA experiments on composite samples with functionalized glass fibers have demonstrated that fiber surface treatments have a minimal impact on the measured properties despite large changes in the interfacial bonding strength (Jia et al. 2012). At the small strains used by the DMA, the quality of the interface isn't being evaluated. Beam bending measurements and analyses are also very sensitive to sample thickness. The ply thicknesses were estimated based on observations of the sample edges. Variations in these thicknesses through the unseen regions of the sample would strongly affect the measured results, as well as the estimated number of cracks needed to match the analytical and experimental results at room temperature. The number of cracks in the shear lag analysis is controlled by the shear moduli of the plies, which were estimated here by particularly crude methods. Given the good agreement between the number of estimated and observed cracks in the glass fiber composite sample, the ply thicknesses and shear moduli used in the analyses appear reasonable.

Each sample was only tested as a function of temperature once. Retesting the samples would give incomparable results as the gripped regions had permanently deformed during the high temperature portion of the tests. In order to observed crack

healing in the composite samples, additional thermal treatments could be used to increase the damage present in the samples before testing. By initially cooling the samples below room temperature, new cracks would be generated that should remain healed during microscopy observations after DMA characterization. Following this approach, Plaisted (2007) successfully observed composite crack healing.

The composite samples were only characterized at only one level of damage. Progressively imparting additional cracks would allow the shear lag model to be better compared with experimental measurements. A fracture criterion could be developed and an energy release rate estimated. More complex, variational methods for stress analysis in cracked cross-ply composites have been developed (Nairn 1989; Hashin 1996) and deemed more accurate for developing fracture criteria (Nairn et al. 1993). An energy release rate would be useful for evaluating the fiber-matrix interface and interfacial healing. The experimental methods given in the literature for developing a fracture criterion require relatively large samples, which would be difficult to produce with material quantities limited by current processing methods. Adaptation of the methods for use with the healable materials is left for future efforts.

Chapter 10

Areas for Future Research

The damaging and healing of polymers and fiber-reinforced composites have been investigated in this dissertation, with experiments and models developed to facilitate understanding of their behavior. This final chapter discusses areas where additional research and development offer possibilities for advancements in the field.

10.1   Modify Polymer and Composite Properties

Early in the research, collaborative efforts with Dr. Haim Weizman (UCSD Department of Chemistry & Biochemistry) focused on modifying the monomers to make them more manufacturable and improving the properties (e.g. increase T_g) of the final polymer. A new furan monomer, 3FT, was the result of this work. Although DSC measurements of 2MEP3FT indicate the cross-linking DA adducts cannot be separated and re-formed in this polymer (Chapter 3.2), modifications to the monomer(s) could address this problem. Other monomer versions can also be developed to address specific applications where damage healing would be beneficial.

Fiber-reinforced healable composites could also be modified to improve mechanical properties. Specifically, glass fibers could be functionalized to form thermally reversible cross-links with the re-mendable polymer matrix. This would enable interfacial healing, a valuable capability in a composite material as cracks in fiber-reinforced 2MEP4FS were observed to preferentially follow the fibers along the

interfaces (Figure 9.1). Peterson et al. (2011) functionalized glass fibers to create Diels-Alder (DA) adducts with a non-re-mendable polymer matrix, and interfacial healing was experimentally demonstrated with a single fiber microdroplet pull-out test.

Initial steps were taken to prepare a fiber-reinforced composite with both a healable matrix and healable fiber-matrix interfaces. Unidirectional glass fiber was functionalized with amine groups, NH_2, which will serve to anchor diene functional groups to the surface of the glass. Milled glass particles were functionalized concurrently with the unidirectional glass fiber. These particles have a larger surface area per effective unit volume and can represent the unidirectional fibers in surface characterization studies.

An 8 inch long by 2 inch wide piece of unidirectional S-2 glass fiber tape was cut out and the fill threads were removed. The milled glass particles were 15.3 g of Fibertec 3032 E-glass short fibers with an average diameter of 16 μm and average length of 200 μm (Fibertec 2011). The fibers and particles were washed separately in piranha solution and thoroughly rinsed with Milli-Q purified water. A 1 wt% solution of 3-aminopropyltrimethoxysilane (APS, Sigma-Aldrich) in 75:25 by weight mixture of purified water and ethanol (ETOH, Gold Shield) was prepared as the source of amine
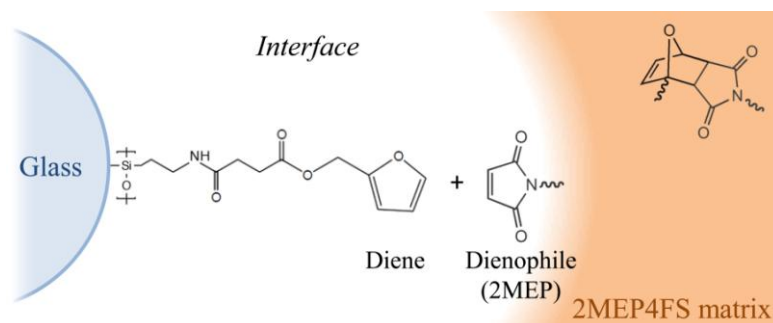

Figure 10.1 Scheme for creating a healable interface. Glass fiber is functionalized to form Diels-Alder thermally reversible cross-links with a 2MEP4FS matrix.

groups and divided between two 50 mL graduated cylinders. The unidirectional fibers were submerged in one cylinder and the milled glass particles were submerged in the other. The cylinders were placed upright in a 90 °C silicone oil bath and the fibers and particles were lightly agitated. After 1 hr, they were removed and rinsed twice with 50 mL of 75:25 wt% water and ETOH and a third time with 50 mL ETOH. The fibers and particles were placed in a 110 °C oven for 1 hr to dry and finalize the surface treatment. After cooling to room temperature, the glass was neutralized for 10 minutes in a mixture of 5 mL triethylamine (TEA, Fisher Scientific) and 95 mL dichloromethane (DCM, Fisher Scientific). The fibers and particles were washed three times with 60 mL purified water and dried for 1.5 hrs in a 110 °C oven.

The concentration of amine groups on the surface of the glass was determined using a picrate test (Gisin 1972; Lee and Loudon 1979), where the number of acid groups that the glass retains after an acid wash corresponds to the number of amines. The unidirectional glass fibers require a relatively large volume of liquid to cover their surfaces and this would dilute the final product below measurable levels. Since the milled glass particles have more surface area per volume of liquid required, they were characterized in place of the unidirectional fibers. Four determinations were sequentially prepared using 8.12 g of functionalized milled glass. In each determination, the particles were sonicated for four minutes in 0.02 M picric acid (Sigma Aldrich) in DCM. The picric acid attaches to amine groups in an acid-base interaction to form a picrate salt. The glass was rinsed five times with 40 mL DCM to wash away unreacted picric acid. The picric acid attached to the glass surface was removed with 0.5 mL n,n-diisopropylethylamine (DIEA, Sigma Aldrich) in 9.5 mL ETOH, followed by rinsing

with 30 mL ETOH. The collected DIEA-ETOH washings of each determination were analyzed using UV spectroscopy. Using Beer's law, the measured absorption of light corresponds to the molar concentration of the picrate salt where the extinction coefficient is known to be 14,500 at 358 nm (Gisin 1972). Using the cylindrical geometry and average dimensions to estimate the tested milled glass surface area, the four determinations give amine densities of 1612, 1372, 1319, and 1349 $nmol/m^2$. The high first result suggests the glass had not been sufficiently washed after functionalization and neutralization. The glass had only been lightly agitated during washing steps and not vigorously sonicated in order to maintain the unidirectional fiber orientation. The first determination suggests this washing method was insufficient, and the picrate test completed the necessary removal of excess amine groups. Excluding the first result, the average amine density is 1347 $nmol/m^2$.

A similar functionalization method was followed for milled glass particles using 3-aminopropyltriethoxysilane (APTES, Sigma-Aldrich) in place of APS. Picrate testing yielded an average surface functionalization of 644 $nmol/m^2$. Lee and Loudon (1979) used APTES to functionalize controlled pore glass. In their study, the average surface functionalization measured using the picrate test was 767 $nmol/m^2$ and shown to correspond well to other measurement methods. Comparing the present results with Lee and Loudon (1979) indicates the achieved amine densities are reasonable.

With amine-functionalized glass fiber prepared, the next step is attaching the functional groups to create DA adducts with a polymer matrix. Peterson et al. (2011) attach a bismaleimide to functionalize the surface with the dienophile in the DA reaction. Given the present synthesis routes, the furfuryl acid groups could be attached to the

amines instead of each other to create a diene-functionalized surface (Figure 10.1). The fibers could be embedded in a polymer matrix like 2MEP4FS to create a composite material for characterization.

10.2   Characterization and Analysis

The DMA bending experiments in Chapter 9 indicate the samples were healing, but the quality of the healing (healing efficiency) was not quantified. Specifically, the recovery of interfacial strength between the fibers and matrix could be characterized. Composite samples with functionalized glass fibers would benefit from such experiments to see if the modified surfaces improve interfacial strength and healing. The microbond test where a small bead of polymer is pulled along the fiber is one option. Peterson et al. (2011) had success with this method although it was noted that pieces of the polymer droplet would break off during testing. Plaisted (2007) found the method challenging to implement for 2MEP4FS and non-functionalized fibers. Another option is an ASTM standard test method for determining the interlaminar fracture toughness of unidirectional composites (ASTM D5528 2007), although it requires relatively large sample sizes. The double cleavage drilled compression (DCDC) fracture geometry has been shown to characterize interfaces (Turner et al. 1995) and might be adapted to study interfacial healing in a fiber-reinforced composite.

REFERENCES

AGY. High strength glass fibers: technical paper. Aiken, SC: AGY; 2006.

Amirkhizi AV. Fracture mechanics of elastic bodies with multiple independent load parameters. P Roy Soc A-Math Phy; Submitted 2012.

ASTM D1343-95. Standard test method for viscosity of cellulose derivatives by ball-drop method. West Conshohocken, PA: ASTM International; 2006.

ASTM D2983-09. Standard test method for low-temperature viscosity of lubricants measured by Brookfield viscometer. West Conshohocken, PA: ASTM International; 2009.

ASTM D5528-01. Standard test method for mode I interlaminar fracture toughness of unidirectional fiber-reinforced polymer matrix composites. West Conshohocken, PA: ASTM International; 2007.

Bleay SM, Loader CB, Hawyes VJ, Humberstone L, Curtis PT. A smart repair system for polymer matrix composites. Compos Part A-Appl S 2001;32:1767-76.

Brown EN, Sottos NR, White SR. Fracture testing of a self-healing polymer composite. Exp Mech 2002;42:372-9.

Brown EN, White SR, Sottos NR. Microcapsule induced toughening in a self-healing polymer composite. J Mater Sci 2004;39:1703-10.

Brown EN, White SR, Sottos NR. Fatigue crack propagation in microcapsule-toughened epoxy. J Mater Sci 2006;41:6266-73.

Carlson JA, English JM, Coe DJ. A flexible, self-healing sensor skin. Smart Mater Struct 2006;15:N129-35.

Chen X, Dam MA, Ono K, Mal A, Shen H, Nutt SR, Sheran K, Wudl F. A thermally re-mendable cross-linked polymeric material. Science 2002;295:1698-702.

Chen X. Novel polymers with thermally controlled covalent cross-linking [dissertation]. Los Angeles, CA: University of California at Los Angeles; 2003.

Chen X, Wudl F, Mal AK, Shen H, Nutt SR. New thermally remendable highly cross-linked polymeric materials. Macromolecules 2003;36:1802-7.

Chen Y, Kushner AM, Williams GA, Guan Z. Multiphase design of autonomic self-healing thermoplastic elastomers. Nat Chem 2012;4:467-72.

Cordier P, Tournilhac F, Soulié-Ziakovic C, Leibler L. Self-healing and thermoreversible rubber from supramolecular assembly. Nature 2008;451:977-80.

Davies P, Cantwell W, Kausch HH. Healing of cracks in carbon fibre-PEEK composites. J Mater Sci Lett 1989;8:1247-8.

Dowling NE. Mechanical behavior of materials: engineering methods for deformation, fracture, and fatigue. 2nd ed. New Jersey: Prentice-Hall; 1999.

Fernando PL, Williams JG. Plane stress and plane strain fractures in polypropylene. Polym Eng Sci 1980;20:215-20.

Fibertec. Microglass specifications. Bridgewater, MA: Fibertec Inc; 2008.

Fitch DA, Hoffmeister BK, de Ana J. Ultrasonic evaluation of polyether ether ketone and carbon fiber-reinforced PEEK. J Mater Sci 2010;45:3768-77.

Flory PJ. Principles of polymer chemistry. Ithaca, NY: Cornell University Press; 1953.

Ghezzo F, Smith DR, Starr TN, Perram T, Starr AF, Darlington TK, Baldwin RK, Oldenburg SJ. Development and characterization of healable carbon fiber composites with a reversibly cross linked polymer. J Compos Mater 2010;44:1587-603.

Gisin BF. The monitoring of reactions in solid-phase peptide synthesis with picric acid. Anal Chim Acta 1972;58:248-9.

Gotsmann B, Duerig U, Frommer J, Hawker CJ. Exploiting chemical switching in a Diels-Alder polymer for nanoscale probe lithography and data storage. Adv Funct Mater 2006;16:1499-505.

Hamilton AR, Sottos NR, White SR. Self-healing of internal damage in synthetic vascular materials. Adv Mater 2010;22:5159-63.

Hamilton AR. Sottos NR, White SR. Pressurized vascular systems for self-healing materials. J Roy Soc Interface 2012;9:1020-8.

Hansen CJ, Wu W, Toohey KS, Sottos NR, White SR, Lewis JA. Self-healing materials with interpenetrating microvascular networks. Adv Mater 2009;21:1-5.

Hashin Z. Analysis of stiffness reduction of cracked cross-ply laminates. Eng Fract Mech 1986;25:771-8.

Hashin Z. Finite thermoelastic fracture criterion with application to laminate cracking analysis. J Mech Phys Solids 1996;44:1129-45.

He MY, Turner MR, Evans AG. Analysis of the double cleavage drilled compression sample for interface fracture energy measurements over a range of mode mixities. Acta Metall Mater 1995;43:3453-8.

Highsmith AL, Reifsnider KL. Stiffness-reduction mechanisms in composite laminates. In: Reifsnider KL, editor. Damage in composite materials: basic mechanics, accumulation, tolerance, and characterization. ASTM STP 775. Philadelphia (PA): ASTM International; 1982. p. 103-17.

Holly EE, Venkataraman SK, Chambon F, Winter HH. Fourier transfom mechanical spectroscopy of viscoelastic materials with transient structure. J Non-Newton Fluid 1988;27:17-26.

Idonije K, Motuku M, Shehata I, Aglan H. Evaluation of the stress intensity factor of brittle polymers based on the crack arrest concept. J Reinf Plast & Compos 1993;12:778-86.

Janssen C. Sample for fracture mechanics studies on glass. 10th International Congress on Glass. Kyoto, Japan: Ceramic Society of Japan; 1974.

Jia Z, Holzworth K, Nemat-Nasser S. Milled glass reinforced polyurea composites: the effect of surface treatment. Proceedings of the Society for Experimental Mechanics Annual Conference. Costa Mesa, CA; 2012.

Jud K, Kausch HH, Williams JG. Fracture mechanics studies of crack healing and welding of polymers. J Mater Sci 1981;16:204-10.

Kaw AK. Mechanics of composite materials. 2nd ed. Boca Raton, FL: CRC Press; 2006.

Kessler MR, Sottos NR, White SR. Self-healing structural composite materials. Compos Part A-Appl S 2003;34:743-53.

Laws N, Dvorak GJ. Progressive transverse cracking in composite laminates. J Compos Mater 1988;22:900-16.

Lee CCY, Loudon GM. Quantitative determination of amino groups on derivatized controlled pore glass: a comparison of methods. Anal Biochem 1979;94:60-4.

Lee JW, Daniel IM. Progressive transverse cracking of crossply composite laminates. J Compos Mater 1990;24:1225-42.

Lin CB, Lee S, Liu KS. Methanol-induced crack healing in poly(methyl methacrylate). Polym Engr Sci 1990;30:1399-406.

Maccagno TM, Knott JF. The fracture behaviour of PMMA in mixed modes I and II. Eng Fract Mech 1989;34:65-86.

Marshall GP, Williams JG. The correlation of fracture data for PMMA. J Mater Sci 1973;8:138-40.

Michalske TA, Smith WL, Chen EP. Stress intensity calibration for the double cleavage drilled compression specimen. Eng Fract Mech 1993;45:637-42.

Murphy EB, Bolanos E, Schaffner-Hamann C, Wudl F, Nutt SR, Auad ML. Synthesis and characterization of a single-component thermally remendable polymer network: Staudinger and Stille revisited. Macromolecules 2008;41:5203-9.

Murphy EB, Wudl F. The world of smart healable materials. Prog Polym Sci 2010;35:223-51.

Nairn JA. The strain energy release rate of composite microcracking: a variational approach. J Compos Mater 1989;23:1106-29.

Nairn JA, S Hu. The formation and effect of outer-ply microcracks in cross-ply laminates: a variational approach. Eng Fract Mech 1992;41:203-21.

Nairn JA, Shoufeng H, Bark JS. A critical evaluation of theories for predicting microcracking in composite laminates. J Mater Sci 1993;28:5099-111.

Nemat-Nasser S, Chang S. Compression-induced high strain rate void collapse, tensile cracking, and recrystallization in ductile single and polycrystals. Mech Mater 1990;10:1-17.

Nemat-Nasser S, Muneo H. Micromechanics: overall properties of heterogeneous materials. 2nd ed. Amsterdam, Netherlands: Elsevier; 1999.

Nielsen LE. Cross-linking-effect on physical properties of polymers. J Macromol Sci-Rev M 1969;3:69-103.

Nielsen C, Amirkhizi AV, Nemat-Nasser S. The effect of geometry on fracture strength measurements using DCDC samples. Eng Fract Mech 2012;91:1-13.

Pallares, G, Ponson L, Grimaldi A, George M, Prevot G, Ciccotti M. Crack opening profile in DCDC sample. Int J Fract 2009;156:11-20.

Pang JWC, Bond IP. A hollow fibre reinforced polymer composite encompassing self-healing and enhanced damage visibility. Compos Sci Technol 2005;65:1791-9.

Park JS, Kim HS, Hahn HT. Healing behavior of a matrix crack on a carbon fiber/mendomer composite. Compos Sci Technol 2009;69:1082-7.

Pascault JP, Williams RJJ. Glass transition temperature versus conversion relationships for thermosetting polymers. J Polym Sci 1990;28:85-95.

Peterson AM, Jensen RE, Palmese GR. Thermoreversible and remendable glass–polymer interface for fiber-reinforced composites. Compos Sci Technol 2011;71:586-92.

Plaisted TA. UCLA meeting [lab book]. La Jolla, CA: University of California at San Diego; 2005.

Plaisted TA, Amirkhizi AV, Nemat-Nasser S. Compression-induced axial crack propagation in DCDC polymer samples: experiments and modeling. Int J Fract 2006;141:447-57.

Plaisted TA. Multifunctional composites: healing, heating and electromagnetic integration [dissertation]. La Jolla, CA: University of California at San Diego; 2007.

Plaisted TA, Nemat-Nasser S. Quantitative evaluation of fracture, healing and re-healing of a reversibly cross-linked polymer. Acta Mater 2007;55:5684-96.

Pulos GC, Knauss WG. Nonsteady crack and craze behavior in PMMA under cyclical loading: II. effect of load history on growth rate and fracture morphology. Int J Frac 1998;93:161-85.

Qiao J, Amirkhizi AV, Schaaf K, Nemat-Nasser S, Wu G. Dynamic mechanical and ultrasonic properties of polyurea. Mech Mater 2011:43:598-607.

Sakai K, Hirano T, Hosoda M. Electromagnetically spinning sphere viscometer. Appl Phys Express 2010;3:016602.

Sammis CG, Ashby MF. The failure of brittle porous solids under compressive stress states. Acta Metall 1986;34:511-26.

Sheng X, Akinc M, Kessler MR. Cure kinetics of thermosetting bisphenol e cyanate ester. J Therm Anal Calorim 2008;93:77-85.

Sjögren BA, Berglund LA. The effects of matrix and interface on damage in GRP cross-ply laminates. Compos Sci Technol 2000;60:9-21.

Smith PA. Ogin SL. On transverse matrix cracking in cross-ply laminates loaded in simple bending. Compos Part A-Appl S 1999;30:1003-8.

Smith PA. Ogin SL. Characterization and modelling of matrix cracking in a $(0/90)_{2s}$ GRFP laminate loaded in flexure. P Roy Soc A-Math Phy 2000;456:2755-70.

TA Instruments. DSC 2920: differential scanning calorimeter operator's manual. New Castle, DE: TA Instruments-Waters LLC; 1998.

TA Instruments. DMA 2980: dynamic mechanical analyzer operator's manual. New Castle, DE: TA Instruments-Waters LLC; 2002.

Tada H, Paris PC, Irwin GR. The stress analysis of cracks handbook. 3rd ed. New York: ASME Press; 2000.

Toohey KS, Sottos NR, Lewis JA, Moore JS, White SR. Self-healing materials with microvascular networks. Nat Mater 2007;6:581-5.

Toohey KS, Hansen CJ, Lewis JA, White SR, Sottos NR. Delivery of two-part self-healing chemistry via microvascular networks. Adv Funct Mater 2009;19:1399-405.

Toray Carbon Fibers America Inc. Torayca T300: technical data sheet CFA-001. Santa Ana, CA: Toray Carbon Fibers America Inc; 2012.

Trask RS, Bond IP. Biomimetic self-healing of advanced composite structures using hollow glass fibres. Smart Mater Struct 2006;15:704-10.

Turner MR, Dalgleish BJ, He MY, Evans AG. A fracture resistance measurement method for bimaterial interfaces having large debond energy. Acta Metall Mater 1995;43:3459-65.

Wade, LG Jr. Organic chemistry. 2nd ed. New Jersey: Prentice Hall; 1991.

Wang PP, Lee S, Harmon JP. Ethanol-induced crack healing in poly(methyl methacrylate). J Polym Sci Pol Phys 1994;32:1217-27.

Watanabe M, Yoshie N. Synthesis and properties of readily recyclable polymers from bisfuranic terminated poly(ethylene adipate) and multi-malimide linkers. Polymer 2006;47:4946-52.

Washburn EW. The dynamics of capillary flow. Phys Rev 1921;17:273-83.

Weizman H, Nielsen C, Weizman OS, Nemat-Nasser S. Synthesis of a self-healing polymer based on reversible Diels-Alder reaction: an advanced undergraduate laboratory at the interface of organic chemistry and materials science. J Chem Educ 2011;88:1137-40.

White SR, Sottos NR, Guebelle PH, Moore JS, Kessler MR, Sriram SR, Brown EN, Viswanathan S. Autonomic healing of polymer composites. Nature 2001;409:794-7.

Weiderhorn SM, Johnson H, Diness AM, Heuer AH. Fracture of glass in vacuum. J Am Ceram Soc 1974;57:336-41.

Williams HR, Trask RS, Bond IP. Self-healing sandwich panels: restoration of compressive strength after impact. Compos Sci Technol 2008;68:3171-7.

Wingard CD. Characterization of prepreg and cured epoxy/fiberglass composite material for use in advanced composite piping systems. Thermochim Acta 2000;357-358:293-301.

Wool RP, O'Conner KM. A theory of crack healing in polymers. J Appl Phys 1981;52:5953-63.

Wu DY, Meure S, Solomon D. Self-healing polymeric materials: a review of recent developments. Prog Polym Sci 2008;33:479-522.

Wudl F. Single component healable polymer [proposal]. Los Angeles, CA: University of California at Los Angeles; 2004.